

PUMP PROBE STUDIES OF SPIN DYNAMICS IN THE 2D
PEROVSKITE BUTYLAMMONIUM METHYLAMMONIUM LEAD
IODIDE

by

Seth Benjamin Todd

Submitted in partial fulfillment of the requirements
for the degree of Master of Science

at

Dalhousie University
Halifax, Nova Scotia
August 2017

© Copyright by Seth Benjamin Todd, 2017

For Uncle Doug

Table of Contents

List of Tables	vi
List of Figures	vii
Abstract	ix
List of Abbreviations and Symbols Used	x
Acknowledgements	xix
Chapter 1 Introduction	1
1.1 Motivation for Perovskite Materials	1
1.2 Fundamental Properties of Perovskite	4
1.2.1 Crystal Structure	4
1.2.2 Transport Properties	5
1.2.3 Optical Properties	8
1.3 Perovskite - A Potential Spintronic Material	10
1.4 Literature Review: Spin Dynamics in Perovskite	11
1.5 Outline of Thesis	13
Chapter 2 Background Information	14
2.1 Review of Bulk Semiconductor Physics	14
2.2 Effects of Confinement on Semiconductors	17
2.3 Optical Excitation in Semiconductors	18
2.4 Charge Carrier Relaxation	21
2.5 Spin Populations	22
2.6 Spin Relaxation	24
2.6.1 Bir-Aronov-Pikus	24
2.6.2 Elliott-Yafet	25
2.6.3 D'yakonov-Perel'	26
2.6.4 Expectations for the Strength of BAP, EY and DP for 2D Perovskites	28

2.7	Rashba/Dresselhaus Spin Splitting	31
Chapter 3	Sample Fabrication and Characterization	33
3.1	Materials Studied	33
3.1.1	Precursor Crystals	33
3.1.2	Thin Films	34
3.2	X-Ray Crystallography	36
3.3	Absorbance	39
3.3.1	Cary 60 UV-Vis	39
3.3.2	Tungsten Lamp Spectrometer	40
3.4	Optical Bandgap	41
3.5	Phase Transitions	41
Chapter 4	Overview of Experiments	43
4.1	Ultrafast Laser Source	43
4.1.1	Verdi V-18 Pump Laser	43
4.1.2	Mira-SEED Mode-Locking Laser	43
4.1.3	Mira Visible Optical Parametric Oscillator	44
4.1.4	Laser Spot Size	45
4.2	Ultrafast Pump-Probe Spectroscopy Techniques	45
4.2.1	Degenerate Time Resolved Differential Transmission	45
4.2.2	Circularly Polarized Pump-Probe	46
4.2.3	Calibration of Quarter Waveplates	48
Chapter 5	Results and Discussion	50
5.1	Sample Stability	50
5.1.1	Exposure to Humid Air	50
5.1.2	Radiatively Induced Degradation	52
5.2	Temperature Dependence of Absorption	53
5.3	Charge Carrier Dynamics in $\text{BA}_2\text{MAPb}_2\text{I}_7$	55
5.4	Spin Dynamics in $\text{BA}_2\text{MAPb}_2\text{I}_7$ at Room Temperature	58
5.4.1	Observed Trends in Spin Dynamics	58
5.4.2	Interpretation of the Measured Spin Dynamics	63
5.5	Spin Dynamics in $\text{BA}_2\text{MAPb}_2\text{I}_7$ at Low Temperature	64
5.5.1	Measured Temperature Dependence of Spin Dynamics	64

5.5.2	Discussion of the Temperature Dependence	67
Chapter 6	Conclusion	69
Bibliography	71
Appendix	Copyright Permissions	86

List of Tables

4.1	Degree of circular polarization of light produced by quarter wave-plates	49
-----	--	----

List of Figures

1.1	ABX ₃ crystal structure of lead-halide perovskite	4
1.2	Crystal structure of 2D BA ₂ MA _{n-1} Pb _n I _{3n+1} class of perovskites for n = 1, 2, 3, ∞	5
1.3	Time resolved differential transmission illustrating carrier lifetimes in 2D perovskite	7
1.4	Absorbance spectrum of MAPbI ₃	8
1.5	Optical Absorption of BA ₂ MA _{n-1} Pb _n I _{3n+1}	9
2.1	Simplified semiconductor band structure	16
2.2	Electronic band structure of 2D perovskite 4F-PEPI	17
2.3	Optical selection rules for perovskite semiconductors	20
2.4	Rasbha and Dresselhaus splitting in band structure	32
3.1	Image of BA ₂ MAPb ₂ I ₇ thin film	35
3.2	X-ray diffraction of crystal lattice	36
3.3	XRD of 2D and 3D lead-iodide perovskite	37
3.4	Parallel and perpendicular lattice planes in BA ₂ MAPb ₂ I ₇	38
3.5	XRD characterization of BA ₂ MAPb ₂ I ₇ film	38
3.6	Validation of tungsten halogen lamp for determination of absorbance spectrum	40
3.7	Tauc plot to determine bandgap energy of BA ₂ MAPb ₂ I ₇	42
4.1	Schematic of MIRA optical parametric oscillator	44
4.2	Basics of pump-probe spectroscopy	46
4.3	Experimental setup of linearly and circularly polarized pump-probe spectroscopy	47
4.4	Experimental setup for calibration of quarter waveplates	49

5.1	Change in absorbance due to humid air exposure	51
5.2	Increased transmission with laser power due to radiatively induced degradation	53
5.3	Absorbance as a function of temperature and wavelength . . .	54
5.4	Temperature dependence of exciton binding energy	55
5.5	Sample fit of spin-independent charge carrier dynamics	56
5.6	Results of linearly polarized pump-probe experiments	57
5.7	Sample raw data and exponential fit of spin relaxation in charge carriers at room temperature	59
5.8	Degree of circular polarization at room temperature as a function of laser detuning	60
5.9	Spin lifetime as a function of laser detuning	61
5.10	Spin lifetime as a function of laser pulse fluence	62
5.11	Sample raw data and exponential fit of spin relaxation in charge carriers at low temperature	65
5.12	Degree of circular polarization as a function of sample temperature	66
5.13	Spin lifetime as a function of temperature	67

Abstract

Halide perovskites have emerged as a promising class of materials for spintronic applications due to their large spin-orbit coupling and Rashba splitting. In this thesis, circularly polarized pump-probe spectroscopy was used to study the spin dynamics and relaxation mechanisms in the 2D perovskite butylammonium methylammonium lead iodide, $\text{BA}_2\text{MAPb}_2\text{I}_7$. The spin lifetime and initial degree of spin polarization was found to be 10 ps and 80% respectively for above bandgap laser excitation at room temperature. Spin lifetime and degree of spin polarization increased with laser fluence and decreased with excess energy above bandgap, indicating the dominant spin relaxation mechanism at room temperature is D'yakonov-Perel'. A strong reduction in the spin polarization was observed in the low-temperature phase, attributed to subpicosecond electron spin relaxation, with a residual spin lifetime of 100 ps at 10 K attributed to holes. These results will help assess the viability of 2D perovskites for applications in spintronics.

List of Abbreviations and Symbols Used

A	Absorbance
C	Coefficient Proportional to Exchange Integral Between Conduction and Valence Bands
C_e	Relative Fraction of Differential Transmission Due to Electrons
C_h	Relative Fraction of Differential Transmission Due to Holes
E_+	Upper Band of Rashba/Dresselhaus Splitting
E_-	Lower Band of Rashba/Dresselhaus Splitting
E_B	Exciton Binding Energy
E_g	Bandgap Energy
F	Numerical Factor Dependent on Scattering Mechanism
H_{SO}	Spin-Orbit Hamiltonian
L	Quantum Well Width
N	Excited Carrier Population
N^+	Population of Spin Up Carriers

N^-	Population of Spin Down Carriers
N_p	Free Hole Concentration
P	Spin Polarization
T	Ratio of Transmitted to Incident Power
U	Envelope Cell Function
V	Lattice Potential
ΔE	Rashba/Dresselhaus Energy Splitting
$\Delta T/T_0$	Differential Transmission
Δ_{SO}	Split-Off Energy
Δ_{ex}	Exchange Splitting of Excitonic Ground State
Δt	Time Delay
Ω	Effective Magnetic Field
Φ_i	Incident Radiant Flux
Φ_t	Transmitted Radiant Flux
α	Absorption Coefficient

δ	Dirac-Delta Function
ϵ	Energy Eigenvalue
η	An Integer
\hbar	Reduced Plank's Constant
λ	Wavelength
λ_D	Dresselhaus Coefficient
λ_R	Rashba Coefficient
μ_s	Spin Magnetic Moment
∇	Gradient Operator
∇^2	Laplace Operator
ν	Photon Frequency
ψ	Electron Wavefunction
σ	Pauli Spin Matrices
σ^+	Left Circularly Polarized Light
σ^-	Right Circularly Polarized Light

τ	Carrier Lifetime
τ_p	Momentum Scattering Time
τ_s	Spin Lifetime
τ_{th}	Thermalization Time
J	Total Angular Momentum Operator
L	Orbital Angular Momentum Operator
S	Spin Angular Momentum Operator
k	Wavevector
p	Momentum Operator
r	Relative Electron Position
T	Sample Temperature
a	Pinhole Radius
n	Perovskite Layer Number
w	Laser Spot Size
θ	X-ray Incident Angle

a_B	Exciton Bohr Radius
c	Speed of Light
d	Lattice Plane Spacing
e	Elementary Charge
e^-	Electron
h	Plank's Constant
h^+	Hole
j	Total Angular Momentum Quantum Number
l	Orbital Angular Momentum Quantum Number
m	Rest Mass of Electron in Vacuum
m^*	Effective Mass
m_j	Secondary Total Angular Momentum Quantum Number
m_s	Secondary Spin Angular Momentum Quantum Number
n	Energy Band Label

n_z	Quantum Well Principal Quantum Number
r	Numerical Tauc Factor Based on Nature of Transition
s	Spin Angular Momentum Quantum Number
t	Time
2D	Two Dimensional
3D	Three Dimensional
4F-PEPI	Fluorinated phenylethylammonium lead iodide ($[\text{pFC}_6\text{H}_5\text{C}_2\text{H}_4\text{NH}_3]_2\text{PbI}_4$)
BA	Butylammonium ($\text{CH}_3(\text{CH}_2)_3\text{NH}_3$)
BAP	Bir-Aronov-Pikus
c-Si	crystalline Silicon
CB	Conduction Band
CBM	Conduction Band Minimum
CW	Continuous Wave

DCP	Degree of Circular Polarization
DFT	Density Functional Theory
DMF	Dimethylformamide
DP	D'yakonov-Perel'
DSSC	Dye-Sensitized Solar Cell
EY	Elliott-Yafet
GVD	Group Velocity Dispersion
IR	Infrared
LBO	Lithium Triborate
LCP	Left Circularly Polarized
MA	Methylammonium (CH_3NH_3)
ML	Mode-Locked

ND:YVO4	Neodymium-doped Yttrium Orthovanadate
OPO	Optical Parametric Oscillator
PCE	Power Conversion Efficiency
PEA	Phenylethylammonium ($[\text{C}_6\text{H}_5\text{C}_2\text{H}_5\text{NH}_3]^+$)
PEPI	Phenylethylammonium lead iodide ($\text{C}_6\text{H}_5\text{C}_2\text{H}_5\text{NH}_3)_2(\text{CH}_3\text{NH}_3)_{n-1}\text{Pb}_n\text{I}_{3n+1}$)
PL	Photoluminescence
PV	Photovoltaic
QWP	Quarter Waveplate
RCP	Right Circularly Polarized
SFET	Spin Field Effect Transistor
SHG	Second Harmonic Generation
SOC	Spin-Orbit Coupling

TA	Transient Absorption
TAM	Transient Absorption Microscopy
Ti:Sapphire	Titanium-doped Sapphire
TRDT	Time Resolved Differential Transmission
VB	Valence Band
VBM	Valence Band Maximum
Vis	Visible
XRD	X-ray Diffraction

Acknowledgements

This project was truly a team effort and without the help of so many brilliant and selfless people this thesis could not have been completed. To everyone with whom I've interacted over my two years in Halifax and at Dalhousie, I am truly grateful for our time together. I would like to give special recognition to a number of people who had an especially significant role in helping me make it through this Masters.

First and foremost, I would like to acknowledge my supervisor Kimberley Hall. Kimberley has been a mentor to me in more than just physics and has gone above and beyond her duties as a supervisor to get me to this point in my degree and life. No matter how dire our timeline might have seemed or how stressed Kimberley felt, she was always a calming influence on me, assuring me that the project could and would get done. Thank you Kimberley!

To my committee members, Professor Jesse Maassen and Professor Laurent Kreplak, thank you so much for taking time out of your busy schedules to aid me during the culminating stage of this journey. You have both willingly accepted duties beyond that of a normal committee member and for that I thank you.

To Professor Ian Hill and Charlotte Clegg, thank you so much for lending me your laboratory and perovskite expertise. Without you I would have no samples to study and what a poor thesis that would be.

I have had the most amazing research group a physicist could ask for. To Ajan, I cannot thank you enough for all your help, chief among it the times you joined me in the lab until 2am collecting data. Let's grab a pint at the Club soon! To Drew, whether it be edits on my thesis or words of wisdom over scotch, I will always appreciate your advice and friendship. Dan, my go-to-guy for any question, be it physics or life related, thanks for showing me the ropes from my day one in Halifax. Special shout-out for your Labview prowess and the tube of science. Sam, your inability to ever stop having fun made the tough parts of this Masters so much easier. Thank you and Gametime bud! Thank you Douwe for forcing me to get out and explore Nova Scotia. And finally Ali, thanks for all your help this summer and for

putting up with my raw managerial skills.

I'd like to express my gratitude to my family for all their support these past two years. Mom, whether it be a quick message or a fancy dinner, your love was always felt and appreciated. I'm so glad I had this time in Nova Scotia with you. Dad, your sage advice on anything from finances to fantasy baseball and your amusing attempts to explain my research have been almost as memorable as the meals you and Kathy make when I come home. Thank you! Isaac and Sophie, thank you so much for making my transition from physics to law and from Halifax to Chicago as easy as it's been. I could never have done it without you and I am so excited about living so close to you. To Aunt Julie, thank you for your interest in my work and in the physics of all things. And lastly to Katie, thank you for your unwavering support, both before and after.

Chapter 1

Introduction

1.1 Motivation for Perovskite Materials

The growing awareness and concern for the adverse environmental effects of increasing global energy consumption has led to the research and development of new clean and sustainable energy technologies. Solar technology is particularly appealing due to the Sun's near limitless supply of energy, potential for economic growth and minimal burden on the environment. For the past 40 years, crystalline silicon (c-Si) solar cells have been at the forefront of this energy shift and have experienced significant advancement in photoelectric power conversion efficiency (PCE) as well as reduction in fabrication cost [1, 2]. In some economies around the world, the cost to produce electricity from solar technologies is comparable to that from fossil fuels [3]. Nonetheless, further increase in PCE and/or reduction in cost is necessary for global energy markets to experience a large-scale adoption of solar technology. With that goal in mind, many other newer solar cell technologies with potential for even lower solar energy cost have emerged and begun to be studied. In contrast to c-Si solar cells, which require the use of expensive high-temperature dry laboratories for fabrication, so-called "next generation" photovoltaics (PV), which include thin-film vapor-deposited semiconductors, such as CdS/CdTe [4, 5], and solution-processed organic, inorganic or hybrid semiconductor-based solar cells [6–10], can be produced at near room temperature in standard university wet laboratories, drastically reducing costs. A recent surge in the interest and study of these next generation PVs has resulted in great leaps in efficiency and stability of these technologies over the past 15 years [1] and commercial products based on these technologies are already being sold for low-power consumption applications. Yet, for next generation PVs to break into utility-scale power markets, significant advancements in efficiency, scalability, stability and cost are required.

One family of materials which shows particular promise for PV applications is

halide perovskites [11–13]. Solar cells based on halide perovskite photon absorbers have shown remarkable potential to combine low-cost fabrication with high, and rapidly increasing, efficiency [1]. Halide-perovskites, specifically methylammonium lead iodide (MAPbI₃; MA = CH₃NH₃), originally fabricated by Weber in 1978 [14], were first used as the absorbing layer of dye-sensitized solar cells (DSSC) by Kojima *et.al.* in 2009, achieving a device efficiency of 3.8% [15]. In subsequent years, efficiencies have vastly progressed thanks to improved experimental techniques and device architecture. In 2011, Im *et.al.* reached a device efficiency of 6.5% utilizing MAPbI₃ nanoparticles as DSSC absorbers and liquid electrolyte hole acceptor [16]. Replacing the liquid electrolyte with a *spiro*-MeOTAD hole transport layer and encasing the MAPbI₃ film in a mesoscopic TiO₂ film or scaffold, enabled Kim *et.al.* to achieve 9.7% efficiency in 2012 [12]. Later that year, building upon Kim’s design, Lee *et.al.* raised the efficiency to 10.9% by replacing the electrically conductive TiO₂ film casing with electrically insulating Al₂O₃ [13]. By further exploring the chemical composition and/or thicknesses of perovskite, scaffold and hole-transporting layers, Jeon *et.al.* managed a certified PCE of 16.2% in 2014 [17]. By 2015, the efficiency of halide perovskite-based solar cell devices had climbed to 20.1% [18] thanks to optimization of perovskite growth techniques resulting in increased control of morphology [19,20] as well as better engineering of electron and hole transport layers [21–23]. Finally, the current PCE record for thin-film perovskite devices as of this writing is 22.1% [1]. The gains in PCE of halide perovskite-based solar cells in the past eight years have been fast and frequent but even more extraordinarily, much of the gains in efficiency have been made with empirical exploration and optimization alone, with many of halide perovskites’ fundamental properties remaining unknown [24]. Only recently has substantial effort been put into characterizing the fundamental processes occurring in, and optoelectronic properties of, perovskites [25–29]. A review of perovskite properties and techniques used will be provided in Sec. 1.2.

In addition to the challenges halide perovskite-based PVs face due to the demand for high efficiency, there are two major obstacles to overcome before widespread implementation of perovskite PVs in energy markets can occur, namely, toxicity and stability. The former issue is due to the presence of toxic lead in the most efficient halide perovskite materials to date [30]. In light of this, an undertaking to replace lead

perovskites with more environmentally friendly options is underway by substituting lead with other group IV elements tin and germanium [31–34] or trivalent antimony or bismuth [35,36]. Of the aforementioned substitutes, tin perovskite materials have the highest PCE [37], yet these materials suffer even more heavily than their lead cousin from perovskite’s second obstacle, that of stability. The temporal stability of halide perovskites has been shown to be reduced by moisture, heat, light and detrimental reaction to neighbouring device layers [38,39]. In order for these materials to be practically viable for use in PV devices, especially in warm, humid climates, resistance to the detrimental effects of moisture, heat and light is crucial. In 2014, Smith *et.al.* had success with enhanced moisture stability in a solar cell with a layered perovskite photon absorber dubbed PEPI $((C_6H_5C_2H_5NH_3)_2(CH_3NH_3)_2Pb_3I_{10})$ [40]. This success with layered perovskite has led to the development of a class of two dimensional (2D) perovskites which have been shown to be more moisture resistant than their three dimensional (3D) counterpart [41]. Indeed, solar cell devices produced with the 2D series of lead-halide perovskite light absorbing layer have survived several months in a humid atmosphere, with little PCE loss [40,41]. Contrast that with the mere hours it may take for the 3D lead-halide perovskite devices to decay, and one easily sees the appeal of the 2D class of materials. However, the efficiency of 2D lead-halide perovskites has only just reached the halfway point of its 3D analogue [42]. Thus, considerable work is needed to understand the fundamental properties of 2D perovskites to better engineer and optimize device architectures for solar cell applications. This thesis will focus on one particular 2D perovskite, butylammonium methylammonium lead iodide ($BA_2MAPb_2I_7$; $BA = CH_3(CH_2)_3NH_3$), with the aim of furthering the understanding of the fundamental properties of this class of 2D perovskite materials.

Perovskite materials’ applications are not limited to photovoltaics. For decades, scientists have been allured to perovskites for their many interesting electromagnetic and physical properties including superconductivity [43–46], magnetoresistance [47], ferroelectricity [48], and spin dependent transport [49]. These properties make these materials excellent candidates in applications such as light emitting diodes [50–52], lasers [53,54], telecommunications [55], and spintronics [56,57], the last of which is of particular interest in this study and will be introduced in detail in Sec. 1.3.

1.2 Fundamental Properties of Perovskite

1.2.1 Crystal Structure

Perovskites are a class of materials with the same crystal structure as calcium titanate, CaTiO_3 , originally found in the Ural Mountains and first characterized by Lev A. Perovski [58]. This structure is labeled ABX_3 and encompasses hundreds of different materials with a multitude of properties as briefly described in Sec. 1.1. In this description, A and B are distinct cations and X is an anion which is typically oxygen, an alkali metal, or a halogen. In the case of MAPbI_3 , A is methylammonium, B is lead and X is iodine. In 1958, by synthesizing and characterizing the structure of CsPbCl_3 and CsPbBr_3 , C.K. Moller first determined the cubic lattice phase of halide-perovskites shown in Figure 1.1.

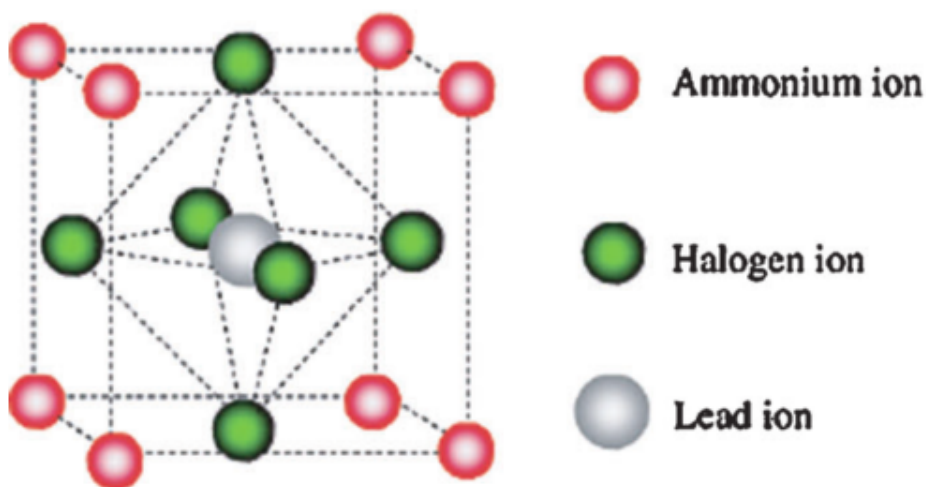


Figure 1.1: ABX_3 crystal structure of a lead-halide perovskite in the cubic lattice phase, adapted from Ref. [59]. In this case, A is an organic ammonium ion, B is lead and X is a halogen.

The class of 2D butylammonium methylammonium lead iodide materials have the general formula $\text{BA}_2\text{MA}_{n-1}\text{Pb}_n\text{I}_{3n+1}$ for $n \in \mathbb{N}$ where ($n = 1$) is the simple one layer true 2D case and ($n = \infty$) is the 3D MAPbI_3 perovskite. Perovskites with finite $n > 1$ thicknesses are regarded as multiple layer 2D materials. The butylammonium cation

spacers act to separate the methylammonium lead iodide layers creating what can be thought of as a natural multiple quantum well structure where the semiconducting inorganic lead iodide layers are the wells and the insulating organic butylammonium layers are the barriers [60–62]. The crystal structure for the 2D class of materials is shown in Figure 1.2 for $n = 1, 2, 3, \infty$.

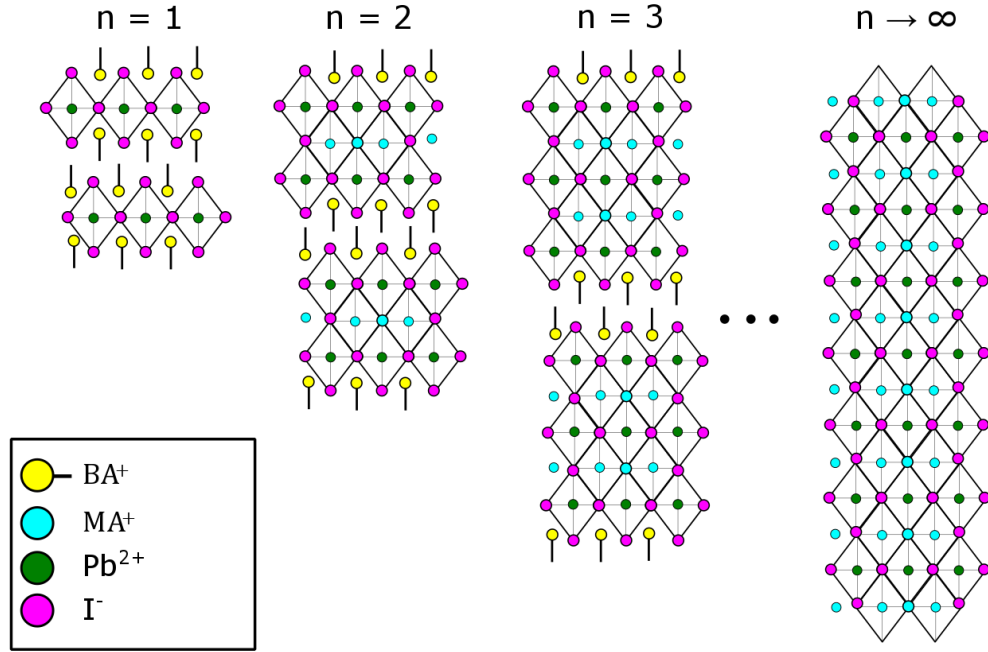


Figure 1.2: Crystal structure of $\text{BA}_2\text{MA}_{n-1}\text{Pb}_n\text{I}_{3n+1}$ ($\text{BA} = \text{C}_4\text{H}_9\text{NH}_3$; $\text{MA} = \text{CH}_3\text{NH}_3$) for $n = 1, 2, 3, \infty$. The BA ions (yellow) separate the inorganic lead (green) iodide (pink) layers creating a multiple quantum well structure. MA ions (blue) bind the lead iodide layers together for case of multiple layer wells ($n > 1$).

1.2.2 Transport Properties

The power conversion efficiency is the fraction of power from light generated electric current over the incident power from photons. The collection probability in a solar cell is the probability that a photoexcited charge carrier will be collected by the electron or hole acceptor material in order to contribute to usable current. Thus, increasing collection probability directly corresponds to an increase in the PCE of a cell. The collection probability of a cell is dictated by the relationship between the absorption depth and the diffusion length of photoexcited charge carriers in the photon absorbing

layer of the solar cell. The absorption, or penetration, depth is a measure of how far photons travel into a material before being absorbed and creating an electron-hole pair. The diffusion length dictates how far those photoexcited electrons and holes can travel through the material before recombining or undergoing some other form of relaxation. If the light absorbing material's penetration depth is large in comparison with the charge carrier diffusion lengths, the charge carriers will recombine before reaching the acceptor layer, and thus collection probability will be low. Lead-halide perovskites have been shown to combine large absorption coefficients (short penetration depths) in the visible spectrum with long carrier diffusion lengths, shedding insight as to why such rapid gains in PCE have occurred in these materials [63–65]. Xing *et.al.* and Stranks *et.al.* separately used techniques called time-resolved photoluminescence (PL) and transient absorption (TA) spectroscopy to obtain diffusion lengths for electrons and holes in MAPbI₃ of greater than 100 nm [25,26] by fitting PL and TA decay to the diffusion equation [66]. The diffusion lengths obtained are on the order of the absorption depth for MAPbI₃ [25]. Furthermore, Guo *et.al.* were able to directly observe long-range carrier transport of ~ 220 nm in 2 ns via two-dimensional transient absorption microscopy (TAM) imaging, estimating carriers diffusion lengths to be on the order of 1 μm in polycrystalline MAPbI₃, far exceeding the absorption depth in these materials [67]. These diffusion lengths compare favourably with those of other next generation PV materials such as solution processed conjugated materials (~ 10 nm) [66, 68, 69], thermally deposited organic molecules (10-50 nm) [70, 71], and colloidal quantum dot films (30-80 nm) [72]. By decreasing the density of trap states, a method for carrier recombination, Shi *et.al.* were able to measure diffusion lengths estimated to be as long as 8 μm in MAPbI₃ and even longer (~ 12 μm) in its lead bromide (MAPbBr₃) counterpart [73].

As mentioned in Sec. 1.1, although 2D perovskite materials have shown increased moisture resistance, they have not yet reached power conversion efficiency levels of 3D perovskites. It is not yet fully understood if these low efficiencies are due to a lack of optimization in 2D perovskite solar cell fabrication, or fundamental issues with charge carrier transport in 2D perovskite light absorbing materials. Milot *et.al.* used time resolved differential transmission (TRDT) to study the charge-carrier dynamics of a 2D lead iodide perovskite with phenylethylammonium (PEA) organic spacers

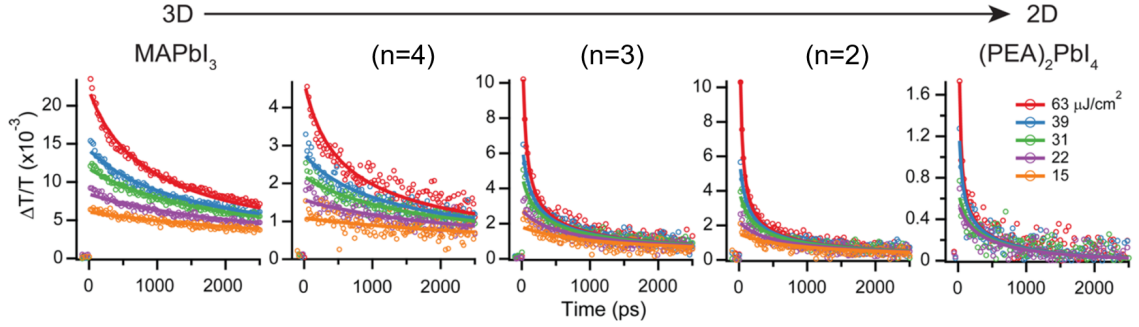


Figure 1.3: Time resolved differential transmission (TRDT) in 3D and 2D phenylethy-lammonium (PEA) lead iodide $((\text{PEA})_2\text{MA}_{n-1}\text{Pb}_n\text{I}_{3n+1})$ perovskite, adapted from Ref. [74]. The TRDT illustrates the decreased excited carrier lifetimes as the well thickness (n) decreases and moves from 3D MAPbI_3 towards 2D $(\text{PEA})_2\text{PbI}_4$.

and found the diffusion lengths of the true single layer 2D material ($n = 1$) to be ~ 60 nm in comparison to $\sim 2.2 \mu\text{m}$ for that of 3D MAPbI_3 . This drastic decrease in diffusion length could be due to the confining effect of the quantum wells in the 2D material [61]. However, Milot *et.al.* found that the diffusion lengths in layered perovskite with larger well thicknesses ($n > 1$) rebounded and in one case ($n = 3$) even exceeded ($\sim 2.5 \mu\text{m}$) the diffusion length of the 3D material. This occurred despite the carrier lifetimes continually decreasing with decreasing layer number, as seen in Figure 1.3 [74]. A suggested explanation for this discovery is the relationship between the chemical and physical properties of the perovskite film, most notably the orientation of the 2D layers with respect to the substrate, and its device efficiency [41]. The conductivity is higher in the inorganic lead iodide layers than the organic spacer layers [75, 76] and therefore in current solar cell architecture, unless lead iodide layers are oriented perpendicularly to the substrate, charge transport will be significantly hindered. Indeed, an X-ray diffraction (XRD) analysis on a similar 2D perovskite material by Cao *et.al.* found that the ($n = 1$) material preferentially oriented parallel to the substrate and the ($n = 3$) preferentially oriented perpendicularly, resulting in device efficiencies of 0.01% and 4.02% for ($n = 1$) and ($n = 3$) respectively [41]. Multiple layer ($n > 1$) 2D perovskite have been studied far less extensively than the ($n = 1$) material, with studies only beginning in the past two to three years. Their increased device efficiency over ($n = 1$) 2D perovskite and increased moisture resistance over 3D materials, make multiple layer 2D perovskite materials of great

interest in the PV community.

1.2.3 Optical Properties

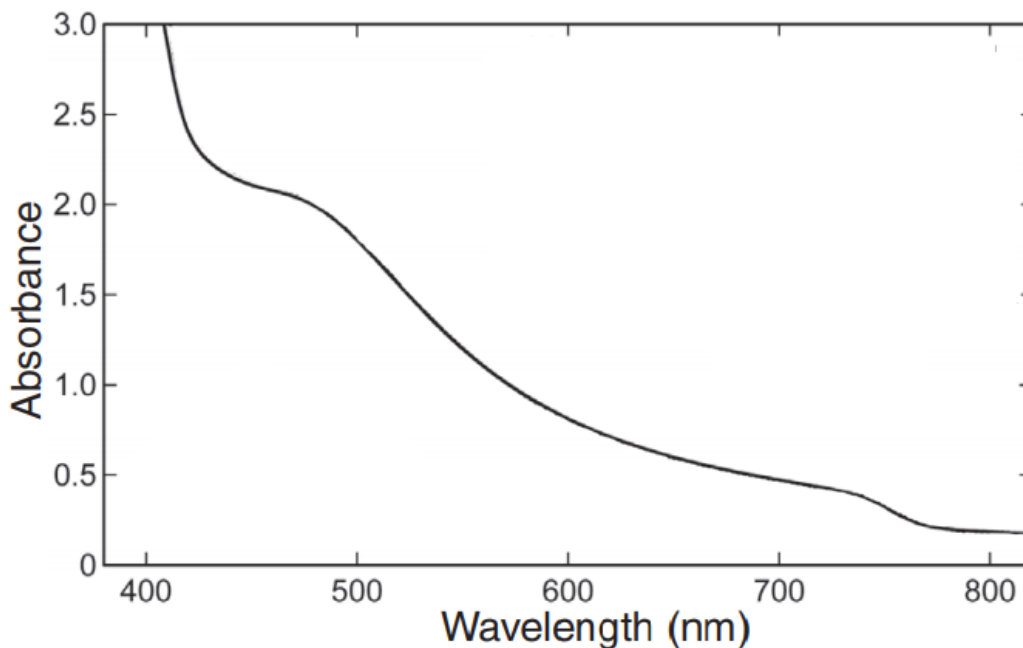


Figure 1.4: Absorbance spectrum of MAPbI₃, adapted from Ref. [13]. Two absorbance peaks are visible, one at 480 nm and the other at 760 nm. The latter is attributed to the direct bandgap transition however the origin of the former is still in dispute.

Beyond their attractive charge transport properties, lead-halide perovskites are appealing for their strong, broad absorption across the solar spectrum. At room temperature, the linear absorption spectrum of MAPbI₃ exhibits two peaks located at 480 nm and 760 nm [12,13,16,77–79]. The low energy absorption peak is attributed to the direct transition from the valence band maximum (VBM) to conduction band minimum (CBM), however the origin of the second absorption peak is still disputed [26]. These peaks can be seen in the linear absorption spectrum from Lee *et.al.* in Figure 1.4 [13]. Using density functional theory (DFT), Even *et.al.* determined the bandgap of MAPbI₃ to be direct [80] helping explain the large absorption coefficient in the solar spectrum ($5.7 \times 10^4 \text{ cm}^{-1}$ at 600 nm) [26], far greater than that of indirect bandgap photovoltaic materials such as c-Si ($\sim 3 \times 10^3 \text{ cm}^{-1}$ at 600 nm) [81].

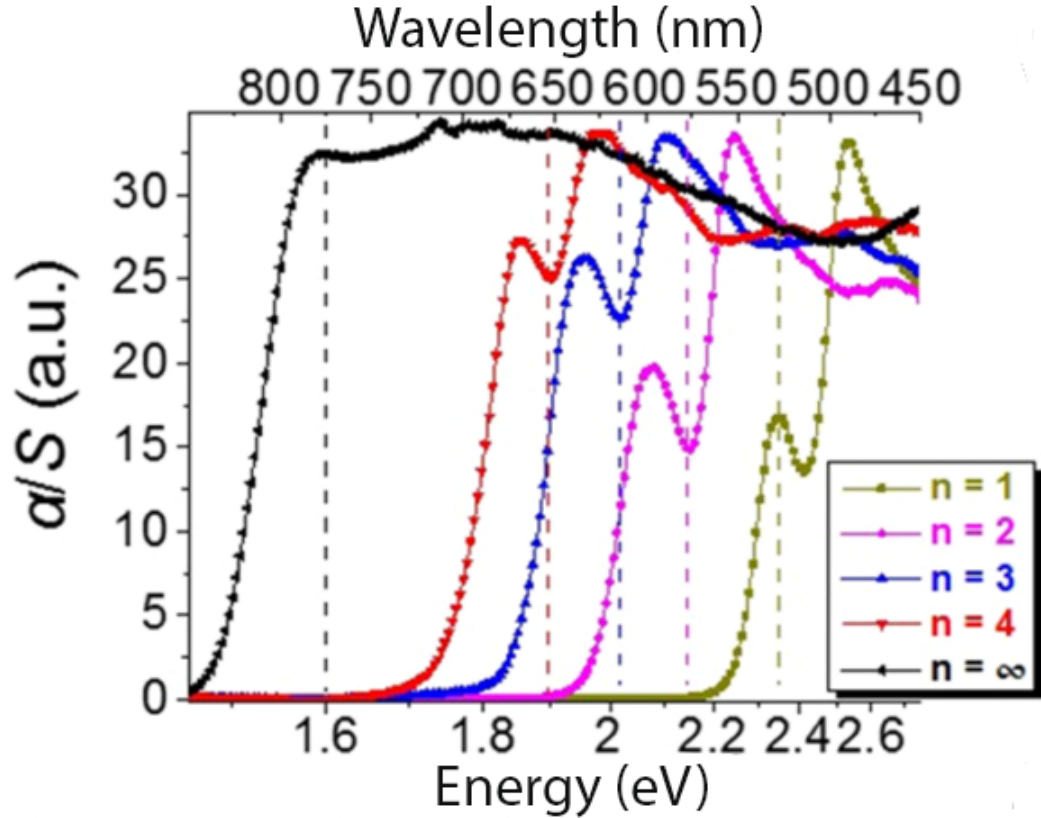


Figure 1.5: Optical absorption of $\text{BA}_2\text{MA}_{n-1}\text{Pb}_n\text{I}_{3n+1}$ obtained by Stoumpos *et.al.* using diffuse reflectance measurements and converted using the Kubelka-Munk function ($\alpha/S = (1 - R)^2/2R$). Adapted from Ref. [76].

The confining nature of the quantum wells in the 2D class of lead iodide perovskites, ($\text{BA}_2\text{MA}_{n-1}\text{Pb}_n\text{I}_{3n+1}$), increases the energy of photon absorption. As seen in Figure 1.5 from Stoumpos *et.al.*, there is increasing energy of peak absorption with decreasing well thickness, n [76]. For each 2D material, the larger, higher energy absorption peak is attributed to the bandgap transition while the smaller, lower energy peak is attributed to excitonic (bound electron-hole pair states) absorption [76]. Again using DFT, Stoumpos *et.al.* found the bandgap of these 2D materials to be direct with the same trend of increasing bandgap energy with decreasing well thickness as was found experimentally [76]. The strong bandgap and excitonic absorption in the visible range in 2D lead-halide perovskite are ideal optical properties for PV materials.

1.3 Perovskite - A Potential Spintronic Material

In addition to their strong potential for photovoltaic applications, halide perovskites are a promising material for use in spintronics. Semiconductor spintronics seeks to create optoelectronic and electronic devices which exploit the intrinsic angular momentum, or spin, of charge carriers in semiconductors in addition to their electric charge [82–85]. The incorporation of this spin degree of freedom of the charge carriers provides the potential for added functionality in terms of the data processing and transfer speed, decreased power consumption, increased integration densities and non-volatile memory in comparison to conventional semiconducting devices [83].

Inorganic semiconducting materials have been intensively investigated over the past two decades for their potential use in a variety of spintronic devices including optical switches and isolators, spin lasers and light emitting diodes, and spin transistors [86–88]. All-optical switches and isolators allow for telecommunication signals to be selectively switched between circuits and have been realized in a variety of inorganic semiconductors [86, 89–91]. Materials which exhibit a strong Faraday effect, a light-matter interaction which causes a rotation in the plane of light polarization, combined with short spin lifetimes, would allow for much more rapid switching and faster telecommunication [92]. Spin-based lasers could allow for a reduction in the lasing threshold required for stimulated emission. Spin polarized electrons with long lifetimes selectively couple to one of two photon modes which may enable the threshold to be reduced by nearly 50% [87]. Since Datta and Das first theorized the spin-based transistor in 1990 [82] the realization of a scalable spin field effect transistor (SFET) has been the holy grail of spintronics. A large, switchable Rashba splitting with long spin lifetimes would help enable the strong spin injection, manipulation and detection required in a SFET and significant progress has been made in this area [93–97]. However, the creation of a spin transistor remains a daunting task in part because materials with large spin-orbit coupling (SOC), helpful for spin manipulation, have short spin lifetimes, which makes the transportation of information more difficult [88, 98–100]. A multitude of materials have been explored for potential use in a SFET such as those with strong SOC including GaAs, InSb and Pt for effective spin injection and manipulation [101–103] as well as those with weak SOC, such as silicon, graphene and diamond, for long spin lifetimes [104–106].

Halide-perovskites have only recently begun to be studied for spintronic applications but have been shown to offer unique properties such as large, switchable SOC and spin dependent optical selection rules for spin manipulation [80, 107–112] and unexpectedly long spin lifetimes [57] and can be solution processed making them inexpensive to fabricate. Additionally, halide-perovskites have been theorized [107, 112] and experimentally observed [110] to have a large Rashba splitting effect, further enabling spin manipulation. These properties have made researchers optimistic about the potential for scalable perovskite spintronic devices, however a more comprehensive understanding of the spin-dependent properties and processes in perovskite is needed for this to occur.

1.4 Literature Review: Spin Dynamics in Perovskite

The large SOC and Rashba splitting in lead-halide perovskites allow for efficient spin injection, however a large SOC can also drastically reduce spin lifetimes [84]. Since different spin devices require different spin lifetimes for proper application, a detailed understanding of the spin dynamics and relaxation mechanisms is needed to evaluate perovskite’s suitability as a spintronic material. The spin relaxation lifetime dictates how quickly an initial net polarization or imbalance in spins relaxes to an equilibrium state of an equal number spin up and spin down charge carriers. More details regarding spin populations and relaxation will be provided in Chapter 2. The first measurement of a spin lifetime in lead-halide perovskite was done by Giovanni *et.al.* in 2015 on MAPbI₃ [108]. Using circularly polarized TRDT spectroscopy, Giovanni *et.al.* determined the initial degree of spin or circular polarization (DCP) was $\sim 90\%$, where 100% DCP is defined as all of the excited electrons for the relevant transition carrying the desired spin polarization, dictated by the polarization of the incident laser light. Their circular TRDT measurements yielded spin lifetimes of (7 ± 1) ps and (1.1 ± 0.1) ps for electrons and holes respectively at a sample temperature of 77 K. They found that spin lifetime decreased both with increased sample temperature and with increased laser fluence. Based on these trends, Giovanni *et.al.* argued that the Elliott-Yafet (EY) spin relaxation mechanism, in which momentum scattering of conduction band electrons randomizes their spin, is the dominant spin relaxation

mechanism in MAPbI₃. A detailed analysis of EY and other spin relaxation mechanisms is presented in Chapter 2.

In 2015, Zhang *et.al.* used magnetic field-induced circularly polarized photoluminescence to study spin dynamics in hybrid lead-halide perovskite MAPbI_{3-x}Cl_x films [109]. They found that the DCP increased linearly with the applied magnetic field for fields up to B = 5 T. They also found an inverse relationship between DCP and sample temperature for temperatures in the range $T = 18$ to 100 K. Using these relationships Zhang *et.al.* calculated the change in g-factor (a property which relates a particle's magnetic moment to its spin angular momentum) of the photogenerated electron-hole pair and Zeeman shift in the electron and hole energy levels. This allowed them to calculate a spin relaxation time of 80 ps at 18 K in the presence of a 100 mT magnetic field. In 2016, Giovanni *et.al.* showed that excitonic spin state energies could instead be selectively tuned in the 2D perovskite material 4F-PEPI ((C₆H₄FC₂H₄NH₃)₂PbI₄) with circularly polarized light via the optical Stark effect. They achieve a Stark effect energy splitting equivalent to a Zeeman effect with a 70 T applied magnetic field, much larger than what can be attained using conventional systems [113]. This demonstrated that spin state manipulation in perovskite materials with light may be a much more practical approach than manipulation via magnetic fields.

Recently in 2017, Odenthal *et.al.* used time resolved Faraday rotation, a technique to measure photoinduced magnetization, to observe spin relaxation lifetimes exceeding 1ns in MAPbI_{3-x}Cl_x at 4 K in the absence of a magnetic field [57]. At higher temperatures, they found the spin lifetimes to decrease with increasing sample temperatures, obeying the power law $\tau_s \propto T^{-1.51}$ where τ_s is the spin lifetime. This spin lifetime and temperature dependence vary drastically from the observations of Giovanni in 2015 [108] which may be due to the different film fabrication process and resulting film morphology. The temperature dependence found by Odenthal *et.al.* is not readily explained by any of the known spin relaxation mechanism and thus they suggest two or more of the existing mechanisms may be present with competing effects. Alternatively, spin relaxation in lead-halide perovskites may be best explained by a mechanism not yet identified [114, 115]. Thus, further exploration is needed to better understand the spin relaxation mechanisms in lead-halide perovskites.

1.5 Outline of Thesis

This thesis studies the spin dynamics in the two layer ($n = 2$) 2D lead-halide perovskite $\text{BA}_2\text{MAPb}_2\text{I}_7$. The objective of the thesis is to determine the spin relaxation lifetime in this material and characterize its dependency on parameters such as excess photon energy, carrier density and sample temperature. Based on this characterization, the dominant spin relaxation mechanism in $\text{BA}_2\text{MAPb}_2\text{I}_7$ will be determined. Understanding the fundamental spin properties and relaxation mechanisms is paramount in determining the viability of using this material in spintronic applications.

The thesis will begin with a review of semiconductor theory including the effect of spin-orbit coupling on semiconductor band structure in Chapter 2. It will then consider the scenario of optical excitation and outline how the requirement of conservation of momentum during excitation produces optical selection rules enabling the creation of spin polarization. The relaxation mechanisms of charge carriers and their spin will be discussed.

In Chapter 3 the fabrication process of $\text{BA}_2\text{MAPb}_2\text{I}_7$ thin films will be provided and its physical and optical properties characterized. The laser system and optical apparatus used to study carrier and spin dynamics will be presented in Chapter 4 and the results of those experiments discussed in Chapter 5. The results will lead to the determination that D'yakonov-Perel' is the dominant spin relaxation mechanism in $\text{BA}_2\text{MAPb}_2\text{I}_7$.

Chapter 2

Background Information

The objective of this chapter is to provide an introduction to the key concepts involved in this thesis work. The chapter starts with a review of semiconductor physics appropriate to bulk (*i.e.* 3D systems), including the influence of the spin-orbit interaction on the band structure (Sec. 2.1). As the perovskite structure studied in this work is subject to quantum confinement, the effects of confinement on the band structure are described in Sec. 2.2. The process of optical excitation in semiconductors is covered in Sec. 2.3, and the processes of relaxation for charge carriers following excitation are discussed in Sec. 2.4. The optical selection rules that allow for injection of spin-polarized distributions of electrons and holes using circularly-polarized light are described in Sec. 2.5. A description of the processes governing spin relaxation, which equalize the spin up and spin down carrier populations, is provided in Sec. 2.6. The origin of spin splittings in the semiconductor energy bands tied to the spin-orbit interaction and lack of inversion symmetry (so-called Rashba and Dresselhaus splittings) are introduced in Sec. 2.7.

2.1 Review of Bulk Semiconductor Physics

A solid's band structure describes the allowable energies of electrons in that system. The versatility of semiconductor's band structure make them important materials for a vast amount of electronic applications. The allowable energies of electrons in a semiconductor, and thus the band structure, can be obtained by solving the time independent Schrödinger equation for a single electron's position dependent wavefunction, $\psi(\mathbf{r})$:

$$\left[\frac{-\hbar^2}{2m} \nabla^2 + V(\mathbf{r}) \right] \psi_{\mathbf{k}}(\mathbf{r}) = \epsilon_{\mathbf{k}} \psi_{\mathbf{k}}(\mathbf{r}) \quad (2.1)$$

for energy eigenvalues, $\epsilon_{\mathbf{k}}$, for a given mode or wavevector, \mathbf{k} . In a bulk semiconductor, ions are arranged in a periodic lattice. V is the potential due to the ionic cores of

the lattice along with all of the screening electrons in the lattice. The potential, V , is periodic such that $V(\mathbf{r}) = V(\mathbf{r} + \mathbf{R})$. Solutions of the Schrödinger equation for a periodic potential as in Eq. 2.1 are the Bloch functions given as

$$\psi_{n\mathbf{k}}(\mathbf{r}) = U_{n\mathbf{k}}(\mathbf{r}) \exp(i\mathbf{k} \cdot \mathbf{r}) \quad (2.2)$$

where $U_{n\mathbf{k}}(\mathbf{r})$ is the cell function for band n , which shares the periodicity of $V(\mathbf{r})$. V is relatively small and the lattice potential is thus a weak perturbation of the free electron model. The effect of this perturbation is a slight modification of the curvature of the electron dispersion relation and the presence of energy gaps in the band structure in which no electronic states exist. Indeed, the Bloch solutions in Eq. 2.2 describe the allowable states of the electron in the “nearly-free” electron model. When this model is reduced to the first Brillouin Zone we obtain the simple band structure of a semiconductor shown in figure 2.1. At zero temperature, there are exactly the correct number of electrons to fill an integer number of bands. The lowest unoccupied band is called the conduction band and the highest occupied band is called the valence band. The region in between the valence and conduction bands where no states exist is known as the band gap.

In a simplified band diagram, such as in figure 2.1, only the top most part of the valence band and the bottom of the conduction band are shown. Such a description is adequate to capture many of the essential physical processes involved in semiconductor optoelectronic devices because only these band edge states are involved in light absorption and charge transport. In semiconductors, these band gaps are small (~ 1 eV) which leads to the versatility of electronic properties. Subtle changes in conditions including temperature, impurities, and light can cause drastic changes in these electronic properties, and this tunability allows semiconductor materials to be used in a wide variety of applications.

The interaction between the intrinsic angular momentum, or spin, of an electron and its orbital motion is known as spin-orbit coupling (SOC). The magnetic moment of the electron’s spin, μ_s , couples to the effective magnetic field from the motion of the charged electron, $\mathbf{\Omega}$. This interaction is described by the Hamiltonian

$$H_{SO} = -\mu_s \cdot \mathbf{\Omega} \quad (2.3)$$

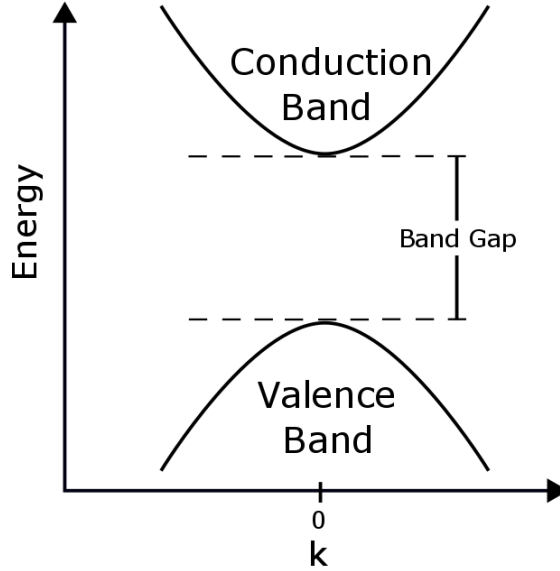


Figure 2.1: Simplified band structure of a semiconductor showing the highest-energy states in the valence band and the lowest-energy states in the conduction band.

In semiconductors, we can write Eq. 2.3 in the form

$$H_{SO} = \frac{\hbar}{4m^2c^2} \nabla V \times \mathbf{p} \cdot \sigma \quad (2.4)$$

where V is the periodic lattice potential from Eq. 2.1, $\mathbf{p} = -i\hbar\nabla$ is the momentum operator and σ are the Pauli spin matrices. In semiconductors, the primary effect of SOC is to split energy bands that would otherwise be degenerate. These splittings arise because the appropriate eigenstates including SOC are states of total angular momentum (\mathbf{J}), which is the sum of the spin (\mathbf{S}) and orbital angular momentum (\mathbf{L}). In lead-halide perovskites, the cell function for the conduction band is “p-type”, for which $l = 1$ and the valence band is “s-type”, for which $l = 0$ where l is the angular momentum quantum number of operator \mathbf{L} [116]. The effect of SOC is to split the conduction band states into $j = 3/2$ states and $j = 1/2$ states where j is the total angular momentum quantum number. The energy splitting between the $j = 3/2$ and $j = 1/2$ bands at $\mathbf{k} = 0$ is given by Δ_{SO} .

Figure 2.2 shows the calculated electronic band structure of 2D lead-iodide perovskite (a) without and (b) with SOC, obtained by Even *et.al.* using DFT, a computational technique capable of calculating the electronic structures of a wide array

of solid-state systems [116]. This illustrates the massive energy splitting in the conduction band due to spin orbit coupling in 2D lead-halide perovskites. Figure 2.2 also shows the crucial role SOC plays in properly determining the bandgap energy in perovskite materials.

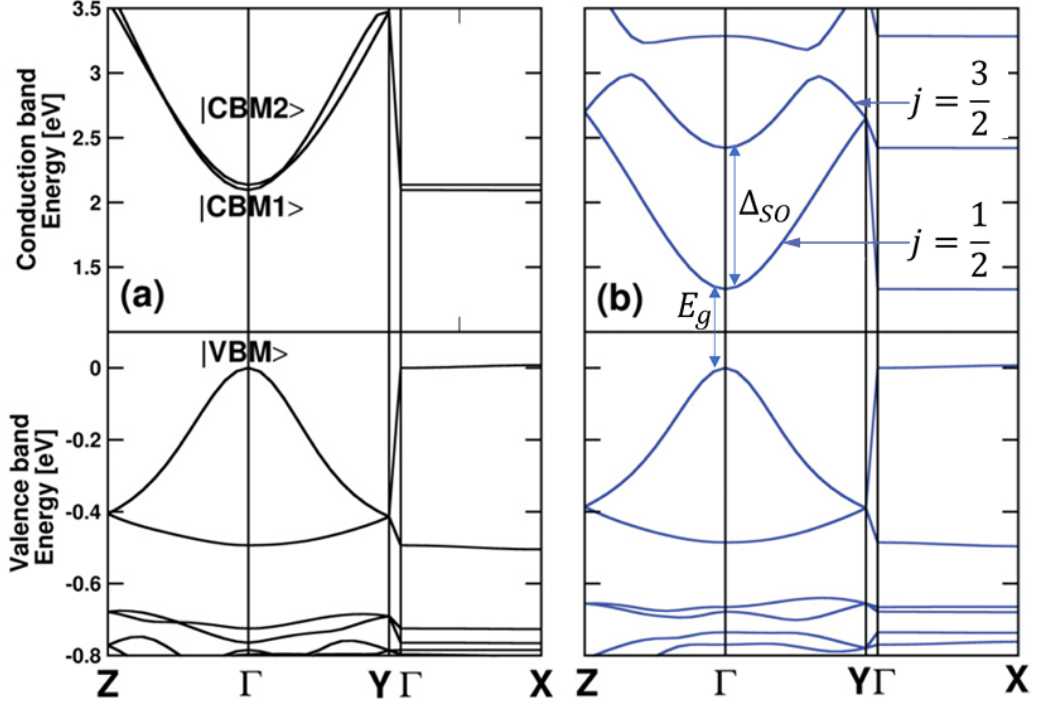


Figure 2.2: Results of calculations of the electronic band structure of the 2D perovskite 4F-PEPI ($[\text{pFC}_6\text{H}_5\text{C}_2\text{H}_4\text{NH}_3]_2\text{PbI}_4$) using density functional theory without (a) and with (b) the inclusion of spin-orbit coupling. Adapted from Ref. [116].

2.2 Effects of Confinement on Semiconductors

In section 2.1, we considered bulk (*i.e.* 3D) semiconductors in which all three spatial dimensions are macroscopic. When one or more of the spatial dimensions is reduced to a length scale on the order of the wavelength of the electron, the electronic and photonic properties can be dramatically altered. The Bloch function solutions describing the electron in this type of semiconductor have finite boundary conditions. The resulting spatial confinement of the electron (also referred to as quantum confinement) alters the allowed quantum states, leading to discretization of the allowed energy levels. These confinement effects occur for each band in the corresponding

bulk semiconductor. If we consider a band characterized by effective mass m^* , the result of confining a nearly-free electron in one dimension, z , within a length, L , quantizes the allowable wavevectors,

$$\mathbf{k}_{n_z} = \frac{2\pi}{\lambda_{n_z}} = \frac{n_z\pi}{L}, n_z \in \mathbb{N} \quad (2.5)$$

resulting in discrete allowable energy states for the electron:

$$E_{n_z} = \frac{\hbar^2 \mathbf{k}_{n_z}^2}{2m^*} = \frac{\hbar^2 \pi^2}{2m^* L} \quad (2.6)$$

Structures with spatial confinement in one direction are known as quantum wells. Quantum wells can exist in materials which are layered such that particles are confined to move in a plane. The 2D family of halide-perovskites are examples of such materials. Quantum confinement in one-dimension leads to energy subbands for each band of the corresponding bulk semiconductor, a result of the discretization of the Bloch wavefunctions.

2.3 Optical Excitation in Semiconductors

Optical excitation is the process by which a photon is absorbed by a semiconductor resulting in the excitation of an electron from the valence band to a higher energy state. In a bulk semiconductor optical excitation of electrons from the valence to conduction band can only occur if the photon energy is at least as large as the band gap energy. Thus the maximum wavelength of the photon for such a transition is

$$\lambda_{max} = \frac{hc}{E_g} \quad (2.7)$$

where E_g is the energy gap. The electron excited to the conduction band leaves behind a hole in its place in the valence band. The hole in fact describes all of the remaining electrons in the valence band. Since the hole is a missing electron it has the opposite charge. When optical excitation excites an electron-hole pair, the electron and hole propagate throughout their respective bands as free carriers. Alternatively, optical excitation can lead to the creation of an exciton which is a hydrogenic pseudoparticle consisting of a bound electron-hole pair. The electron and hole in the exciton are bound together by the Coulomb interaction. The bound exciton

is at a lower potential energy than free carriers, by an amount equal to the exciton binding energy, and thus the associated optical transition has an energy lower than the semiconductor band gap. In 3D perovskites the exciton binding energy has been shown to be comparable to or smaller than the thermal energy at room temperature. However, in 2D perovskites the exciton binding energy is extremely large [61] up to a few hundred meV due to the strong quantum confinement in these structures, which increases the overlap of the electron and hole wavefunction and also therefore the strength of their Coulomb interaction.

One can use differential transmission spectroscopy to probe the occupation of electrons or holes in the semiconductor as a function of the energy above the band gap. Since laser pulses are used in these experiments, this occupation may be probed as a function of time after excitation (*i.e.* this is a time-resolved technique). These experiments exploit the Pauli exclusion principle, by which a given state can only be occupied by one electron at a time (or one hole at a time in the valence band). Thus, if a particular optical transition above the band gap is already occupied by an electron-hole pair, the material no longer can absorb that wavelength. In practice, because the semiconductor consists of energy bands, there is a large number of electron-hole pair transitions very close in energy. Nevertheless, if carriers are already occupying band states at a given transition energy, the absorption will be reduced at that energy since there is a finite density of electronic states in the valence and conduction bands. In this way, optical excitation changes the semiconductor's absorption coefficient and this change in absorption is directly related to the excited electron population. This is the basis of differential transmission spectroscopy.

Since photons are spin 1 particles they carry angular momentum. In order for angular momentum to be conserved, during optical excitation the photon's momentum is transferred to the electron and hole when the photon is absorbed. This requirement for angular momentum conservation results in optical selection rules for optical excitation. The optical selection rules for the lowest-energy conduction band (with $j = 1/2$) and top most valence band (with $j = s = 1/2$) is shown in Figure 2.3. Left circular polarization (LCP), σ^+ , and right (RCP), σ^- , transfer +1 and -1 angular momentum respectively, in units of \hbar , to the electron-hole pair. Linearly polarized light, π , composed of equal parts LCP and RCP carries no net momentum and excites an

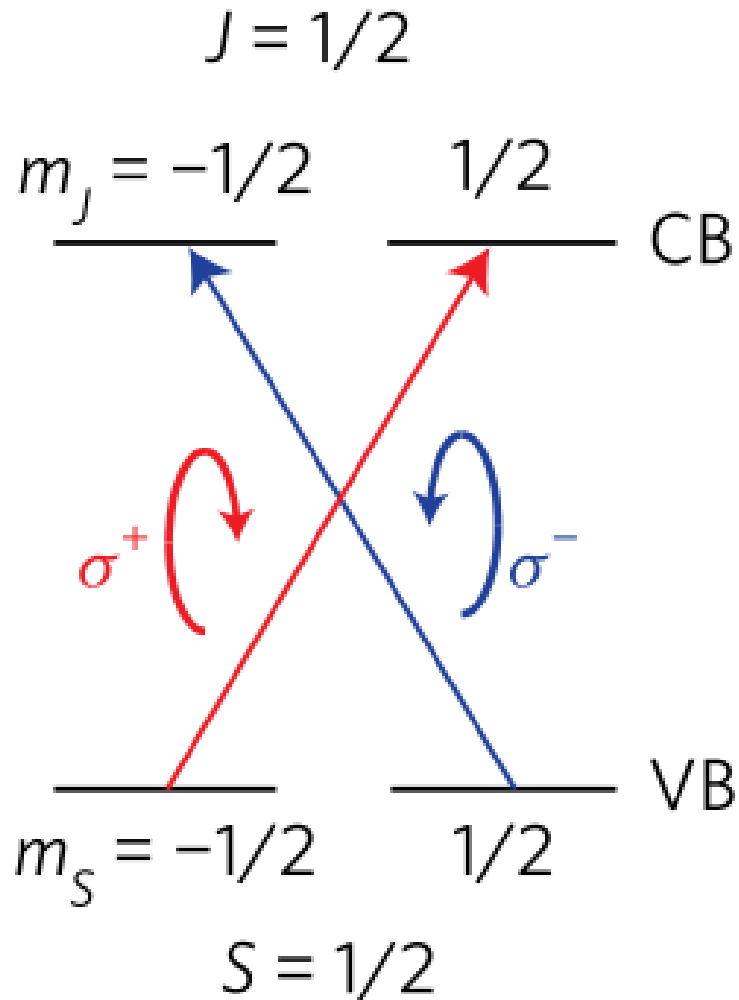


Figure 2.3: Schematic representation of the optical selection rules for the lowest conduction band and the highest valence band in perovskite semiconductors. Adapted from Ref. [57].

equal population of carriers of both spin polarizations. These optical selection rules are derived by calculating the dipole matrix element for the relevant transition. A non-zero matrix element corresponds to an allowed transition.

Recall from Figure 2.2, there exists a split-off energy band with total angular momentum $j = 3/2$ in addition to the valence band, VB, and conduction band, CB, in Figure 2.3. However, since in 2D perovskites Δ_{SO} is so large (on the order of an eV), the states are not excited when laser photon energy is similar to the band gap energy. In this case the optical selection rules of the split-off energy state need not

be considered.

When optically exciting with a single type of circularly-polarized light (σ^+ or σ^-), a population imbalance between spin up and spin down electrons in the conduction band will arise. This population imbalance leads to an imbalance in absorption between LCP and RCP photons. The difference in absorption between LCP and RCP light is directly related to the difference in excited spin populations and is the basis of circular differential transmission spectroscopy.

2.4 Charge Carrier Relaxation

When carriers in a semiconductor are excited with an ultrashort optical pulse they undergo several relaxation processes [117]. The initial kinetic energy of the electron (and hole) following optical excitation by a photon of a particular energy will be dictated by the difference in energy between the state the carrier is excited into and the edge of the associated band. If a population of electrons is excited with a laser pulse, there will be a range of such kinetic energies, but it will be narrow, dictated by the spectrum of the laser pulse. If this kinetic energy is larger than the thermal energy, then the carrier distribution is “hot”. Rapid scattering between carriers redistributes the energy between carriers in the population, ultimately spreading out the carriers energetically within the band states with an energy profile described by a Fermi distribution. The temperature of that distribution will initially be characterized by the carrier temperature, and so will be “hot”. The carriers then exchange energy with the lattice through phonon absorption and emission until the temperature of the carrier distribution is the same as the lattice. The resulting carrier distribution is then said to be thermalized. In conventional inorganic semiconductors, energy exchange with the lattice occurs on a time scale of 1 to 100 ps [117]. On longer time scales (typically hundreds of picoseconds or longer) electron-hole pairs recombine, returning the semiconductor to equilibrium. The time it takes for an excited electron-hole pair to recombine is referred to as the carrier lifetime, τ .

Assuming that the carrier lifetime is independent of time, the total charge carrier population (*i.e.* the number of electron-hole pairs), N will be described by the following differential equation:

$$\frac{d}{dt}N = -\frac{N}{\tau} \quad (2.8)$$

Solving this differential equation for an initial population N_0 , yields the following result:

$$N(t) = N_0 \left[\exp\left(-\frac{t}{\tau}\right) \right] \quad (2.9)$$

The process of thermalization causes the initial carrier population in the optically-coupled states to decay due to energetic redistribution of the carriers within their respective bands. We denote the thermalization time by τ_{th} . In this case, the full charge carrier relaxation dynamics can be describe by the following double exponential expression:

$$N(t) = N_0 \left[\exp\left(-\frac{t}{\tau}\right) + \exp\left(-\frac{t}{\tau_{th}}\right) \right] \quad (2.10)$$

2.5 Spin Populations

Under excitation with LCP or RCP light, spin-polarized electron-hole pairs are generated. We can describe the degree of spin polarization of the carrier population by relating the populations of spin up (N^+) and spin down (N^-) carriers using:

$$P = \frac{N^+ - N^-}{N^+ + N^-} \quad (2.11)$$

We can use differential transmission experiments to probe the degree of spin polarization as a function of time after excitation by a pump laser pulse by probing the state-filling signal. As discussed above, state filling describes the reduction in absorption due to the Pauli exclusion principle when the electronic states coupled by the laser field are occupied. The degree of state filling is detected using a weak laser pulse, called the probe pulse. The small change in probe transmission caused by the pump-laser-excited carriers is detected using lock-in amplifier techniques, and constitutes the “state-filling signal”. The difference between the state filling signal observed when the pump and probe pulses are co-circularly and counter-circularly polarized provides a direct measurement of P . From the optical selection rules, excitation with circularly-polarized light excites carriers that are 100% spin polarized. The electrons

and holes then undergo spin relaxation, leading ultimately to an equilibrium state of equal spin up and spin down populations. The rate of spin relaxation can differ for electrons and holes in the general case. Taking the spin relaxation rates for the two types of carrier to be the same for simplicity, we can describe the rate of change of the populations of spin up (N^+) and spin down (N^-) electron-hole pairs by

$$\begin{aligned}\frac{dN^+}{dt} &= -\frac{N^+}{\tau} - \frac{N^+ - N^-}{\tau_s} \\ \frac{dN^-}{dt} &= -\frac{N^-}{\tau} + \frac{N^+ - N^-}{\tau_s}\end{aligned}\quad (2.12)$$

where τ again is the carrier recombination time and τ_s is the spin relaxation time, which is generally much smaller than τ [89]. Adding equations 2.12 gives,

$$\frac{d}{dt}(N^+ + N^-) = -\frac{(N^+ + N^-)}{\tau} \quad (2.13)$$

which is exactly the carrier recombination rate Eq. 2.8 from earlier. Subtracting equations 2.12 yields,

$$\frac{d}{dt}(N^+ - N^-) = -\left(\frac{1}{\tau} + \frac{2}{\tau_s}\right)(N^+ - N^-) \quad (2.14)$$

Integration of equations 2.13 and 2.14 results in the following solutions for the spin populations:

$$\begin{aligned}(N^+ + N^-) &= N_0 \exp\left(-\frac{t}{\tau}\right) \\ (N^+ - N^-) &= N_0 \exp\left(-\frac{t}{\tau}\right) \exp\left(-\frac{2t}{\tau_s}\right)\end{aligned}\quad (2.15)$$

and from Eq. 2.11 we obtain the relationship between spin lifetime, τ_s , and the net spin polarization:

$$P = \exp\left(-\frac{2t}{\tau_s}\right) \quad (2.16)$$

If electrons and holes undergo spin relaxation at different rates, then the signal observed in the pump probe experiments will decay partially due to the loss of polarization of each carrier type. In this case, the equation above will be replaced by:

$$P = C_e \exp\left(-\frac{2t}{\tau_{s,e}}\right) + C_h \exp\left(-\frac{2t}{\tau_{s,h}}\right) \quad (2.17)$$

where $\tau_{s,e}$ ($\tau_{s,h}$) are the spin lifetimes of electrons (holes), and the coefficients C_e and C_h describe the relative fraction of the total differential transmission signal tied to each carrier type, where $C_e + C_h = 1$. The values of C_e and C_h are determined by the electronic band structure since the density of states in each of the valence and conduction bands at the optical transition corresponding to the laser photon energy will differ if the effective masses of the valence and conduction bands differ.

2.6 Spin Relaxation

There are three primary mechanisms of spin relaxation that have been identified for electrons and holes in semiconductors. These are Bir-Aronov-Pikus (BAP), Elliott-Yafet (EY), and D'yakonov-Perel' (DP) [84], named according to the researchers who discovered each mechanism. The first is caused by the exchange interaction between the electron and hole, and the other two are tied to the spin-orbit interaction. Each of these mechanisms is described in the following sections.

2.6.1 Bir-Aronov-Pikus

In the Bir-Aronov-Pikus spin relaxation mechanism, holes and electrons undergo spin-flip scattering interactions via the Coulomb exchange coupling between the electron and hole. This process therefore leads to spin flip of the electron-hole pair as a whole. This relaxation mechanism was first described in the context of spin relaxation of electrons in p-doped semiconductors by Bir *et.al.* in 1975 [118]. The interaction Hamiltonian governing the spin exchange between electrons and holes is

$$H = C\mathbf{S} \cdot \mathbf{J}\delta(\mathbf{r}) \quad (2.18)$$

where C is proportional to the exchange integral between conduction and valence bands, \mathbf{S} is the spin operator, \mathbf{J} is the hole angular momentum operator, and \mathbf{r} is the relative displacement between electrons and holes [84]. This Hamiltonian results in a spin relaxation rate for electrons given by:

$$\frac{1}{\tau_s} \propto N_p a_B^4 \frac{\Delta_{ex}^2}{E_B} k \quad (2.19)$$

where N_p is the free hole concentration, $a_B = \hbar^2 \epsilon m / e^2$ is the exciton Bohr radius, Δ_{ex} is the exchange splitting of the excitonic ground state, and $E_B = \hbar^2 / (2ma_B^2)$ is the exciton binding energy [57]. BAP is extremely important for electron spin relaxation in p-doped semiconductors in which the free hole concentration is high.

2.6.2 Elliott-Yafet

The Elliott-Yafet mechanism of spin relaxation is caused by the spin-orbit interaction, together with scattering processes that cause carriers to undergo transitions between different \mathbf{k} -states within a given band (the conduction band for electrons and the valence band for holes) [119, 120]. We can understand the origins of this mechanism by considering the Schrödinger equation in which SOC is included, given by

$$\left[\frac{\mathbf{p}^2}{2m} + V(\mathbf{r}) + H_{SO} \right] \psi_{\mathbf{k}}(\mathbf{r}) = \epsilon_{\mathbf{k}} \psi_{\mathbf{k}}(\mathbf{r}) \quad (2.20)$$

where H_{SO} was given in Eq. 2.4. Inserting a Bloch wave function solution (Eq. 2.2) gives

$$[H^0(\mathbf{k}) + H_{SO}(\mathbf{k})] U_{n\mathbf{k}}(\mathbf{r}) = \epsilon_n(\mathbf{k}) U_{n\mathbf{k}}(\mathbf{r}) \quad (2.21)$$

which is a new differential equation for the cell function $U_{n\mathbf{k}}(\mathbf{r})$, and

$$H^0(\mathbf{k}) = \frac{(\hbar\mathbf{k} + \mathbf{p}^2)}{2m} + V \quad (2.22)$$

and

$$H_{SO}(\mathbf{k}) = \frac{\hbar}{4m^2c^2} \nabla V \times (\hbar\mathbf{k} + \mathbf{p}) \cdot \sigma \quad (2.23)$$

The Schrödinger equation for the cell function in Eq. 2.21 may be solved using perturbation theory, taking the set of cell functions solutions for the bands at $\mathbf{k} = 0$ as a basis set and treating the spin-orbit interaction as a perturbation. In this case, while the spin states of the bands are well-defined at $\mathbf{k} = 0$ (given in Figure 2.3), the perturbative solutions away from $\mathbf{k} = 0$ have non-zero components of the $\mathbf{k} = 0$ basis functions in other bands. For instance, the conduction states for nonzero \mathbf{k} will have a term proportional to the zero- \mathbf{k} top-most valence band basis state (including states with both spin directions in general). From perturbation theory, the magnitude of the coefficients of the other bands will be dictated by the strength of the spin-orbit

interaction and the energy difference between the associated bands at zone center. Due to this spin mixing, the band states are no longer states of well-defined spin (*i.e.* well-defined total angular momentum). In this case, scattering via any process (even a spin-independent process, such as electron-phonon scattering) that causes a carrier to undergo a transition to another \mathbf{k} state within the band will have a non-zero probability of flipping the spin. The larger the coefficient of the opposite spin component, the larger the rate of scattering-induced spin relaxation. Momentum scattering can occur due to coupling of the carriers with other carriers, phonons, or defects.

Analytical calculations of the spin relaxation lifetime for electrons in III-V semiconductors due to mixing with the valence band states [121,122] yielding the following result:

$$\frac{1}{\tau_s(\epsilon_{\mathbf{k}})} = F \left(\frac{\Delta_{SO}}{E_g + \Delta_{SO}} \right)^2 \left(\frac{\epsilon_{\mathbf{k}}}{E_g} \right)^2 \frac{1}{\tau_p(\epsilon_{\mathbf{k}})} \quad (2.24)$$

where τ_p is the average momentum scattering time in state $\epsilon_{\mathbf{k}}$, E_g is the band gap energy, Δ_{SO} is the energy of the valence band splitting due to spin-orbit coupling, and F is a numerical factor dependent on the type of scattering mechanism. Eq. 2.24 illustrates that the Elliott-Yafet mechanism plays an important role in the spin relaxation of small band gap semiconductors with large spin-orbit coupling.

2.6.3 D'yakonov-Perel'

The D'yakonov-Perel' spin relaxation mechanism occurs in semiconductor systems which have no centre of inversion symmetry. This mechanism was first discovered by D'yakonov and Perel in 1972 [123]. The spin-orbit coupling results in an effective magnetic field ($\mathbf{\Omega}(\mathbf{k})$, for a given momentum state \mathbf{k} in the band) that is experienced by an electron in that state. Inversion symmetry may be broken in a variety of different ways. If the crystal structure itself lacks inversion symmetry (due for example to polar bonding), it is referred to as bulk inversion asymmetry. It is also possible to have structural inversion asymmetry by creating a layered semiconductor structure, and one can “turn on” inversion asymmetry by applying an electric field to the semiconductor using a gated structure. In all of these cases, there are electric fields within the crystal that electrons move through as they propagate. Within the spin-orbit Hamiltonian in Eq. 2.4, these electric fields play the role of ∇V . For a

given (non-zero) momentum, $\mathbf{\Omega}(\mathbf{k})$ has a magnitude and direction determined by the crystallographic direction about which symmetry is broken, the strength of the internal electric fields, and the magnitude and direction of the electron momentum. The effective magnetic field lifts the degeneracy of the two spin states (*i.e.* the spins parallel and antiparallel to $\mathbf{\Omega}(\mathbf{k})$), leading to a spin splitting in the bands that increases with increasing $|\mathbf{k}|$.

The effective magnetic field, $\mathbf{\Omega}(\mathbf{k})$, causes the spin of an electron within the band at \mathbf{k} to precess. The rate of precession corresponds to the Larmor frequency, given by $\frac{e}{m} |\mathbf{\Omega}(\mathbf{k})|$. When a circularly-polarized light pulse is used to excite a spin population, conservation of momentum indicates that the carrier spins will all be parallel or antiparallel to the propagation direction of the optical beam depending on the sense of circular polarization (left or right). Once injected, carriers at different \mathbf{k} precess about different effective magnetic fields (with different magnitudes and directions). This precession ultimately causes the initially spin-polarized distribution to become random.

Momentum scattering interrupts the spin precession and thus reduces the rate of spin relaxation such that the spin lifetime is inversely proportionate to the scattering time:

$$\frac{1}{\tau_s} \propto \tau_p \frac{e^2}{m^2} \overline{\Omega^2(\mathbf{k})} \quad (2.25)$$

where $\frac{e^2}{m^2} \overline{\Omega^2(\mathbf{k})}$ is the mean square precession frequency. This is fundamentally different from EY spin relaxation in which the spin lifetime is proportional to the scattering time. In EY spin relaxation occurs during scattering events, while in DP spin relaxation occurs between scattering events. For DP spin relaxation, scattering resets the spin precession axis and precession rate, reducing the effectiveness of the DP relaxation process.

2.6.4 Expectations for the Strength of BAP, EY and DP for 2D Perovskites

A broad objective of this thesis work is to determine the operative spin relaxation mechanism in the $\text{BA}_2\text{MAPb}_2\text{I}_7$ sample studied. Prior to interpretation of the measured results, it is useful to derive insight from existing studies in III-V semiconductors, in which the rate of spin relaxation via all three processes have been studied extensively [124]. This will provide a starting point to understand what is expected for the organic-inorganic perovskite class of materials.

The BAP mechanism is tied to spin-flip interactions between electrons and holes caused by the exchange interaction, with a rate described by Eq. 2.18. The exchange coupling between electrons and holes was recently measured to be very small in 3D $\text{MAPbI}_{3-x}\text{Cl}_x$ perovskite by Odenthal *et.al.* [57] leading to the conclusion in that work that the BAP mechanism does not contribute significantly to spin relaxation in the 3D material. Since the exciton binding energy is much larger in 2D perovskite systems ($\sim 80\text{-}200$ meV) [61] compared to 15 meV in 3D perovskite [125, 126], and as a result the Bohr radius is also smaller, from Eq. 2.19 the BAP mechanism is expected to be even weaker in our sample. As a result, it is not discussed further in this thesis. This leaves two remaining candidate mechanisms: EY and DP, both of which are linked to the spin-orbit interaction.

The EY mechanism is tied to mixing of the spin states away from the band extremum. The rate of EY is determined by the degree of spin mixing and the rate of scattering, as each scattering event of a single carrier contributes to partial loss of the spin polarization of the ensemble. The degree of mixing becomes stronger the larger the size of the spin-orbit splitting (Δ_{SO} in Figure 2.2) and the smaller the bandgap, as the former reflects the strength of the spin-orbit interaction and the latter occurs in the denominator in the perturbation theory treatment as the energy separation between the states being mixed (i.e. the conduction and valence bands).

The strength of the EY mechanism is therefore tied closely to the band structure of the material. The band structure of the III-V semiconductors is different than in perovskites because the highest energy valence bands are the heavy-hole and light-hole bands characterized by total angular momentum $j = 3/2$, with the conduction band corresponding to $j = 1/2$. The heavy-hole and light-hole valence bands are

degenerate in the bulk, unstrained semiconductor, and are separated by a few 10s of meV in semiconductor quantum wells [127]. As a result of the close proximity of these valence states, the spin mixing in both the heavy-hole and light-hole valence bands is very strong. This leads to rapid *hole* spin relaxation via the EY mechanism in III-V materials [128]. For the conduction band, the degree of spin mixing is much lower since the dominant contribution to mixing of conduction states involves the light-hole and heavy-hole valence bands, which are separated from the conduction states by the bandgap. EY has been found to contribute for electrons only for very small bandgap materials characterized by a large spin-orbit interaction, including HgCdTe and InSb [121, 129], but has been found to contribute negligibly in comparison to DP and BAP in larger bandgap materials such as GaAs [124].

The inverted band structure of the organic-inorganic perovskites is expected to lead to weak spin relaxation for both electrons and holes since the relevant energy separation in perturbation theory is the bandgap for both the conduction and valence states. This situation is thus similar to the case of electrons in the conduction band in GaAs. As a general guide to the relative strength of spin mixing in perovskite materials, we can use the predicted dependence of the spin-flip matrix element for electrons in III-V materials on the spin-orbit splitting Δ_{SO} and the bandgap, E_g , from [121]. Taking values of $\Delta_{SO} = 0.966$ eV and $E_g = 2.35$ eV for a similar 2D perovskite (PEPI) from [116], and the known values for GaAs ($\Delta_{SO} = 0.34$ eV; $E_g = 1.51$ eV) [130], the EY relaxation process is expected to be approximately 2 times stronger in the 2D perovskites in comparison to GaAs. While values for Δ_{SO} are not available for the 2D perovskite material studied here (containing the butylammonium organic spacer instead of phenoethylammonium, and two layers of the lead-iodide octahedral instead of one for PEPI), the values for PEPI should provide a reasonable guide to gauge the strength of spin mixing and EY spin relaxation in our material.

The DP spin relaxation mechanism is caused by precession of the spin moment of carriers about an effective magnetic field, $\mathbf{\Omega}$, that originates from the spin-orbit interaction in systems lacking a centre of inversion symmetry. This effective magnetic field vanishes at the band extremum and increases in magnitude with \mathbf{k} away from the extremum. The effective magnetic field lifts the degeneracy of the two spin states, leading to a spin splitting that increases with increasing magnitude of wavevector away

from the extremum. In a spin-resolved pump-probe experiment, the initial alignment of the electron (hole) spins by the excitation laser field is parallel (antiparallel) to the laser propagation direction. Since the direction of $\mathbf{\Omega}$ depends on the magnitude and direction of \mathbf{k} , this precession randomizes the spin orientation of the ensemble of carriers. The strength of the DP mechanism is dictated by both the magnitude of the effective magnetic field and the rate of scattering. Scattering serves to slow the rate of spin relaxation since the carrier spins are unable to precess between scattering events when scattering is rapid, referred to as motional narrowing. The average magnitude of the effective magnetic field in the range of k-space occupied by the carrier distribution dictates the rate of precession between scattering events.

In III-V semiconductors, the inversion symmetry is lifted because of the inequivalent charges on the Ga and As ions in the face-centred cubic crystal structure. This leads to a spin splitting in the conduction band for GaAs quantum wells that is less than 1 meV in magnitude within 100 meV of the bandgap [124], (Figure 4.12). The associated effective magnetic field leads to precessional spin relaxation via the DP mechanism that is stronger than all other processes in GaAs for temperatures ranging from 300 K to 30 K. DP becomes weak at very low temperatures (< 30 K) as the thermalized carrier population extends over a smaller range of k values, where the magnitude of the effective magnetic field is small. For $T < 30$ K, BAP has been shown to dominate [131], with EY contributing negligibly to the relaxation rate at all temperatures.

As the 2D perovskite, $\text{BA}_2\text{MAPb}_2\text{I}_7$, studied in this work is inversion asymmetric with a polar C_{2v} structure [76], the DP process will be operative. The inversion asymmetry is caused by tilting of the corner-sharing $[\text{PbI}_6]^{4-}$ octahdra [116]. Due to the large strength of the spin-orbit interaction, the spin splittings in these 2D materials caused by this symmetry breaking have been predicted to be extremely large, in the range of 10s of meV [132]. For example, the spin splitting was calculated for Bz_2PbCl_4 ($\text{Bz} = \text{C}_6\text{H}_5\text{CH}_2\text{NH}_3$) in the β phase with C_{2v} symmetry to be approximately 50 meV [112]. No calculations of the size of the spin splittings have yet been reported for the $\text{BA}_2\text{MAPb}_2\text{I}_7$ structure studied in this work. The exact value of the spin splitting will depend on both the constituent inorganic atoms (i.e. Pb vs Sn and I vs Br or Cl), whose orbitals form the conduction and valence states [116], and the

organic spacer component, which has been found to influence the relative rotation and tilt of the inorganic octahedral [76]. Nevertheless, the consistently large values of the spin splittings in inversion-asymmetric phases of a wide range of 2D perovskites [132] suggests that similar splittings would be found in our material. Taking into account the much smaller size of the spin splittings in GaAs quantum wells, the DP mechanism is expected to be at least 10-fold stronger in these 2D perovskites. We thus anticipate that DP will dominate all other mechanisms in our sample.

2.7 Rashba/Dresselhaus Spin Splitting

The splitting in the band states resulting from the spin-orbit interaction and lack of inversion symmetry (the same splitting responsible for DP spin relaxation) can be calculated using advanced electronic structure models. For perovskites, symmetry is typically broken due to distortions of the lead-iodide octahedra, and it is necessary to compare DFT simulations with X-ray diffraction measurements very carefully to obtain correct predictions for the spin splitting. These spin splittings are often referred to as Rashba or Dresselhaus splittings following the analytic treatment of the spin splitting in inorganic semiconductors associated with structural inversion asymmetry (Rashba) [133, 134] and bulk-inversion asymmetry (Dresselhaus) [135]. In the perovskite literature, the convention for labeling the spin splitting is not uniform (*e.g.* sometimes it is referred to as a Rashba splitting even when caused by the intrinsic crystal asymmetry).

To understand the origin of the spin splitting, it is instructive to consider a simple 2D system such as a semiconductor quantum well in which transport occurs in the x-y plane and the structural inversion asymmetry is along the growth direction (introduced *e.g.* through the application of an electric field along the z-direction), so that the relevant wavevector is $\mathbf{k}_{\parallel} = k_x \hat{x} + k_y \hat{y}$. In this case, from the symmetry of the spin-orbit Hamiltonian in Eq. 2.4, the effective magnetic field will be perpendicular to both the z-direction and the direction of the electron wavevector \mathbf{k} . The associated spin splitting is described by the Rashba Hamiltonian

$$H_R(\mathbf{k}_{\parallel}) = \lambda_R(k_x \sigma_y - k_y \sigma_x) \quad (2.26)$$

where the magnitude of the coefficient λ_R is dependent upon the material system

(including the degree of inversion symmetry breaking and the size of the spin-orbit coupling). The corresponding eigenenergies yields the following dispersion relation for the higher (+) and lower (-) energy branches

$$E_{R\pm}(\mathbf{k}_{\parallel}) = \frac{\hbar k_{\parallel}}{2m} \pm \sqrt{\lambda_R^2(k_x^2 + k_y^2)} \quad (2.27)$$

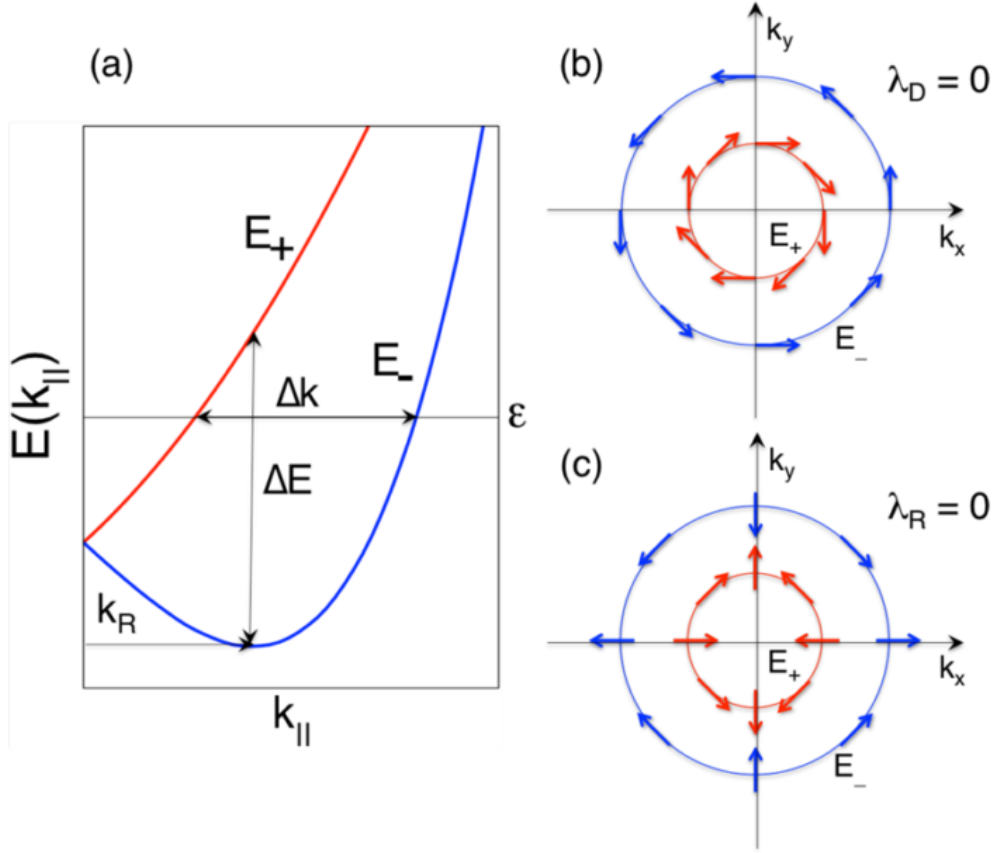


Figure 2.4: (a) The band structure near $\mathbf{k} = 0$ in a 2D system incorporating Rashba and Dresselhaus splittings, described by coefficients λ_D and λ_R , respectively. (b),(c) The direction of the effective magnetic field tied to pure Rashba (b) and Dresselhaus (c) splitting. Adapted from Ref. [112].

The Rashba coefficient is given in terms of the energy splitting $\Delta E = E_+ - E_-$ as

$$\lambda_R = \frac{\Delta E(\mathbf{k}_{\parallel})}{2\sqrt{k_x^2 + k_y^2}} \quad (2.28)$$

Rashba and Dresselhaus energy splittings for such a 2D system are shown in Fig. 2.4. Rashba/Dresselhaus spin splittings have been predicted to occur in a variety of methylammonium-based perovskite materials [80, 107, 112, 116, 136–138].

Chapter 3

Sample Fabrication and Characterization

3.1 Materials Studied

3.1.1 Precursor Crystals

The material studied in this thesis is the two layer ($n = 2$), two dimensional, butylammonium methylammonium lead iodide perovskite ($\text{BA}_2\text{MAPb}_2\text{I}_7$) with the full chemical formula $(\text{CH}_3(\text{CH}_2)_3\text{NH}_3)_2(\text{CH}_3\text{NH}_3)\text{Pb}_2\text{I}_7$. The precursor crystals were fabricated at Northwestern University following the recipe outlined in Ref. [76]. While the author of this thesis later visited Northwestern University to fabricate several samples, the precursor crystals used in this study were fabricated by the Kanatzidis group in the Department of Chemistry at Northwestern University. 2.232 g of PbO powder (10 mmol) was dissolved in 20 mL of 57% w/w aqueous HI solution (152 mmol) by heating to boiling on a hot plate (set to ~ 175 °C) with a magnetic stirrer. A small amount (~ 2 mL) of 50% aqueous H_3PO_2 is added to the solution to reduce oxygenation. The powder was allowed to dissolve for about five minutes and turned to a clear strong yellow colour. Next, 338 mg of solid $\text{CH}_3\text{NH}_3\text{Cl}$ (5 mmol) was added to the hot solution which caused a black powder to precipitate which quickly redissolved and returned the solution to its clear yellow colour. Separately 694 μL of $n\text{-CH}_3(\text{CH}_2)_3\text{NH}_2$ was mixed with 5 mL of 57% w/w aqueous HI in an ice bath to reduce loss due to evaporation. This resulted in a clear light yellow solution. This $n\text{-CH}_3(\text{CH}_2)_3\text{NH}_3\text{I}$ solution was then added to the main solution, immediately producing black precipitate. This solution was left on heat with magnetic stirring until all of the black precipitate had redissolved, returning the solution to its clear yellow colour in approximately 15 minutes. At this point the heat and magnetic stirrer were turned off but the solution was left on the hot plate to cool very slowly to room temperature. Small, rectangular, dark red plates start to crystallize at the bottom of the solution. This crystallization process takes at least two hours to complete once

cooled to room temperature but can be left longer. The crystals were then isolated via suction filtration and dried in a vacuum oven. The yield was approximately 3 g or roughly 40% based on initial lead content.

Ensuring the correct ratio of $\text{PbO}:\text{CH}_3\text{NH}_3\text{Cl}:n\text{-CH}_3(\text{CH}_2)_3\text{NH}_2$ is crucial to ensuring the desired well thickness, or layer number, n , is obtained. The thicker the 2D perovskite layer (larger n) the more subtly the ratio is altered and the more difficult it is to avoid contamination by different layer numbered materials. The purity of the material can be estimated via X-ray diffraction analysis as will be outlined in section 3.2. However, to the author’s knowledge, no quantitative analysis of the crystal purity was carried out before the particular crystals studied here were sent to Dalhousie University and further processed. Once the crystals were sufficiently dried they were placed in a vial which was then evacuated to $\sim 10^{-3}$ Torr and shipped from Northwestern University to Dalhousie University. The vials were then stored in a dry Argon glove box for about a year.

3.1.2 Thin Films

The perovskite thin film samples were prepared at Dalhousie University in Professor Ian Hill’s laboratory. To fabricate the perovskite thin films studied here, 35 mg of $\text{BA}_2\text{MAPb}_2\text{I}_7$ crystal was dissolved in 100 μL of dimethylformamide (DMF) by heating for one hour on a hot plate at 75 °C with a magnetic stirrer in a Nitrogen filled dry glove box (H_2O , $\text{O}_2 < 0.1$ ppm). Sapphire substrates were prepared and cleaned prior to the solution being dissolved. The substrates were 0.5” diameter, 0.020” thick, round sapphire windows with 60/40 polish and 1/10 wavelength per inch flatness. They were first cleaned with a brush and soap to remove large particles. Then the windows were sequentially sonicated in de-ionized water, acetone and ethanol for 10 minutes each in a Branson Sonicator 2510 sonicating bath. Finally, the substrates were treated with UV-ozone (NovaScan) for 15 minutes. To make the films, a clean sapphire window at room temperature was placed on and secured via vacuum suction to a SCS G3P spincoater inside the Nitrogen glove box. 40 μL of the hot perovskite in DMF solution (concentration ~ 0.45 M) was pipetted onto the substrate and spin-coated at 3000 rpm for 70 s. Upon deposition onto the sapphire window, the solution was a pale yellow colour, however within five seconds of spinning the solution turned

to the pure red colour of the 2D perovskite material, depicted in Figure 3.1. The sample was then transferred from the Nitrogen glove box to an Argon glove box, with as minimal exposure to air as possible, in order for it to be loaded into a sealed JANIS ST-100 cryostat for optical characterization and study. The results in this thesis all come from samples prepared in the method stated here. However, more recent analysis of film fabrication conducted at Northwestern University has determined that optimal conditions for preferred film orientation included hot-casting, a method in which the sapphire substrate is heated to 110 °C, and increasing the spin rate to 5000 rpm.

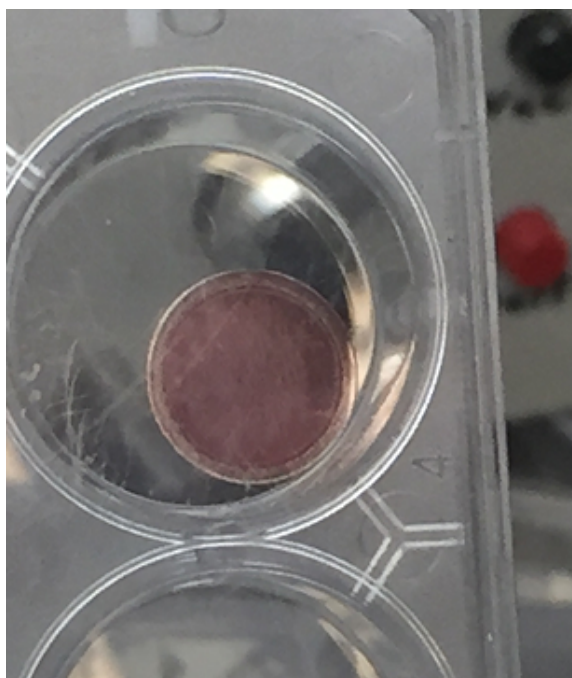


Figure 3.1: Image of $\text{BA}_2\text{MAPb}_2\text{I}_7$ thin film spin-coated onto a circular sapphire substrate

To estimate the thickness of the film, the sample height profile was obtained using a Veeco Dektak 150 profilometer. Prior to profile measurement, a cliff edge and a canyon were created in the film using a razor blade in order to estimate the height of the film from the substrate floor. Based on the profile measured, the film thickness was estimated to be ~ 500 nm, although this may be an overestimate due to the profilometer's tendency to overshoot the cliff/canyon rises. The profile also indicated there was substantial heterogeneity of film thickness throughout the film as could be seen with the naked eye as a variation in film transparency.

3.2 X-Ray Crystallography

X-ray crystallography or diffraction (XRD) is a technique used to determine the atomic structure in a crystal. When X-rays are incident on a crystal, the periodic array of atoms in the crystal cause the X-rays to diffract in a specific direction. The angle and intensity of the X-ray diffraction as a function of incident angle informs a crystallographer of the orientation and atomic separation of the crystal. This phenomenon is governed by Bragg's law, which states that X-rays which scatter off a lattice will destructively interfere except in a few specific directions,

$$\sin(\theta) = \frac{\eta\lambda}{2d}, \eta \in \mathbb{Z} \quad (3.1)$$

in which they add constructively [139]. Here d is the spacing of atomic planes and θ is the incident X-ray angle, as illustrated in the right side of Figure 3.2. As shown in Figure 3.2 at left, by rotating the X-ray source and detector so as to vary θ , the orientation and spacing of different atomic planes within the sample are determined.

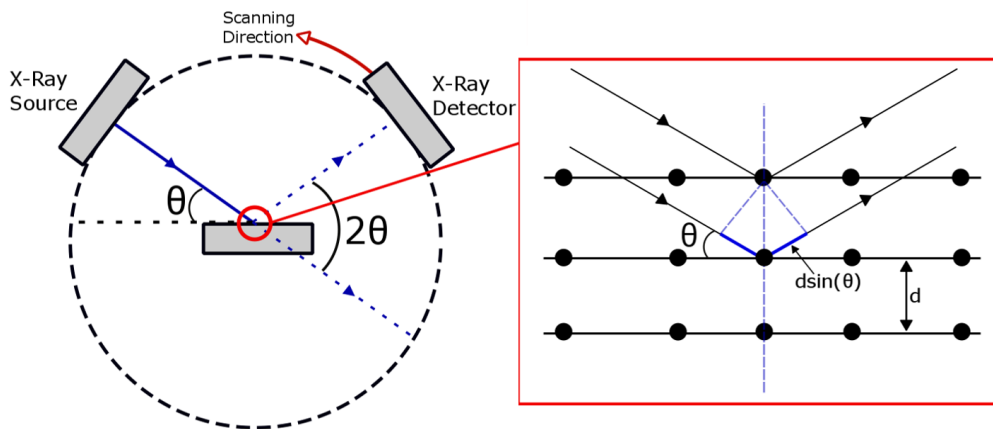


Figure 3.2: Left: Schematic of X-ray diffractometer. Right: Zoomed-in depiction of sample illustrating Bragg scattering of X-rays by crystal lattice planes.

The perovskite crystals were characterized at Northwestern University with a Rigaku Ultima IV X-Ray Diffractometer. XRD is a powerful tool for characterizing the well thickness of 2D lead iodide perovskites due to the presence of an additional low angle XRD intensity peak for each added perovskite layer. This can be seen in Figure 3.3 from [76] where there are two evenly spaced diffraction peaks for the $n = 2$ material (Pb_2I_7) below $2\theta = 13^\circ$, three for $n = 3$ (Pb_3I_{10}), and four for

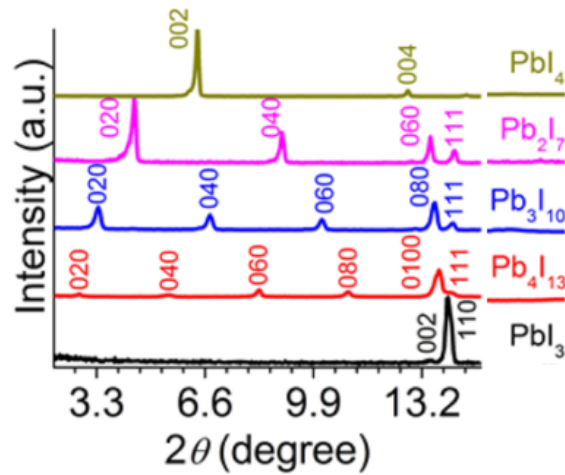


Figure 3.3: XRD intensity peaks at characteristic low angles in 2D and 3D butylammonium methylammonium lead-iodide perovskite samples, adapted from Ref. [76].

$n = 4$, (Pb_4I_{13}). The numbers above the peaks correspond to the Miller indices of the diffraction plane. The $0\kappa 0$ family of planes ($\kappa = 2, 4, 6$, etc.) are the planes of inorganic perovskite layer oriented parallel to the substrate. The higher the layer number or well thickness the more $0\kappa 0$ peaks exist at low angle since the spacing between successive planes increases and thus θ decreases as can be seen in Eq. 3.1. The planes with Miller indices 111 are oriented nearly perpendicular to the substrate but with a slight tilt. The 020 plane (red) and 111 plane (green) for the $n = 2$ lead-iodide perovskite case are shown in Figure 3.4 from [41]. The relative intensities and widths between 020 and 111 peaks provide information regarding the percentage of the material oriented in each plane. Note that the $0\kappa 0$ reflections in the $n = 2, 3, 4$ case correspond to the 00κ reflection in $n = 1, \infty$ [41] as seen in Figure 3.3.

The crystallography of the thin film 2D perovskite samples were characterized at Dalhousie University with a Siemens D5000 X-ray Diffractometer. Scans were completed with 30 kV/20 mA power, 0.05 2θ step size and 1s integration per step. The low angle characteristic intensity peaks for the $n = 2$ film are shown in Figure 3.5. Comparing the intensity peak positions to those in Figure 3.3, it is clear that $n = 2$ perovskite was fabricated. However, based on the relative intensities between the 020 and 111 peaks, it is likely that a significant percentage of the 2D perovskite layers are oriented perpendicularly to the substrate. Judging by the width of 020, even among the layers oriented parallel to the substrate there is significant tilting with

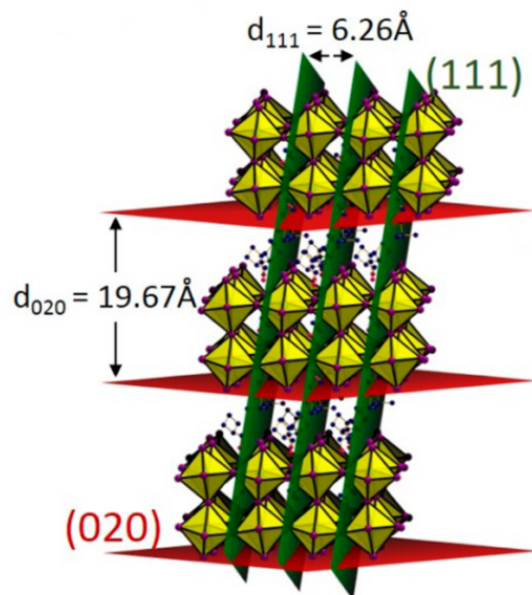


Figure 3.4: Illustration of the parallel 020 (red) and perpendicular 111 (green) oriented lattice planes with respect to the substrate in the BA₂MAPb₂I₇, adapted from Ref. [41]

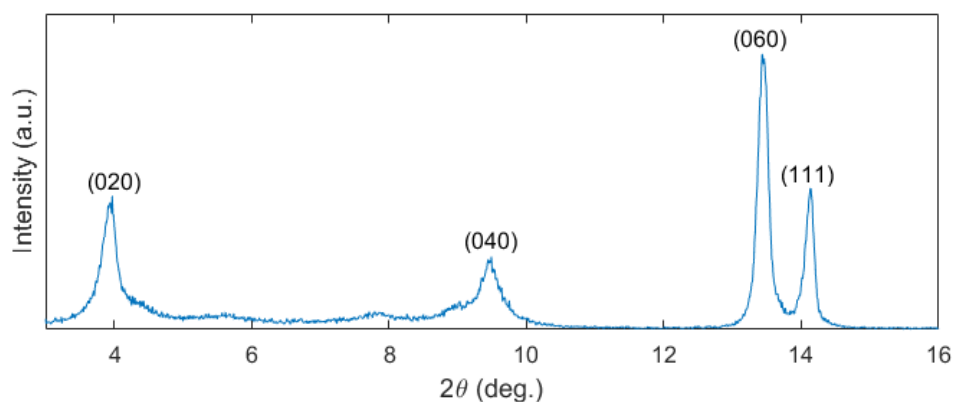


Figure 3.5: Characteristic Bragg intensity peaks of BA₂MAPb₂I₇ film using XRD

layers oriented at slightly different angles with respect to the substrate, broadening the intensity peak of the 020 diffraction plane. Finally, the two small intensity peaks between $2\theta = 5^\circ$ and 8° suggests that there is contamination of the film with other layer numbers, almost certainly $n = 1$ and 3 . These impurities may have formed during the fabrication of precursor crystals, due either to incorrect reagent ratios or incomplete dissolution. Other layers numbered perovskite can also form during the

spin coating process of film fabrication as seen by Liu *et.al.*, again possibly due to incomplete dissolution in the DMF solvent resulting in inappropriate reagent ratios in certain regions of the film [140]. Finally, sample decay due to exposure to humid air could cause other layer numbers to form if the moisture in the air dissolves the lead iodide inorganic layers leaving the remaining lead-iodide to form lower layer number 2D perovskites which require a lower inorganic to organic constituent ratio.

3.3 Absorbance

The absorbance, sometimes called optical density, of a material is a property which enables the determination of the band edge or excitonic absorption of a perovskite thin film. Although often inappropriately used interchangeably with absorption, absorbance is a measure of the attenuation of transmitted light, which is caused by absorption but also by reflection, scattering and other processes. Absorbance, A , is related to the ratio of transmitted, Φ_t , and incident, Φ_i , radiant flux by the following expression:

$$A = \log_{10} \left(\frac{\Phi_i}{\Phi_t} \right) \quad (3.2)$$

The absorbance spectrum, absorbance as a function of incident photon wavelength or energy, can then be used to create a Tauc plot, described in section 3.4 which can determine the optical bandgap in a semiconductor [141, 142]. Two different apparatuses were used to obtain the absorbance spectrum of $\text{BA}_2\text{MAPb}_2\text{I}_7$ which are outlined below.

3.3.1 Cary 60 UV-Vis

The Cary 60 UV-Vis Spectrophotometer works by illuminating the sample with a Xenon flash lamp and measuring the transmission as a function of wavelength and using Eq. 3.2 to obtain the absorbance. The lamp has a spot size of less than 1.5 mm \times 1.0 mm at its focus and covers the range of wavelengths from 190 to 1100 nm. The Cary 60 UV-Vis resides in Professor Ian Hill's laboratory at Dalhousie University.

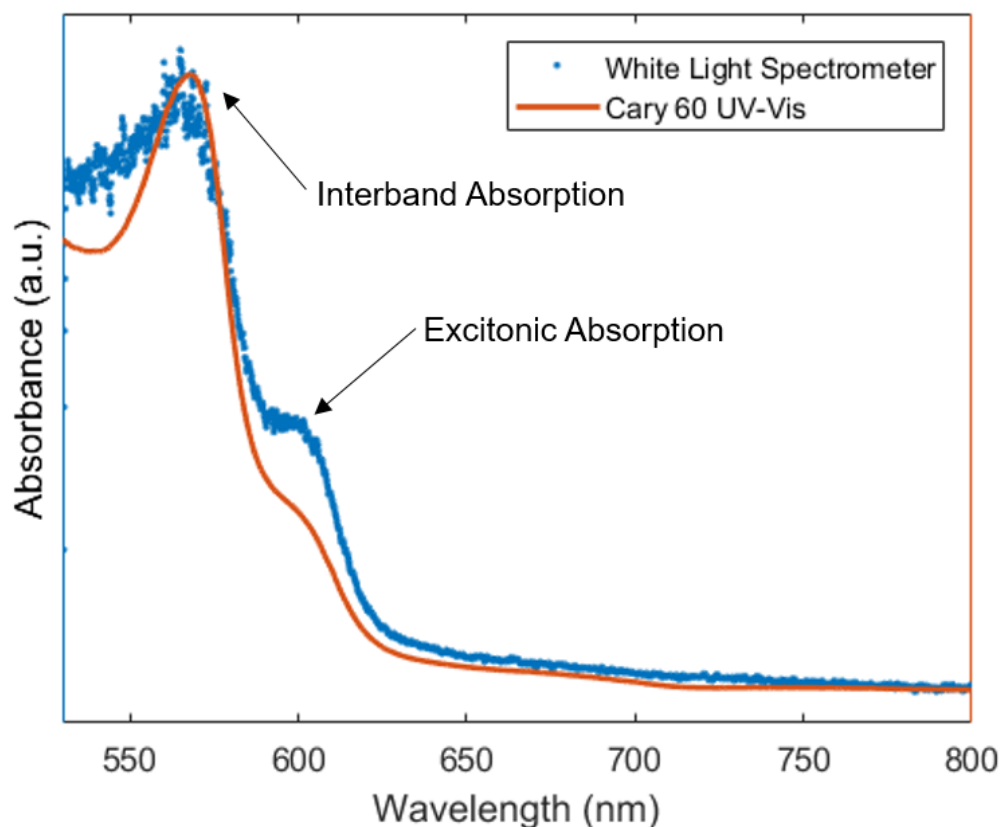


Figure 3.6: Absorbance spectrum of $\text{BA}_2\text{MAPb}_2\text{I}_7$ film using Cary UV-Vis spectrophotometer (red) and Tungsten halogen lamp spectrometer (blue).

3.3.2 Tungsten Lamp Spectrometer

A more portable absorbance measurement device was required in order to complete a temperature dependent absorbance study. Thus, a transportable tungsten halogen lamp (Ocean Optics) was incorporated into the setup in Professor Kimberley Hall's laboratory using optical fibre and was focused through the sample into an Ocean Optics fibre optic usb 4000 spectrometer. Once again, the transmittance was measured as a function of incident wavelength and the absorbance spectrum was obtained via Eq. 3.2. The light source was focused to a spot size radius of $\sim 100 \mu\text{m}$ at the sample. The spectrometer can detect wavelengths from 530 to 800 nm. As there was some concern regarding the validity of the device, the obtained absorbance spectrum at room temperature was compared to that from the Cary 60, and is shown in Figure 3.6. Although the absolute absorbance values differ, as do the relative heights of

the bandgap and excitonic absorption peaks, the important features and their spectral positions are shared, therefore the Tungsten lamp absorbance device was deemed sufficient for continued use.

3.4 Optical Bandgap

The energy gap of the $n = 2$ perovskite sample was determined by creating a Tauc plot out of the absorbance data [142]. A Tauc plot has the quantity $(\alpha h\nu)^{1/r}$ on the y-axis against photon energy, $h\nu$, on the x-axis where α is the absorption coefficient and r is a numerical factor dictated by the nature of the transition. For direct allowed transitions, as in 2D and 3D lead-halide perovskite, $r = 1/2$ [143]. Since the complex index of refraction is unknown for this $n = 2$ perovskite material, the absorption coefficient has been replaced here by the absorbance from Eq. 3.2 which is valid if reflection, scattering and other non-absorption attenuation mechanisms are independent of wavelength. The optical bandgap is then obtained by extrapolating the linear region of the bandgap absorption in the Tauc plot down to the abscissa or x-axis [141] as shown by the orange dashed line in Figure 3.7. Using this method, a energy gap of (2.12 ± 0.05) eV is obtained, which agrees within uncertainty with bandgap calculations in the literature for this material (2.08 eV) [41].

3.5 Phase Transitions

3D lead-iodide perovskite has been shown to undergo two phase transitions when cooling from room temperature down to ultracold temperatures (~ 10 K) [144]. It is generally accepted that there are three phases through which lead-halide perovskites transition in this temperature range, and from high temperature to low are known as the α , β and γ phases [76, 144]. However, there is currently disagreement in the scientific community regarding the transition temperatures, crystal structure, and symmetry properties of these phases [144–147]. There has not been a temperature dependent study of the phase transitions in $\text{BA}_2\text{MAPb}_2\text{I}_7$, however its room temperature structure has been observed and computed, via XRD and DFT respectively, to be orthorhombic with inversion asymmetry and space group Cc2m [76]. It is predicted that multiple layer ($n > 1$) 2D perovskite will exhibit similar phase transitions as their

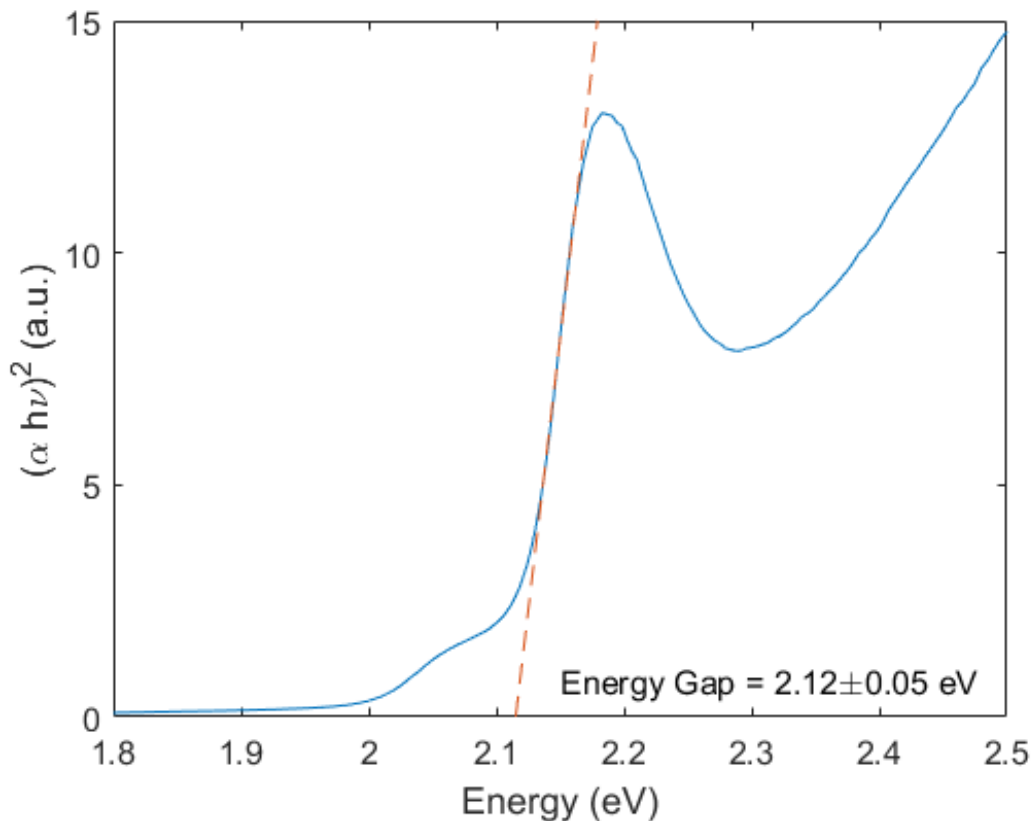


Figure 3.7: Tauc plot is used to determine the optical bandgap of $\text{BA}_2\text{MAPb}_2\text{I}_7$. On the y-axis, α is the absorbance, $h\nu$ is the photon energy and the exponent 2 is used because the relevant transition is direct and allowed. A clear linear region is present on the bandgap absorption rise and the bandgap energy is determined to be the intersection of the extrapolation of the linear rise (orange dashed line) and the x-axis. This energy gap for $\text{BA}_2\text{MAPb}_2\text{I}_7$ was determined to be (2.12 ± 0.05) eV.

more studied 3D counterpart, albeit at different temperatures. Based on the phase transition temperatures of 3D MAPbI_3 [144] and the 2D ($n = 1$) BA_2PbI_4 [145], as well as communication with Costas Stoumpos in the Chemistry Department at Northwestern University, it is believed that the $\alpha \rightarrow \beta$ transition occurs between 255 and 300 K and the $\beta \rightarrow \gamma$ transition occurs between 100 and 150 K.

Chapter 4

Overview of Experiments

4.1 Ultrafast Laser Source

A laser light source was used to study the spin dynamics in 2D perovskite materials. Since the spin dynamics in these semiconductors occur over picosecond time-scales, a laser with subpicosecond pulse duration is necessary to resolve these dynamics. The laser system used here was manufactured by Coherent Inc. The main components of the laser system, namely the Verdi V-18 Pump, Mira-SEED and optical parametric oscillator (OPO), are discussed below.

4.1.1 Verdi V-18 Pump Laser

The Verdi V-18 pump laser is a solid-state, diode pumped laser with Neodymium-doped Yttrium Orthovanadate (Nd:YVO₄) gain medium. The Verdi has an average output power of 15 W and output wavelength of 532 nm. The characteristic wavelength of Nd:YVO₄ is 1064 nm and so the output wavelength is attained through intracavity second harmonic generation (SHG) in a lithium triborate (LBO) nonlinear crystal. The Verdi optically pumps the Mira-SEED.

4.1.2 Mira-SEED Mode-Locking Laser

The Mira is a solid-state laser with titanium-doped sapphire (Ti:Sapphire) gain medium. The Mira is mode-locked via a nonlinear optical process called the Kerr lens effect, for which sufficiently intense light experiences nonlinear refractive indices with respect to the electric field strength. Mode-locking enables the Mira to produce optical pulse of extremely short duration, in this case on the order of 100 fs or 10^{-13} s. It works by inducing a common-phase relationship between all longitudinal modes of the resonant laser cavity. These “phase-locked” or “mode-locked” modes then interfere in the resonant cavity such that a train of very short duration single

pulses emerge. In a Ti:Sapphire gain medium, the Kerr lens effect focuses the pulsed light, which has a Gaussian intensity profile, but does not self-focus lower intensity continuous wave (CW) light. In tandem with a spatially filtering aperture, this focusing effect ensures only pulse light is supported in the laser cavity. The dispersive glass elements and Ti:Sapphire gain medium produce positive group velocity dispersion (GVD) into the system which is compensated by negative GVD prism pair to keep laser modes phased-locked. The Mira output wavelength is centred at 830 nm with an average power of 3.2 W.

4.1.3 Mira Visible Optical Parametric Oscillator

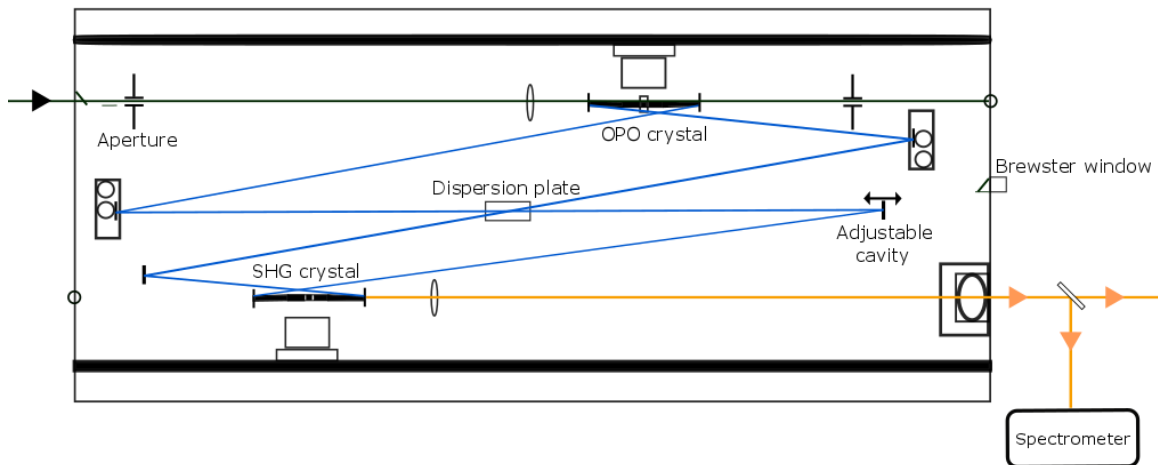


Figure 4.1: Schematic of MIRA Optical Parametric Oscillator in visible configuration

A schematic of the Mira OPO in its visible configuration is provided in Figure 4.1. This configuration consists of a singly signal-resonant potassium titanyl phosphate OPO crystal along with an intracavity SHG module. The SHG module works by temperature tuning the SHG crystal to slightly alter its size in order to create phase matched SHG for visible output generation. The output wavelength and bandwidth is measured in real-time with a spectrometer and the power is monitored with a photodiode. The output wavelengths are tunable from 550 nm to 740 nm with an output power that varies greatly with wavelength but is on the order of 100s of mW.

4.1.4 Laser Spot Size

The spot size of the laser beam incident on the sample was determined by the fractional transmission of the laser through a pinhole of known area less than the laser spot size. The spot size, or radius of the beam, is given by

$$w = a\sqrt{2}[\log(1 - T)]^{-\frac{1}{2}} \quad (4.1)$$

where a is the pinhole radius and T is the ratio of transmitted power to incident power. For this optical setup, this calculation yields a spot size of $\sim 60 \mu\text{m}$.

4.2 Ultrafast Pump-Probe Spectroscopy Techniques

4.2.1 Degenerate Time Resolved Differential Transmission

Ultrafast spectroscopy is the study of light matter interaction dynamics on extremely short time scales using ultrashort pulse lasers such as the system described previously. The type of ultrafast spectroscopy used in this thesis, TRDT is more commonly called pump-probe. In pump-probe spectroscopy, the ultrashort laser pulse is split in two by a beam splitter with one of the pulse pairs being the pump and the other the probe. By placing a movable stage in the pump beam's path, the path length to the sample can differ between the two pulses and as a result one pulse is delayed with respect to the other. When the pump pulse arrives at the sample first, it can excite the carriers in the material, and the effects of this excitation, namely a change in optical absorption, can be detected by the delayed probe pulse as shown in Figure 4.2. By moving the stage position to create longer and longer probe pulse delays, the excitation effects can be monitored over time. In this study the photon energies of the pump and probe pulses are the same and in this case it is known as degenerate pump-probe spectroscopy. The experimental setup is shown in Figure 4.3 with the quarter waveplates (QWPs) in each beam path set to linear. A lock-in amplifier is employed with a reference frequency of the pump pulse via an optical chopper so that only measurements which occur at the pump frequency survive. This ensures any measured change in probe transmission by the Si amplified detector (Thorlabs) is due to the pump pulse.

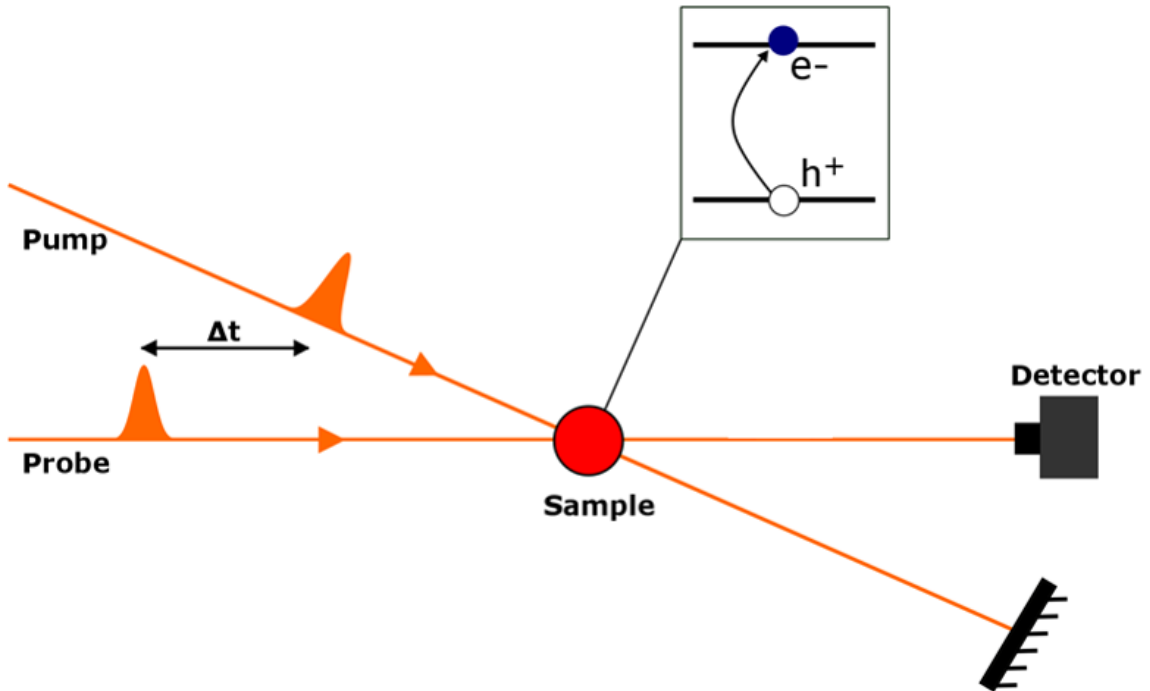


Figure 4.2: Schematic of Pump-Probe Spectroscopy: The pump pulse excites the charge carriers in the sample (inset) and their subsequent relaxation can be probed as a function of time by varying the delay, Δt , between pump and probe pulses.

4.2.2 Circularly Polarized Pump-Probe

In TRDT, the incident light is linearly polarized, meaning it contains equal parts left circular polarized (LCP) and right (RCP) light, and thus does not create a net spin polarization when it excites carriers. In contrast, circularly polarized pump-probe spectroscopy uses circularly polarized light to excite carriers to specific spin states. Circularly polarized light is created by sending linearly polarized light through a quarter waveplate with its fast and slow axis at 45° from the polarization axis of the incident light. This induces a phase shift of $\pi/2$ between the fast and slow components thus creating circularly polarized light. When this is done to both the pump and probe pulses, they are either co-circularly polarized if they share the same direction of circularly polarized light (left or right), or counter-circularly polarized if they do not. By rotating the angle of the QWP by 90° , one can switch the setup from co-circular to counter-circular. The experimental setup for circular pump-probe is shown in Figure 4.3 when the QWPs are rotated appropriately.

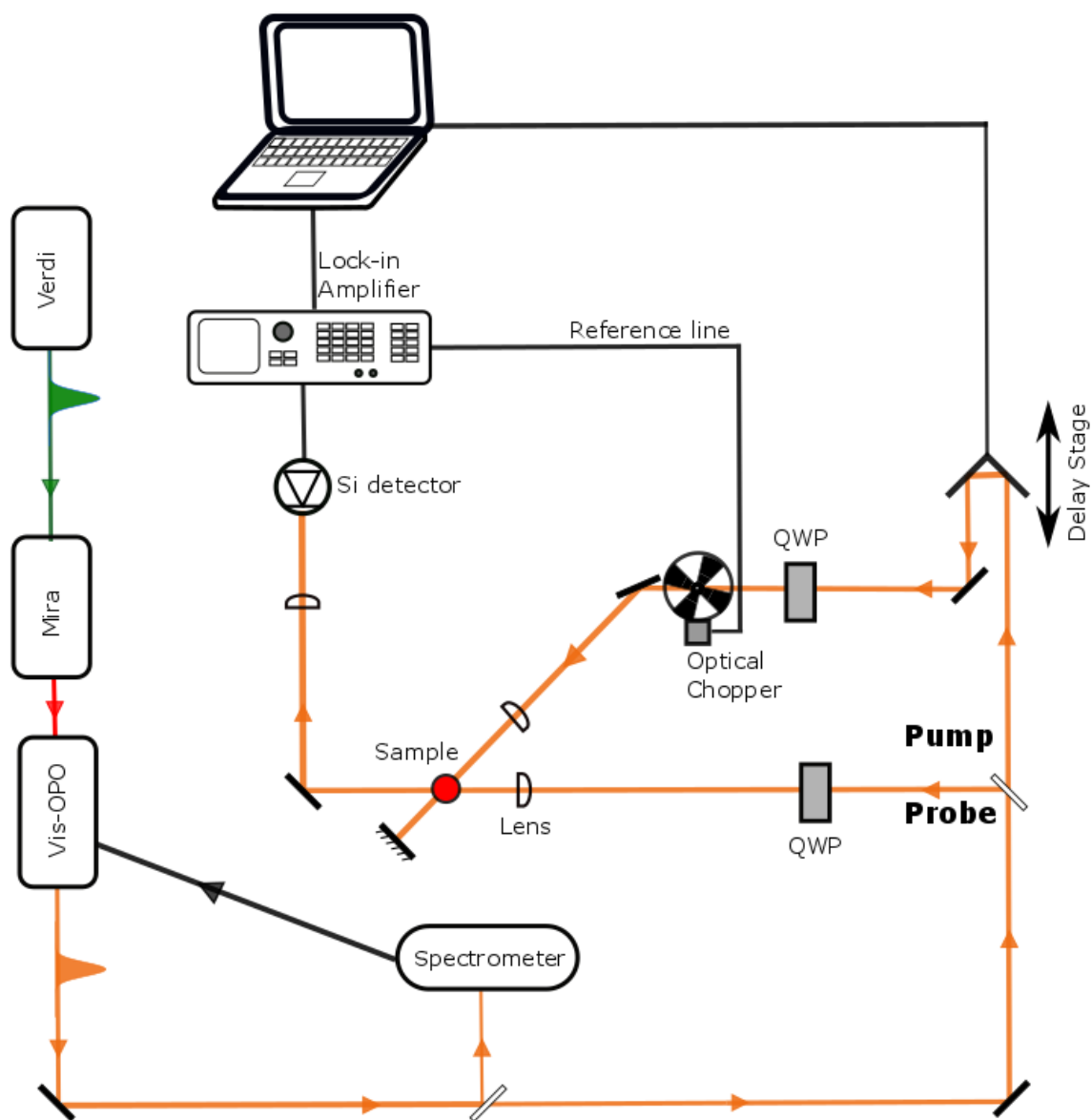


Figure 4.3: Experimental setup of pump-probe spectroscopy. To measure charge carrier recombination dynamics the fast and slow axis of the quarter waveplates (QWPs) are set to linear polarization. To study the spin dynamics of charge carriers the QWPs are rotated to produce circularly polarized light.

4.2.3 Calibration of Quarter Waveplates

The quarter waveplates used in this study to create circularly polarized light were CVI ACWP-400-700-10-4 and CVI ACWP-700-1000-10-4 the former of which is designed for visible light (400-700 nm) and the latter for IR (700-1000 nm). Since exclusively visible light (560-620 nm) was used in this study, there was some concern that the IR QWP would not be calibrated properly to create circularly polarized light. To determine the optimal fast and slow angle for each waveplate to create circular light, and to gauge the level of circular polarization, the setup depicted in Figure 4.4 was used. The linear polarizer was set to allow maximal laser transmission into the power meter in the absence of any QWPs. Each QWP was then placed in the beam path as shown. The polarization out of the Vis-OPO laser is vertical. When vertically polarized light passes through a QWP set to the appropriate fast and slow axis angle, circular light is created. For our purposes we will call this light LCP although the direction of the circularly polarized light was never determined. When LCP light is reflected off the mirror, its polarization reverses to RCP and then is turned to horizontal linear polarization upon passing back through the QWP. Thus, light will be minimally transmitted through the linear polarizer into the power meter when the QWP fast and slow axis is set to circular with respect to the incident linear polarization (45°) and maximally transmitted when the QWP is set to linear (0°). The power transmitted and resulting percent modulation of circular light for each QWP at seven different laser wavelengths is shown in Table 4.1. The modulation is calculated as $1 - (\text{Min Power} / \text{Max Power}) / 2$, where the division by 2 occurs because the light passes through the QWP twice. For the longest wavelength (620 nm), the IR QWP actually outperforms the Vis, however as photon wavelengths move further away from the prescribed range for the IR QWP the percentage modulation of circularly polarized light drops below 95%. This means that the probe beam, in whose path the IR QWP is placed, will be producing slightly elliptical light and not truly circular light. This will result in a lower measurement of the degree of spin polarization for excited charge carriers.

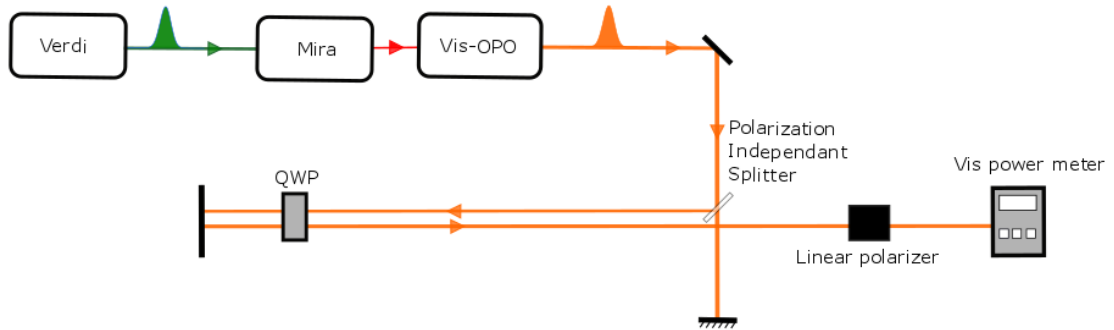


Figure 4.4: Experimental setup for the calibration of QWPs for linearly and circularly polarized pump-probe spectroscopy.

λ (nm)	QWP	Max Power (mW)	Min Power (mW)	% Modulation
560	Vis	13.0	0.17	99.4
	IR	11.2	1.39	93.8
570	Vis	40.7	0.36	99.6
	IR	37.6	4.34	94.2
580	Vis	38.9	0.30	99.6
	IR	36.9	3.62	95.1
590	Vis	38.8	0.31	99.6
	IR	38.2	2.70	96.4
600	Vis	44.1	0.39	99.6
	IR	44.0	2.16	97.6
610	Vis	33.8	0.37	99.4
	IR	34.0	0.80	98.8
620	Vis	35.3	0.42	99.4
	IR	35.5	0.42	99.4

Table 4.1: Degree of circular polarization of light produced by infrared (IR) and visible (Vis) quarter waveplates (QWP)

Chapter 5

Results and Discussion

5.1 Sample Stability

5.1.1 Exposure to Humid Air

2D perovskite materials have been shown to be more resistant to moisture than their 3D counterparts, as outlined in Chapter 1. Indeed, photovoltaic devices made from 2D lead-halide perovskites were able to maintain their power conversion efficiency for months in comparison to a few days for bulk perovskite devices [41]. However, in device architectures the photon absorbing perovskite layer is generally encased in an insulating layer which may help increase the device's moisture resistance. When one of the ($n = 2$) perovskite thin films fabricated in this study was exposed to humid air (characterized by $\sim 30\%$ relative humidity) for approximately one week due to a cryostat leak, parts of the sample visibly changed from the original clear red colour to yellow. In order to gain further insight into the influences of moisture on the 2D perovskite material studied in this work, the absorbance spectrum was obtained after the sample decayed and was compared to the original spectrum taken after fabrication. This is shown in Figure 5.1.

Several notable changes in the absorption spectrum of the perovskite sample occurred as a result of exposure to humidity. The original ($n = 2$) absorbance peak is greatly reduced and the excitonic absorption is no longer visible in the decayed film absorption spectrum. Additionally, two new absorbance peaks are present after the moisture exposure. The lower energy peak occurring around 500 nm is attributed to a partial conversion of the ($n = 2$) original film to the corresponding ($n = 1$) material. The preferential formation of lower number of layers, n , has been observed previously, and shown to provide a means to engineer carrier transport in device films [140]. The assignment of this additional peak to ($n = 1$) material is supported by its location around 500 nm, which is consistent with previous work for this material system which

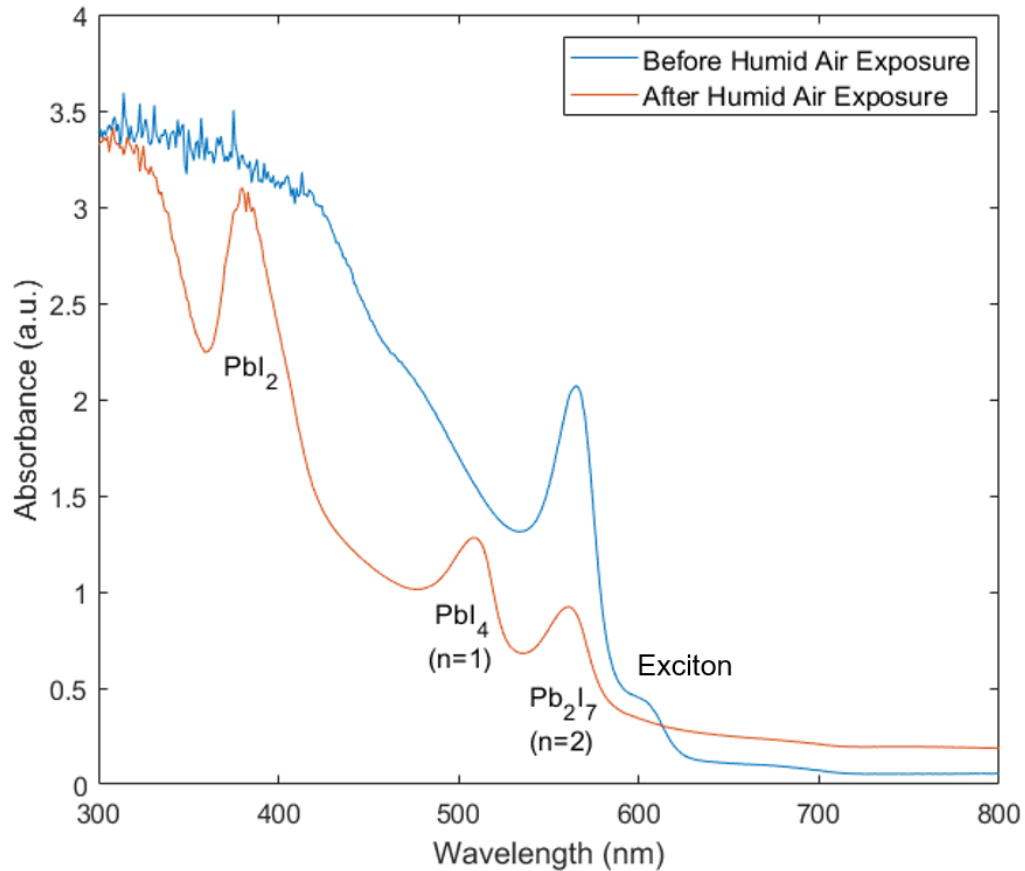


Figure 5.1: Linear absorption spectrum of a $\text{BA}_2\text{MAPb}_2\text{I}_7$ film just after deposition (blue curve) and after exposure to humid air for one week (red curve). The additional peaks at ~ 380 nm and ~ 510 nm are attributed to sample decomposition, leading to excess lead iodide and the conversion of some of the ($n = 2$) film to the energetically more stable ($n = 1$) 2D perovskite species.

place it at 510 nm [41]. The higher energy peak is attributed to lead (II) iodide, PbI_2 . The presence of lead iodide was evident from the yellow colour of the decayed perovskite film. The bandgap absorption peak of PbI_2 is known to occur between 300 nm and 400 nm [148]. The precipitation of PbI_2 out of the film when the lead-iodide perovskite is exposed to moisture in the air also occurs for 3D perovskites. Although 2D perovskite films have been shown to be much more resistant than 3D films, this decay from a week of moisture exposure suggests that encapsulation is necessary for devices based on 2D films, similar to the case of 3D perovskite devices.

5.1.2 Radiatively Induced Degradation

The organic-inorganic perovskites are known to be subject to light-induced changes in their optoelectronic and transport properties. In order to ensure that such changes were not occurring during our optical experiments, and to gain insight into photo-damage effects in the ($n = 2$) perovskite film studied in this work, the influence of laser exposure was tested by measuring changes in the transmission through the film during exposure. The result of this test is shown in Figure 5.2. These experiments were carried out within the pump-probe setup, ensuring that the spot size was identical to that used in the spin dynamics experiments. The wavelength used for these measurements was 570 nm, corresponding to a photon energy of 20 meV above the the bandgap at room temperature. The transmission is observed to increase with laser exposure time for powers exceeding 2 mW. The rate of change of the transmission is observed to increase with increasing power of exposure, with the highest slope for 10 mW incident on the sample. The slope is small but significant for a power as low as 4 mW, which corresponds to a fluence of $0.5 \mu\text{J}/\text{cm}^2$. The increase in transmission with light exposure suggests that the laser is locally bleaching the film. While it is not possible to measure the transmission spectrum on the localized damaged regions due to the small spot size of the focused laser beam, it is likely that the film is decomposing into other compositions, as was seen in the case of moisture exposure, since such a decomposition redistributes the absorption towards higher energies, away from the band edge of the starting film. This redistribution of absorption would be observed as an increase in transmission near the band edge.

More studies are needed to characterize the process of radiative decay in this and similar 2D perovskite materials for future applications in optospintronic applications. Pulsed excitation is likely to be exploited in such applications. For instance, recent demonstrations of carrier spin control via the optical Stark effect [113] involved high pulse fluence exposure, and high repetition rates would be beneficial for high speed spin logical operation employing optical spin control. As a result, a determination of the threshold fluence at which damage occurs as a function of the laser repetition rate and wavelength would be a useful direction for future work. All studies in the remainder of this thesis were completed at laser fluences below $0.35 \mu\text{J}/\text{cm}^2$ (3 mW laser power) to avoid photodamage to the films.

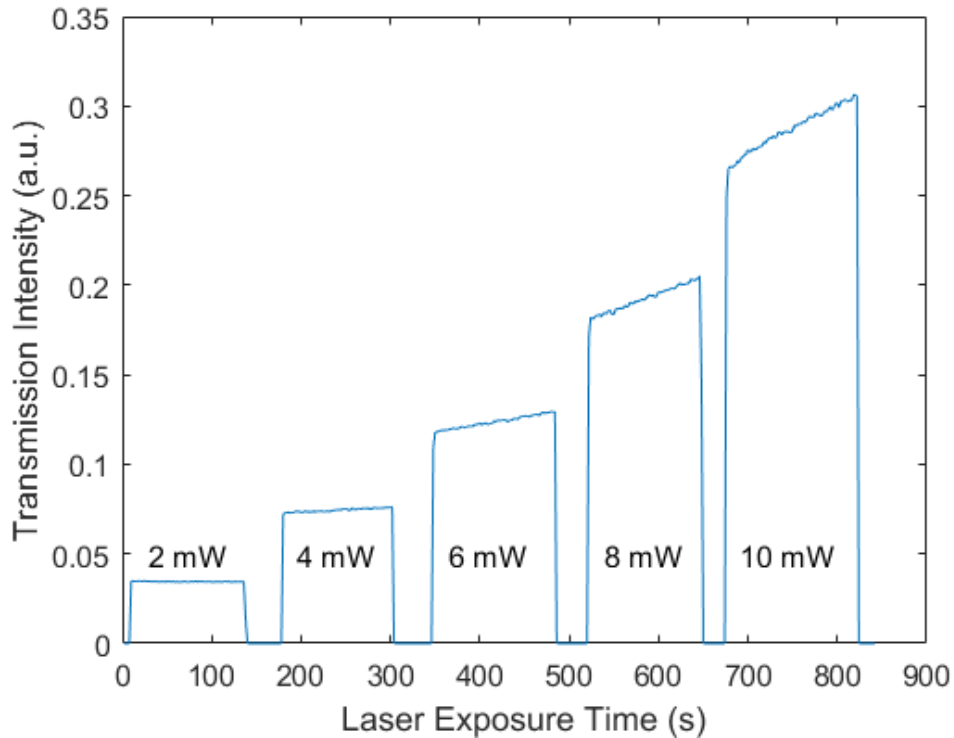


Figure 5.2: Results of measured transmission through the $\text{BA}_2\text{MAPb}_2\text{I}_7$ film while it is exposed to the OPO excitation beam tuned to 570 nm (20 meV above the bandgap) for various average powers. Results show evidence of laser-induced film decomposition, manifested as a reduced band edge absorption with exposure time.

5.2 Temperature Dependence of Absorption

The temperature dependence of the absorbance spectrum is shown in Figure 5.3 (a) and characteristic absorbance plots are shown on the right in Figure 5.3 (b)-(e). The black dashed curves identify the peak wavelength position for the bandgap and exciton absorption as a function of temperature. There is a sharp change in exciton binding energy in both of the regions of temperature in which phase transitions are expected to occur for ($n = 2$) $\text{BA}_2\text{MAPb}_2\text{I}_7$. The evolution of the exciton binding energy, taken as the energy difference between the two peaks, with temperature is more pronounced in Figure 5.4. Based on this plot, the $\alpha \rightarrow \beta$ and $\beta \rightarrow \gamma$ phase transitions in $\text{BA}_2\text{MAPb}_2\text{I}_7$ occur at 280 K and 130 K respectively. An overall trend of increasing exciton binding energy with decreasing temperature from room temperature to 10 K is also observed, and has been witnessed in perovskite materials previously [125, 149,

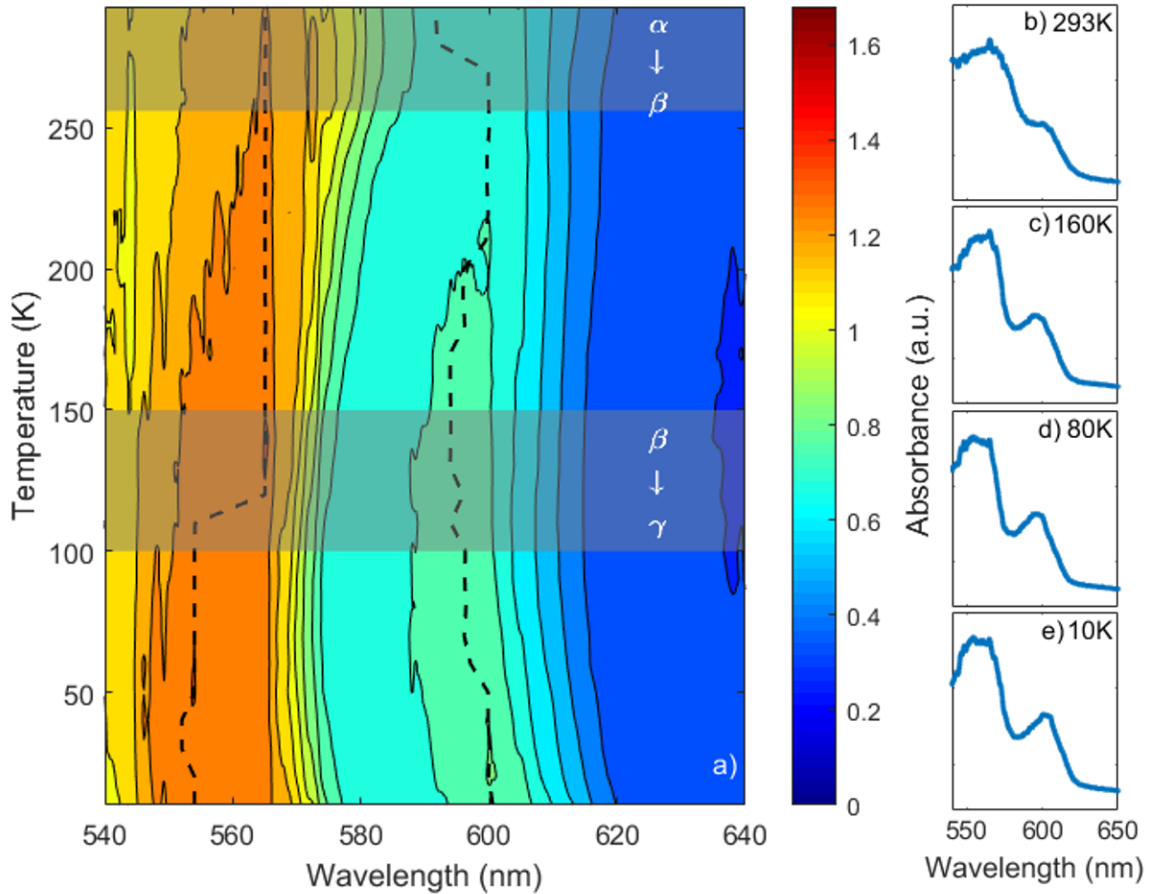


Figure 5.3: (a) Absorbance as a function of sample temperature and photon wavelength. (b)-(e): Individual absorbance spectra at fixed temperatures ((b) 293 K; (c) 160K; (d) 80 K; (e) 10 K).

150]. This may be seen by comparing the absorbance spectrum at room temperature (Figure 5.3 b) and 10 K (Figure 5.3 e). In the former, the exciton absorption peak is primarily contained within the bandgap absorption, expressing itself only as a shoulder on the main bandgap absorption rise. In the latter case, two absorbance peaks are distinctly visible and have separated from an energy splitting of ~ 100 meV at 293 K to ~ 180 meV at 10 K. The range of binding energies in Figure 5.4 are in line with the large exciton binding energies found previously in 2D perovskite materials [61, 76].

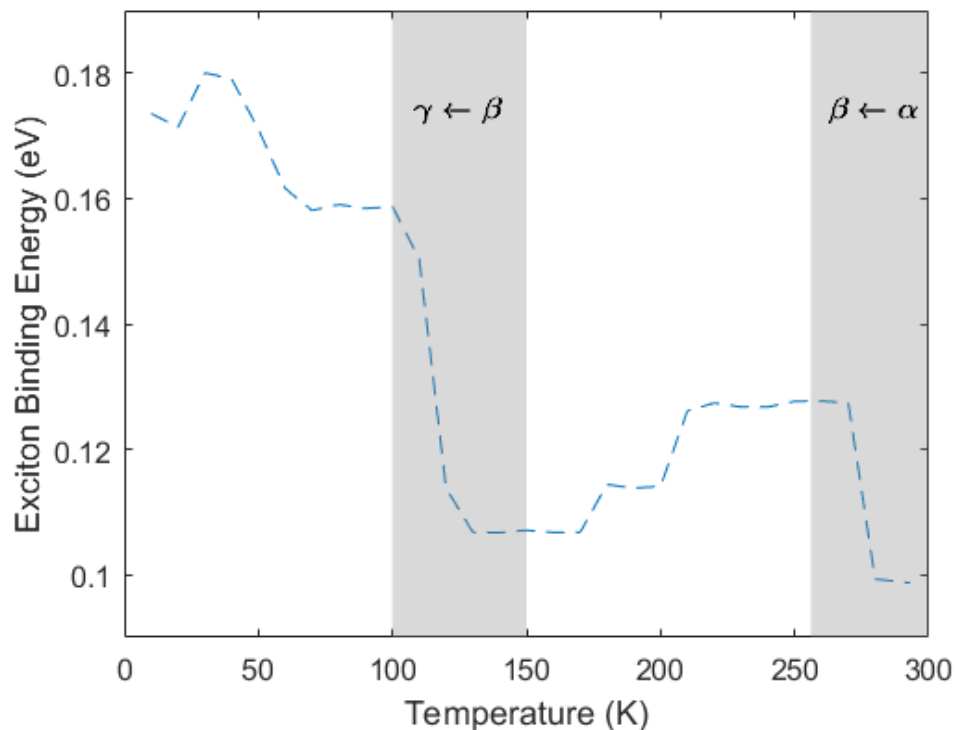


Figure 5.4: Temperature-dependent exciton binding energy in the $\text{BA}_2\text{MAPb}_2\text{I}_7$ film extracted from the linear absorption results.

5.3 Charge Carrier Dynamics in $\text{BA}_2\text{MAPb}_2\text{I}_7$

In preparation for measurements of the spin-resolved carrier dynamics, a measurement of the carrier dynamics for equal spin populations was made by performing pump-probe differential transmission experiments for linearly-polarized optical excitation at room temperature. Owing to the selection rules, linearly-polarized light results in an equal population of spin up and spin down carriers. Carrier dynamics have been studied extensively in traditional inorganic semiconductors [117]. Following excitation by a short laser pulse, the initial carrier distribution has an energy profile that reflects the laser excitation spectrum. The most rapid scattering process (typically carrier-carrier scattering) then transforms this *non-thermal* population into a thermal distribution, for which the energy profile is described by the Fermi distribution function. The temperature of this initial thermal distribution is determined by the excitation energy of the laser since this energy dictates the initial kinetic energy of the carriers. For above bandgap excitation, the carriers therefore initially form a *hot*

distribution. Phonon emission and absorption processes ultimately enable this hot carrier distribution to exchange energy with the lattice and cool to the lattice temperature. Once this occurs, the thermalization process is complete. The thermalized carrier distribution then recombines, returning the semiconductor to equilibrium.

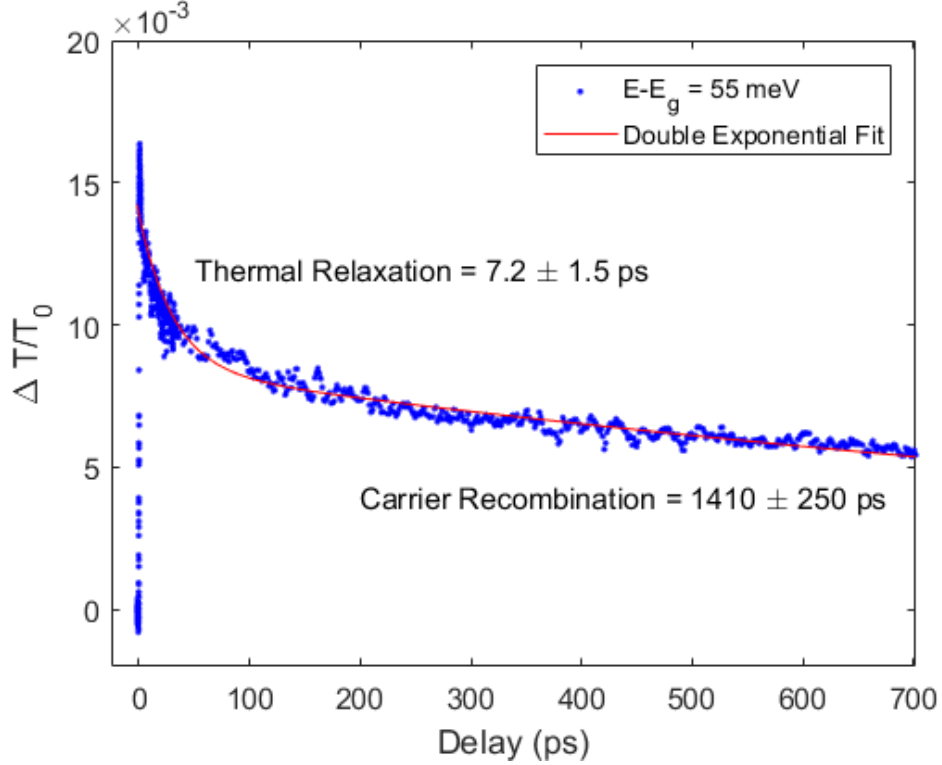


Figure 5.5: Results of pump-probe differential transmission experiments with linearly-polarized light, for which equal spin up and spin down carrier populations are excited. Blue symbols: experimental data; red curve: exponential fit. Fit values indicate a carrier thermalization time of (7.2 ± 1.5) ps and a recombination time of (1410 ± 250) ps, with uncertainties determined by averaging measurements over the full range of excitation energies.

The pump-probe response was measured in $\text{BA}_2\text{MAPb}_2\text{I}_7$ for a range of laser excitation energies in the vicinity of the band edge (from approximately 90meV below bandgap to 100meV above). The carrier relaxation in each case was fit to a double exponential decay, as described in Eq. 2.10, to account for thermalization and recombination. An example fit for 55meV excess energy is shown in Figure 5.5, which is representative of the results obtained at all energies. The pump-probe results for a small range of interpulse delay ($\Delta t < 20$ ps) are shown for a range of excitation

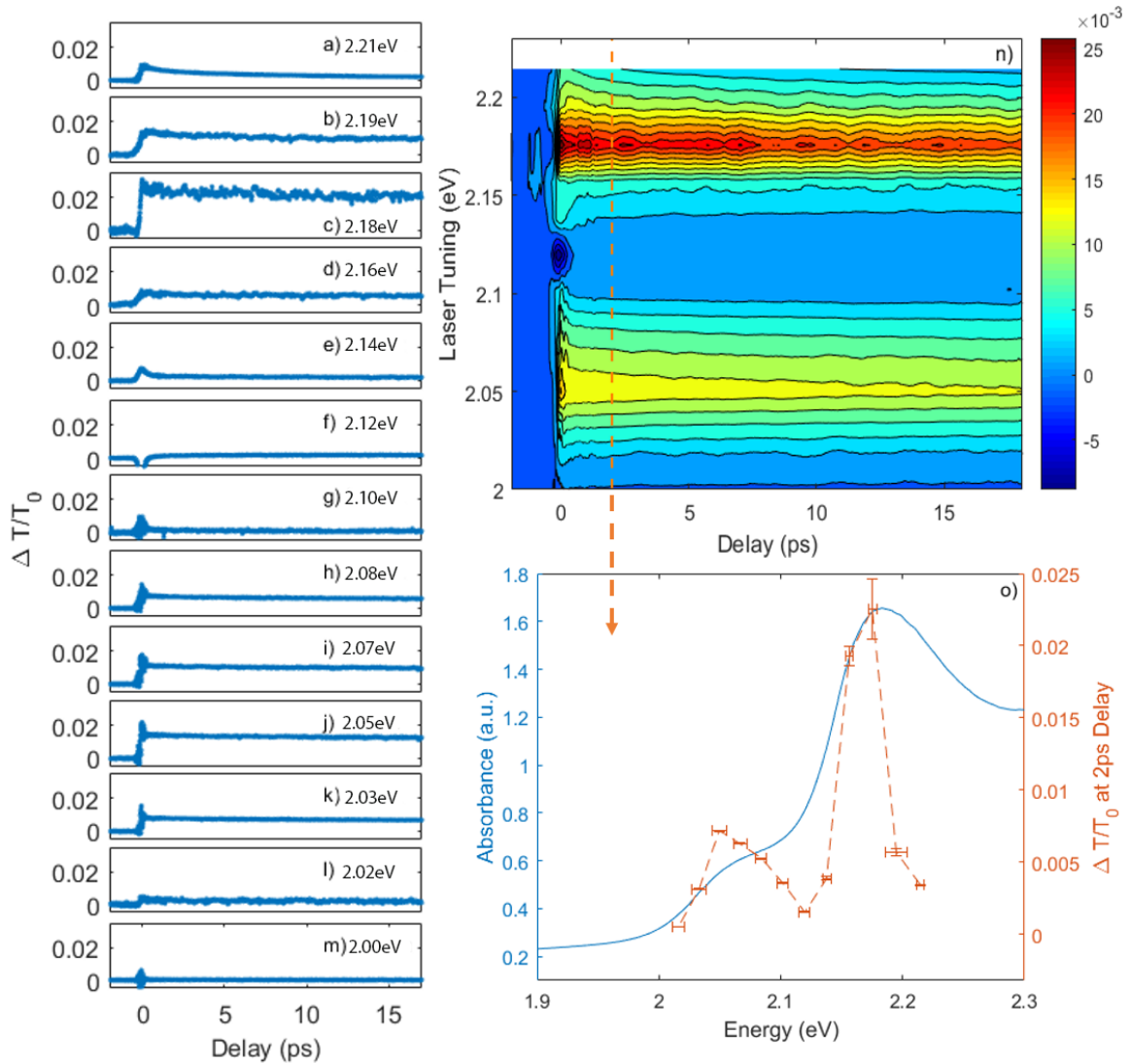


Figure 5.6: (a)-(m) Results of pump-probe experiments using linearly-polarized excitation for a range of laser excitation energies relative to the bandgap. (n) The magnitude of the pump-probe signal is shown as a function of laser excitation energy and delay on a contour plot. (o) The magnitude of the pump-probe signal at 2 ps delay is plotted together with the linear absorption spectrum, indicating pump-probe responses from both excitons and interband transitions above the bandgap.

energies in Figure 5.6. The snapshot at 2 ps delay (Figure 5.6 (o)) provides a measure of the absorption spectrum of the sample. The excitonic absorption peak is observed, and the excited population is minimal for laser excitation at or below the bandgap ($E_g \sim 2.12$ eV) and then rapidly rises as the excitation photon energy is increased. The band edge response observed in these results contains a sharper onset than in the linear absorption spectrum. The absorption edge is typically more clearly observed in nonlinear pump-probe spectroscopy than in linear absorption because the pump-probe signal reflects a reduction in absorption due to state filling, while the linear absorption response is also influenced by scattering losses, which show up as a tail in the bandgap region and at lower energies. The exciton binding energy extracted from Figure 5.6 (o) is consistent with that found via absorbance measurements in section 5.2 (100 meV at room temperature).

The thermal relaxation time was determined to be $\tau_{th} = (7.2 \pm 1.5)$ ps and the carrier recombination lifetime was determined to be $\tau = (1410 \pm 250)$ ps. The uncertainties in these values were obtained from the standard error of the mean for measurements at the 13 different energies probed. The thermal relaxation lifetime resides in the expected temporal regime for direct bandgap semiconductors [117, 151] and the recombination time is comparable to lifetimes observed in other 2D lead-halide perovskite materials [74].

5.4 Spin Dynamics in $\text{BA}_2\text{MAPb}_2\text{I}_7$ at Room Temperature

5.4.1 Observed Trends in Spin Dynamics

The results of pump-probe differential transmission experiments using circularly-polarized pump and probe laser pulses are shown in Figure 5.7 (a). During the first ~ 15 picoseconds, the pump-probe signal for co-circular polarization is larger than that for counter-circular polarization. For the co-circular configuration, the probe pulse is measuring the state filling response associated with the same spin-polarization as that injected by the pump pulse. In this case, the dynamics of the majority spin population are detected. For counter-circular polarization, the dynamics of the minority spin are measured. These two populations equalize as carriers undergo spin relaxation. For delays longer than about 20 ps, the two signals are equal, indicating

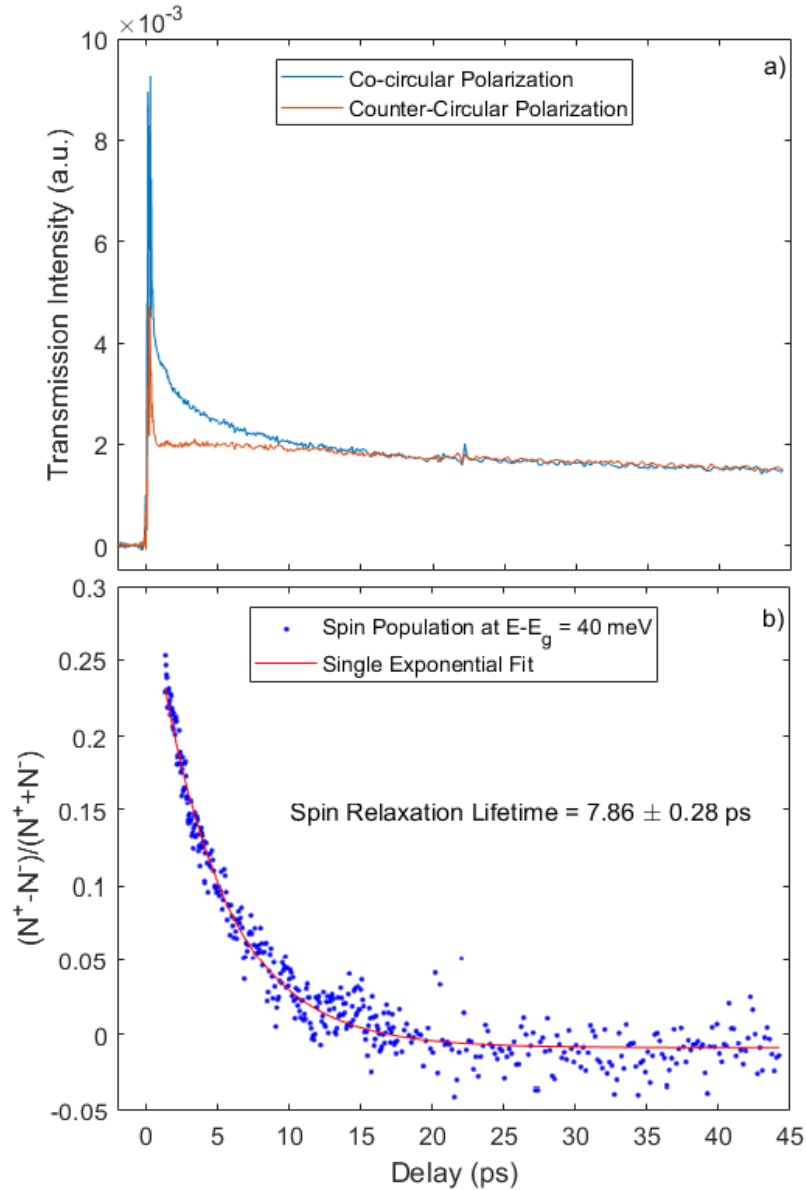


Figure 5.7: (a) Results of pump-probe experiments with circularly-polarized pump and probe pulses for a laser tuning of 2.16 eV. Blue curve: Results for the same circular polarization state in pump and probe beams; Red curve: results for opposite circular polarization states. (b) Degree of circular polarization of the pump-probe signal, reflecting the degree of spin polarization of the electrons and holes in the sample, versus interpulse delay time. Blue symbols: experimental data; red curve; exponential fit, yielding a spin relaxation time of (7.86 ± 0.28) ps.

that the spin polarization has fully decayed.

The spin relaxation time may be determined from the measured pump-probe results in Figure 5.7 (a) by evaluating the degree of spin polarization, which is obtained

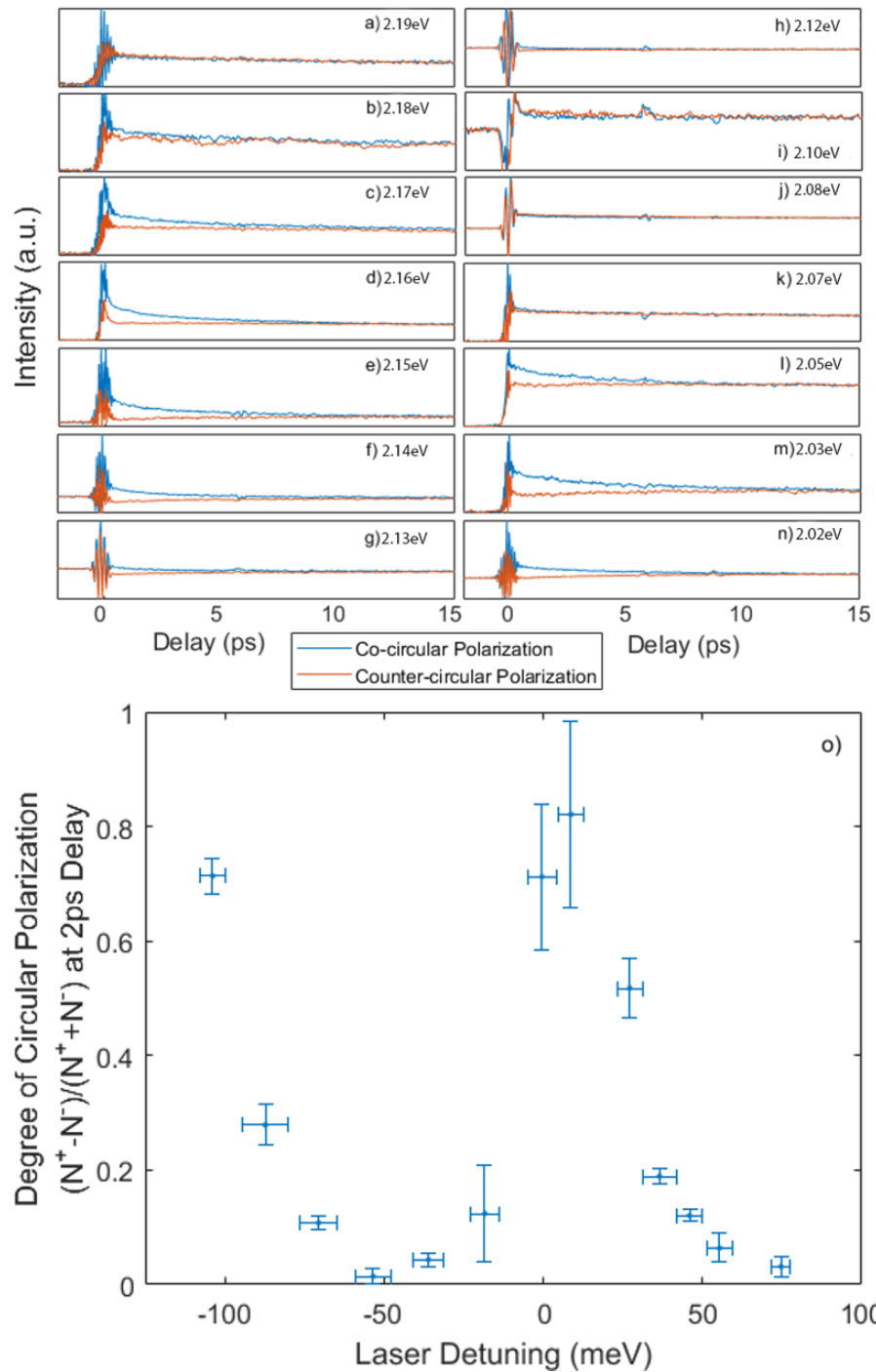


Figure 5.8: (a)-(n) Results of pump-probe experiments with circularly-polarized pump and probe pulses for a range of laser tunings. Blue curves: co-circular polarizations in the pump and probe pulses; red curves: counter-circular polarizations. The laser excitation energy in each case is indicated in the inset. (o) Degree of circular polarization at 2 ps delay as a function of laser detuning.

by taking the difference between the two curves and dividing by the sum. The resulting data are shown in Figure 5.7 (b). The difference is shown only for delays beyond 0.5 picoseconds to avoid the strong zero delay feature in the pump-probe response. The zero delay feature contains a spurious signal often referred to as a coherent artifact that results from a four-wave mixing response in the sample, which can have the same or opposite sign as the carrier state filling signal, but does not contain useful information about the spin dynamics. A fit of the degree of spin polarization as a function of delay provides the spin relaxation time. The fit in Figure 5.7 (b) indicates a spin lifetime of approximately 8 ps.

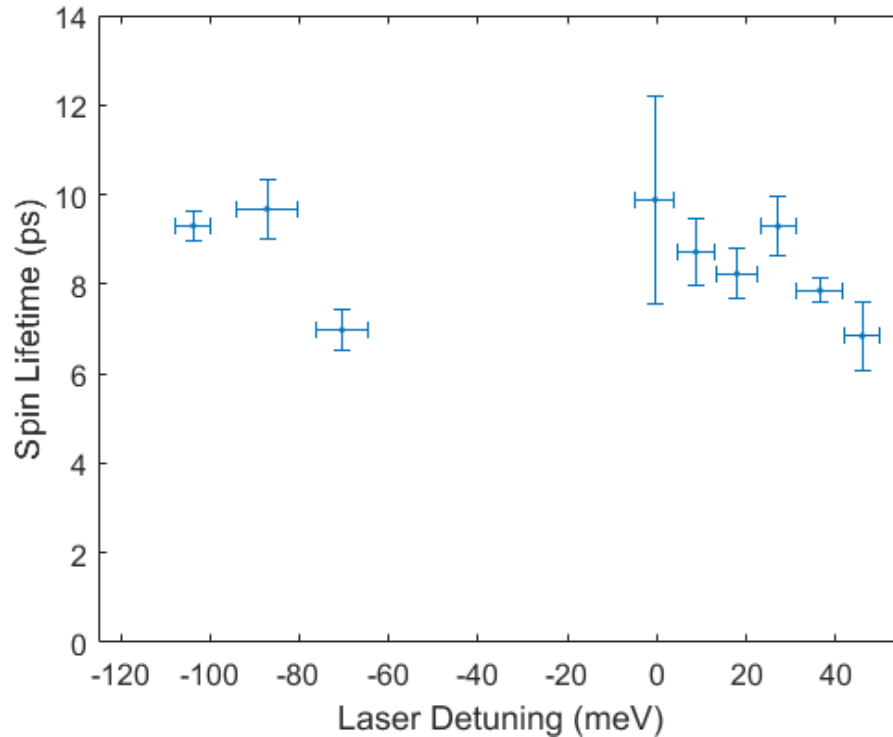


Figure 5.9: Carrier spin relaxation time extracted from the pump-probe results as a function of the laser detuning. The lifetime decreases with increasing energy above the bandgap for free electrons and holes. The exciton spin relaxation time is similar to the band edge value for free carriers.

The raw pump-probe data for a range of laser tunings is shown in Figure 5.8 (a)-(n). It is apparent from these data that the degree of spin polarization, reflected by the separation between the co-circular and counter-circular data curves, varies with the laser tuning. This variation can be seen more clearly in Figure 5.8 (o), which shows

the degree of spin polarization evaluated 2 ps after the pump pulse. The degree of spin polarization is largest at the bandgap of the semiconductor and at the excitonic resonance energy. The spin lifetime extracted from the fit to the spin decay curves at each energy is shown in Figure 5.9. For excitation above the bandgap (i.e. for positive laser detuning) the spin lifetime decreases for increasing laser excitation energy. The spin lifetime for laser excitation on the high energy side of the exciton resonance is similar to the band edge value for free carriers. The absence of lifetime measurements below bandgap in Figure 5.9 is a result of the degree of spin polarization being too low to extract spin lifetimes. This can be seen in the raw data in Figure 5.8 (h)-(k). The spin lifetime was also measured as a function of the laser excitation fluence. The results of these measurements for two different laser tunings above the bandgap are shown in Figure 5.10. The spin lifetime was observed to increase with increasing excitation fluence for both values of the laser tuning.

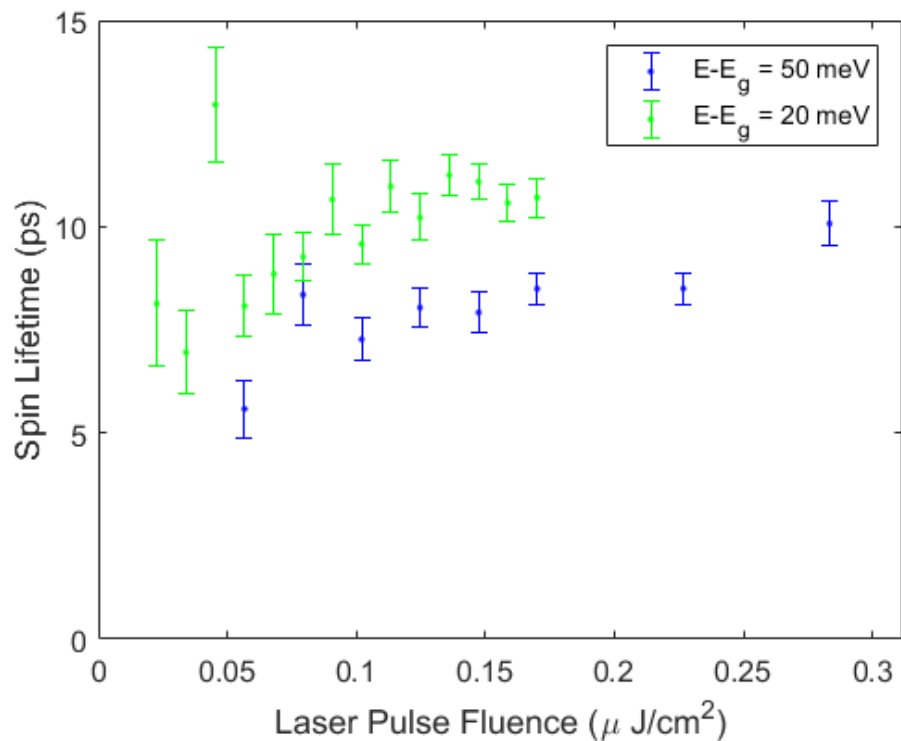


Figure 5.10: Carrier spin relaxation time extracted from the pump-probe results as a function of laser pulse fluence. Results indicate an increasing spin lifetime with increasing fluence.

5.4.2 Interpretation of the Measured Spin Dynamics

The results in Figure 5.8 indicate a high degree of spin polarization of approximately 80% in the vicinity of the band edge. This observation of high initial spin polarization is consistent with the optical selection rules for the lowest energy valence to conduction band transition (Figure 2.3) which predicts 100% spin-polarized carriers for excitation at the bandgap. For comparison, 90% spin polarization was observed by Giovanni *et.al.* in 3D perovskites [108], which exhibit identical selection rules [80].

The effective masses of carriers in the conduction band (valence band) in the $\text{BA}_2\text{MAPb}_2\text{I}_7$ material studied here has been estimated as $m_e=0.08 m$ ($m_h=0.14 m$), where m is the vacuum rest mass of the electron [76]. The heavier mass of the holes would lead to a smaller contribution of the hole occupation to the bleaching signal due to the larger density of states in the valence band, [117] similar to the situation for III-V materials [124]. The majority of the bleaching signal is therefore expected to be from the electrons. Nevertheless, since a single exponential decay is observed, the relaxation times for the two carrier species are assumed to be similar.

The carrier spin relaxation time of ~ 10 ps at the band edge in Figure 5.9 is much faster than in GaAs quantum wells, for which a lifetime of 100 ps was observed at room temperature [152]. This is consistent with the DP mechanism and the larger spin splittings calculated for related 2D perovskites [112]. The degree of spin polarization at 2 ps delay decreases when the excitation laser is tuned above the bandgap (Figure 5.8), reflecting the shorter spin lifetime observed with increasing excess energy (Figure 5.9). These observations are also expected for the DP mechanism. Since the carrier thermalization time is comparable to the spin relaxation time, the carrier distribution will not have a chance to fully equilibrate with the lattice, and so the average kinetic energy of the carriers will be higher for higher energy laser excitation (i.e. the carriers remain hot during spin relaxation, with a temperature determined by the excess energy of the exciting photons above the bandgap). A higher average carrier kinetic energy will lead to the occupation of states at larger \mathbf{k} values, accessing regions of \mathbf{k} -space where the magnitude of the effective magnetic field is larger, leading to more rapid spin relaxation. The spin relaxation time at the exciton resonance is similar to the band edge value (Figure 5.9), as expected since the exciton wavefunction is composed of a superposition of small-wavevector components near

the band extrema for electrons and holes.

The above conclusion that DP dominates spin relaxation for carriers in the 2D perovskite structure studied here holds regardless of the dominant scattering process that limits the DP spin relaxation rate. In the general case, carrier-phonon, carrier-carrier, and carrier-defect scattering may contribute to the carrier dynamics within the semiconductor. Evidence for significant phonon scattering contributions have been seen in 3D perovskite [153–155], and as a result phonon scattering is likely contributing in our experiments on 2D butylammonium methylammonium lead iodide. One can assess the role of carrier-carrier scattering by performing measurements at a fixed temperature as a function of laser excitation fluence, shown in Figure 5.10. The observation of an increase in the carrier spin lifetime as a function of fluence indicates that carrier-carrier scattering is contributing significantly to limiting the spin lifetime in our sample. The increase in spin lifetime with increasing power is consistent with motional narrowing, for which the DP relaxation rate is reduced with rapid scattering because the carrier spins are unable to precess significantly before the direction of the effective magnetic field changes. This trend is opposite to that expected for EY relaxation, in which more scattering increases the spin relaxation rate. Carrier-carrier scattering has also been found to contribute to motional narrowing in GaAs quantum wells [156]. All of the observed spin dynamics thus point to the DP mechanism as the dominant relaxation mechanism in the 2D perovskite system studied here at room temperature.

5.5 Spin Dynamics in $\text{BA}_2\text{MAPb}_2\text{I}_7$ at Low Temperature

5.5.1 Measured Temperature Dependence of Spin Dynamics

In order to gain further insight into the spin relaxation kinetics, pump-probe experiments were performed on the $\text{BA}_2\text{MAPb}_2\text{I}_7$ sample over a range of temperatures between 10 K and 300 K. For these experiments, the laser excitation energy was chosen to follow changes in the bandgap with temperature using the corresponding linear absorption spectrum at each temperature. The results of spin relaxation measurements at 40 K are shown in Figure 5.11. The most notable difference between these results and the room temperature measurements in Figure 5.7 is that the degree of

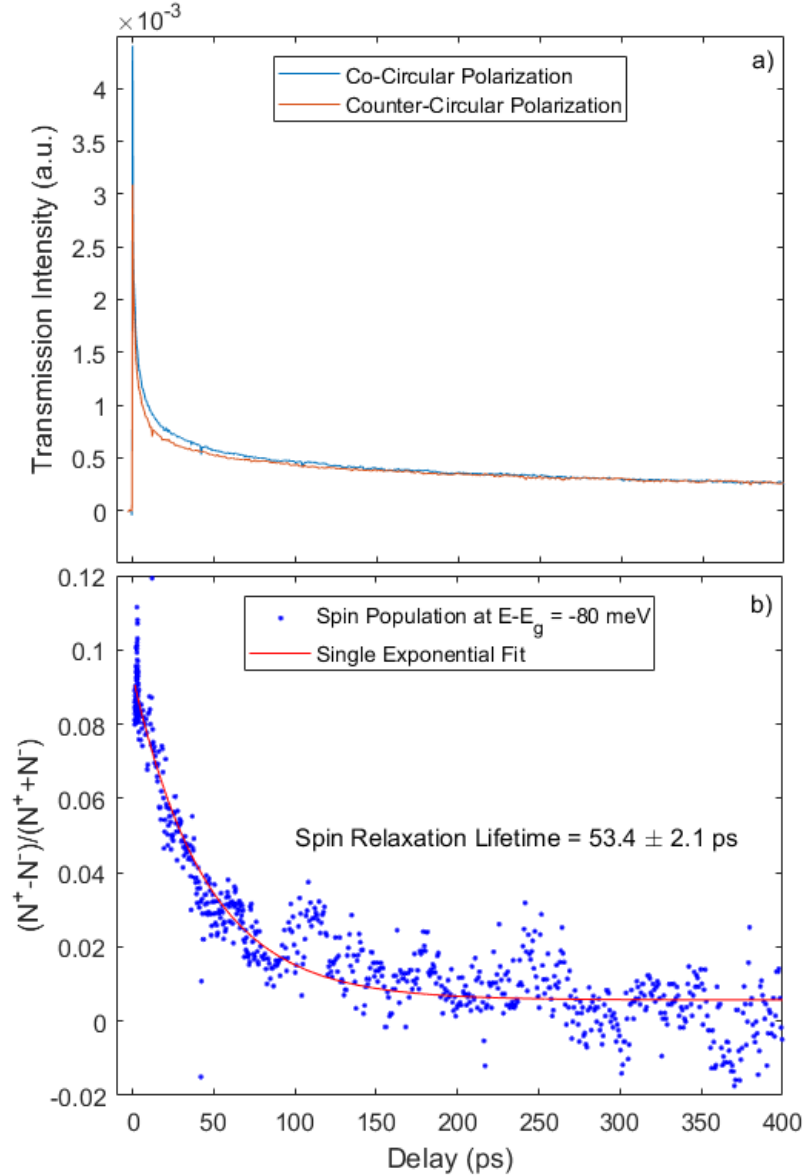


Figure 5.11: (a) Results of pump-probe experiments with circularly-polarized pump and probe pulses with the sample held at a temperature of 40 K. Blue curve: co-circular polarization; Red curve: counter-circular polarization. The results indicate a much smaller degree of circular polarization after the first picosecond than in the room temperature results, but the polarization persists to much larger interpulse delays. (b) Degree of circular polarization extracted from the results in (a). Blue symbols: experimental data; Red curve: single exponential fit, indicating a spin lifetime of (53.4 ± 2.1) ps.

spin polarization is reduced for delay values beyond the region of pulse overlap. This can be seen in Figure 5.12, which shows the degree of circular polarization at 2 ps

delay as a function of temperature. The reduction in spin polarization as temperature is reduced coincides with the $\beta \rightarrow \gamma$ phase transition identified in Sec. 5.2. In addition to the diminished degree of spin polarization, the time scale for spin relaxation is observed to be much longer at low temperatures. The measured dependence of the spin lifetime on temperature is shown in Figure 5.13. For temperatures above the $\beta \rightarrow \gamma$ phase transition, the spin lifetime is observed to increase slowly with decreasing temperature. For an excess energy of 20 meV, the spin lifetime increases by a factor of approximately 2 as the temperature is reduced from 300 K to 170 K. In contrast, for temperatures below the $\beta \rightarrow \gamma$ phase transition, the spin lifetimes are much longer and exhibit a rapid increase with decreasing temperature.

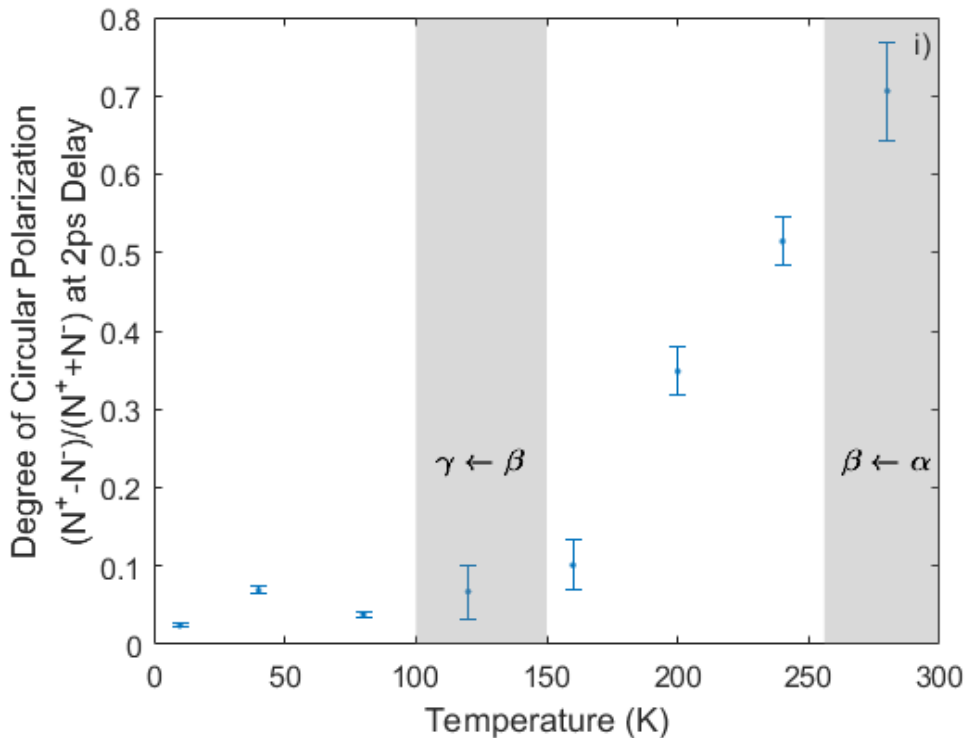


Figure 5.12: Temperature dependence of the degree of circular polarization extracted from the pump-probe results at a delay of 2 ps after the pump pulse. The results indicate a strong reduction below the β to γ phase transition.

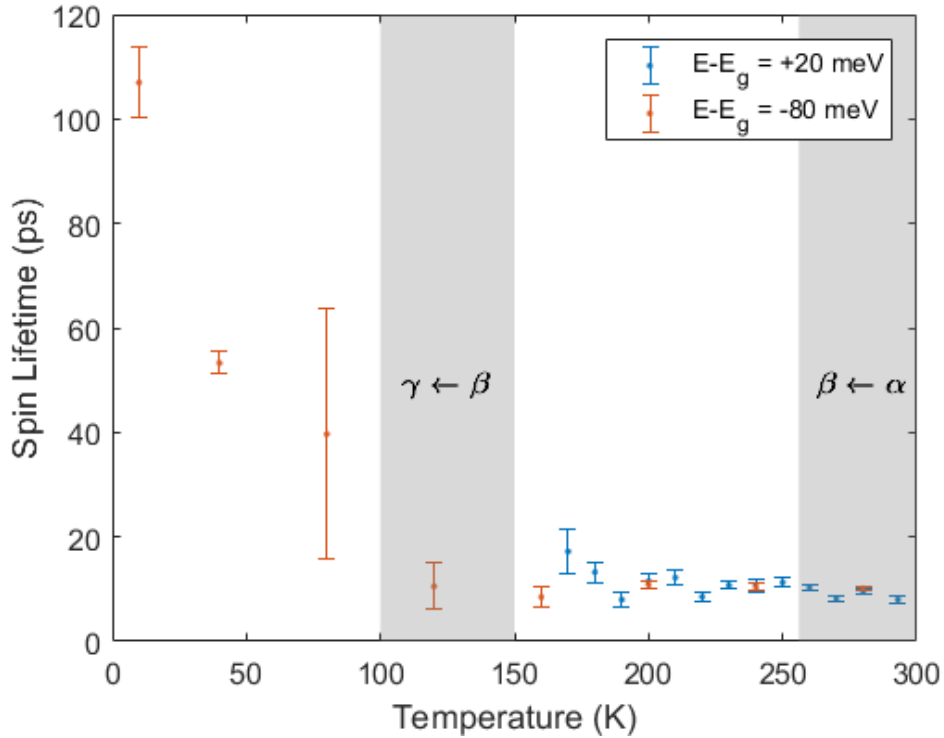


Figure 5.13: Spin relaxation time extracted from the pump-probe results as a function of sample temperature. Results indicate a weak increase in temperature within the α and β phases. For temperatures below the β to γ phase transition, much longer spin lifetimes are observed.

5.5.2 Discussion of the Temperature Dependence

Variations in the spin dynamics as the temperature is reduced are expected to arise from a number of sources: (i) the perovskite sample undergoes structural phase changes with temperature, as discussed in Sec. 5.2; (ii) the rate of scattering with phonons is reduced at lower temperature; thus for a given power the total scattering rate will be reduced; and (iii) The thermalized carrier distribution will become colder as the temperature drops, so that carriers will occupy a narrower range of k-states near the band edge. As no similar phase changes occur in inorganic semiconductors, the phase changes complicate the interpretation of the temperature dependent spin dynamics in perovskites considerably. In particular, the size of the spin splitting will change in different phases due to differing degrees of inversion asymmetry [132]. Calculations have also shown that the magnitude of the spin splitting can change continuously within a given phase due to the temperature dependence of the order

parameter tied to the associated ferroelectric phase transition [112]. As discussed above, the magnitude of the spin splitting in a given phase (and a given material) will depend on both the inorganic and organic constituent components [76, 132].

The observation of a much smaller degree of circular polarization at 2 ps delay within the γ phase suggests the existence of distinct relaxation rates for electrons and holes, with one being below the time resolution of the experiment (i.e. in the subpicosecond range). Due to the larger effective mass of the holes [76], the contribution to the total bleaching signal from the holes is much smaller than that for the electrons. [117] Given the small fraction of the bleaching signal that remains spin polarized after 2 ps, the subpicosecond spin relaxation rate is assigned to the electrons. The longer spin lifetimes values of 40 to 100 ps in the γ phase in Figure 5.13 are therefore attributed to holes. While no calculations of the spin splittings are available in our material system, a much smaller spin splitting has been predicted for the valence band in comparison to the conduction band in the β phase of the 2D perovskite Bz_2PbCl_2 [112]. Our observation of a 50 fold difference in the spin lifetimes of electrons and holes suggests that the spin splitting is much larger in the conduction band than in the valence band in our 2D system as well. These findings point to the need for electronic structure calculations including the spin-orbit interaction in a wide range of 2D perovskite materials. We note that a subpicosecond electron spin relaxation time has also been observed in III-V systems possessing large spin splittings (GaSb/AlSb quantum wells [157] and InAs/GaSb superlattices [158]. In the latter material, the calculated spin splitting exceeds 40 meV [159]). Given the large spin splittings calculated for the 2D perovskite, a subpicosecond spin lifetime for electrons is reasonable.

Chapter 6

Conclusion

The large, tunable spin-orbit coupling, Rashba splitting, and spin dependent optical selection rules make lead-halide perovskites promising materials for spintronic applications. Spin relaxation lifetimes have recently been measured in 3D lead-halide perovskites by Giovanni *et.al.* and Odenthal *et.al.* resulting in vastly different lifetimes of 7 ps and 1ns respectively, and dispute over the dominant relaxation mechanism [57, 108]. This thesis represents the first instance of spin lifetime measurements in the more moisture resistant 2D class of lead-halide perovskites.

Spin relaxation was studied in $\text{BA}_2\text{MAPb}_2\text{I}_7$ using circularly polarized pump-probe spectroscopy and resulted in a lifetime of ~ 10 ps for above bandgap pumping at room temperature. Spin lifetime and degree of spin polarization decreased with increased excess energy above bandgap. Spin lifetime increased with increased laser fluence. These trends point to D'yakonov-Perel' as the dominant spin relaxation mechanism in $\text{BA}_2\text{MAPb}_2\text{I}_7$. The results also suggest that carrier-carrier momentum scattering contributes significantly to limiting the spin lifetime in the sample. At low temperature, the spin relaxation lifetime increased upwards of 20-fold, while the degree of spin polarization was found to decrease. This indicates the presence of distinct relaxation rates for electrons and holes, with holes having lifetimes an estimated 50 times longer than electrons, likely due to significant spin splitting in the conduction band at low temperature. A comprehensive study of the temperature dependence of spin lifetime and degree of polarization is necessary to better understand the relaxation mechanisms at play. In addition to further experimental study, a more complete set of calculations of the electronic band structure in 2D perovskites is needed to assess their capacity for spintronic applications.

Odenthal *et.al.* attributed the disagreement in spin lifetime measurement with Giovanni *et.al.* to deviations in film fabrication process and morphology [57]. Thus, a study concerning the effects on spin lifetime of film parameters including precursor

crystal purity, solvent, substrate, spin-rate and temperature of solution and substrate would be a valuable undertaking. An exploration of film fabrication techniques and parameters is necessary not only to gauge their consequences on spin dynamics but also their impact on sample stability. This study found significant sample degradation due from exposure to humid air and high laser fluence. These stability concerns must be addressed for 2D perovskites to remain a viable candidate for use in a SFET.

This thesis only considered the 2D halide perovskite material $\text{BA}_2\text{MAPb}_2\text{I}_7$ and thus there is need for a more exhaustive study of spin properties in a wide range of 2D perovskites. The dependence of spin lifetime on quantum well width and barrier width can be probed by varying the 2D perovskite layer number, n , and type of organic spacer molecule respectively. Furthermore, to deal with the issue of toxicity of lead, 2D materials made with other, nontoxic group four elements including tin and germanium should be explored for potential use in spintronics.

The surface has only just been scratched in the study of spin dynamics in 2D halide perovskites. A material which combines stability, long spin lifetime and ability for spin manipulation would have enormous ramifications for data transfer, storage and operation in solid-state devices. The family of 2D perovskites are a strong candidate to contain such a material but more exploration is needed before the realization of a perovskite-based spintronic device can occur.

Bibliography

- [1] Martin A Green, Yoshihiro Hishikawa, Wilhelm Warta, Ewan D Dunlop, Dean H Levi, Jochen Hohl-Ebinger, and Anita WH Ho-Baillie. Solar cell efficiency tables (version 50). *Progress in Photovoltaics: Research and Applications*, 25(7):668–676, 2017.
- [2] Martin A Green. Silicon solar cells: evolution, high-efficiency design and efficiency enhancements. *Semiconductor science and technology*, 8(1):1, 1993.
- [3] Kadra Branker, MJM Pathak, and Joshua M Pearce. A review of solar photovoltaic levelized cost of electricity. *Renewable and Sustainable Energy Reviews*, 15(9):4470–4482, 2011.
- [4] J Britt and C Ferekides. Thin-film cds/cdte solar cell with 15.8% efficiency. *Applied Physics Letters*, 62(22):2851–2852, 1993.
- [5] Ingrid Repins, Miguel A Contreras, Brian Egaas, Clay DeHart, John Scharf, Craig L Perkins, Bobby To, and Rommel Noufi. 19.9%-efficient zno/cds/cuingase2 solar cell with 81.2% fill factor. *Progress in Photovoltaics: Research and applications*, 16(3):235–239, 2008.
- [6] Michael Graetzel, René AJ Janssen, David B Mitzi, and Edward H Sargent. Materials interface engineering for solution-processed photovoltaics. *Nature*, 488(7411):304, 2012.
- [7] Brian Oregan and M Grfitzeli. A low-cost, high-efficiency solar cell based on dye-sensitized. *nature*, 353(6346):737–740, 1991.
- [8] Ching W Tang. Two-layer organic photovoltaic cell. *Applied Physics Letters*, 48(2):183–185, 1986.
- [9] Teodor K Todorov, Kathleen B Reuter, and David B Mitzi. High-efficiency solar cell with earth-abundant liquid-processed absorber. *Advanced materials*, 22(20), 2010.
- [10] Gang Yu, Jun Gao, Jan C Hummelen, Fred Wudl, and Alan J Heeger. Polymer photovoltaic cells: Enhanced efficiencies via a network of internal donor-acceptor heterojunctions. *Science*, 270(5243):1789, 1995.
- [11] Wan-Jian Yin, Ji-Hui Yang, Joongoo Kang, Yanfa Yan, and Su-Huai Wei. Halide perovskite materials for solar cells: a theoretical review. *Journal of Materials Chemistry A*, 3(17):8926–8942, 2015.

- [12] Hui-Seon Kim, Chang-Ryul Lee, Jeong-Hyeok Im, Ki-Beom Lee, Thomas Moehl, Arianna Marchioro, Soo-Jin Moon, Robin Humphry-Baker, Jun-Ho Yum, Jacques E Moser, et al. Lead iodide perovskite sensitized all-solid-state submicron thin film mesoscopic solar cell with efficiency exceeding 9%. *Scientific reports*, 2, 2012.
- [13] Michael M Lee, Joël Teuscher, Tsutomu Miyasaka, Takuro N Murakami, and Henry J Snaith. Efficient hybrid solar cells based on meso-superstructured organometal halide perovskites. *Science*, 338(6107):643–647, 2012.
- [14] Dieter Weber. $\text{CH}_3\text{NH}_3\text{PbX}_3$, ein pb (ii)-system mit kubischer perowskitstruktur/ $\text{CH}_3\text{NH}_3\text{PbX}_3$, a pb (ii)-system with cubic perovskite structure. *Zeitschrift für Naturforschung B*, 33(12):1443–1445, 1978.
- [15] Akihiro Kojima, Kenjiro Teshima, Yasuo Shirai, and Tsutomu Miyasaka. Organometal halide perovskites as visible-light sensitizers for photovoltaic cells. *Journal of the American Chemical Society*, 131(17):6050–6051, 2009.
- [16] Jeong-Hyeok Im, Chang-Ryul Lee, Jin-Wook Lee, Sang-Won Park, and Nam-Gyu Park. 6.5% efficient perovskite quantum-dot-sensitized solar cell. *Nanoscale*, 3(10):4088–4093, 2011.
- [17] Nam Joong Jeon, Jun Hong Noh, Young Chan Kim, Woon Seok Yang, Seungchan Ryu, and Sang Il Seok. Solvent engineering for high-performance inorganic–organic hybrid perovskite solar cells. *Nature materials*, 13(9):897–903, 2014.
- [18] Woon Seok Yang, Jun Hong Noh, Nam Joong Jeon, Young Chan Kim, Seungchan Ryu, Jangwon Seo, and Sang Il Seok. High-performance photovoltaic perovskite layers fabricated through intramolecular exchange. *Science*, 348(6240):1234–1237, 2015.
- [19] Cheng Bi, Yuchuan Shao, Yongbo Yuan, Zhengguo Xiao, Chenggong Wang, Yongli Gao, and Jinsong Huang. Understanding the formation and evolution of interdiffusion grown organolead halide perovskite thin films by thermal annealing. *Journal of Materials Chemistry A*, 2(43):18508–18514, 2014.
- [20] Zhengguo Xiao, Cheng Bi, Yuchuan Shao, Qingfeng Dong, Qi Wang, Yongbo Yuan, Chenggong Wang, Yongli Gao, and Jinsong Huang. Efficient, high yield perovskite photovoltaic devices grown by interdiffusion of solution-processed precursor stacking layers. *Energy & Environmental Science*, 7(8):2619–2623, 2014.
- [21] Nam Joong Jeon, Jaemin Lee, Jun Hong Noh, Mohammad Khaja Nazeeruddin, Michael Gratzel, and Sang Il Seok. Efficient inorganic–organic hybrid perovskite solar cells based on pyrene arylamine derivatives as hole-transporting materials. *Journal of the American Chemical Society*, 135(51):19087–19090, 2013.

- [22] Nam Joong Jeon, Hag Geun Lee, Young Chan Kim, Jangwon Seo, Jun Hong Noh, Jaemin Lee, and Sang Il Seok. o-methoxy substituents in spiro-ometad for efficient inorganic–organic hybrid perovskite solar cells. *Journal of the American Chemical Society*, 136(22):7837–7840, 2014.
- [23] Huanping Zhou, Qi Chen, Gang Li, Song Luo, Tze-bing Song, Hsin-Sheng Duan, Ziruo Hong, Jingbi You, Yongsheng Liu, and Yang Yang. Interface engineering of highly efficient perovskite solar cells. *Science*, 345(6196):542–546, 2014.
- [24] Henry J Snaith. Perovskites: the emergence of a new era for low-cost, high-efficiency solar cells. *The Journal of Physical Chemistry Letters*, 4(21):3623–3630, 2013.
- [25] Samuel D Stranks, Giles E Eperon, Giulia Grancini, Christopher Menelaou, Marcelo JP Alcocer, Tomas Leijtens, Laura M Herz, Annamaria Petrozza, and Henry J Snaith. Electron-hole diffusion lengths exceeding 1 micrometer in an organometal trihalide perovskite absorber. *Science*, 342(6156):341–344, 2013.
- [26] Guichuan Xing, Nripan Mathews, Shuangyong Sun, Swee Sien Lim, Yeng Ming Lam, Michael Grätzel, Subodh Mhaisalkar, and Tze Chien Sum. Long-range balanced electron-and hole-transport lengths in organic-inorganic $\text{ch}_3\text{nh}_3\text{pb}_3\text{i}_3$. *Science*, 342(6156):344–347, 2013.
- [27] Joseph S Manser and Prashant V Kamat. Band filling with free charge carriers in organometal halide perovskites. *Nature Photonics*, 8(9):737–743, 2014.
- [28] Lili Wang, Christopher McCleese, Anton Kovalsky, Yixin Zhao, and Clemens Burda. Femtosecond time-resolved transient absorption spectroscopy of $\text{ch}_3\text{nh}_3\text{pb}_3\text{i}_3$ perovskite films: evidence for passivation effect of pb_2i_2 . *Journal of the American Chemical Society*, 136(35):12205–12208, 2014.
- [29] Oliver Flender, Johannes R Klein, Thomas Lenzer, and Kawon Oum. Ultrafast photoinduced dynamics of the organolead trihalide perovskite $\text{ch}_3\text{nh}_3\text{pb}_3\text{i}_3$ on mesoporous tio_2 scaffolds in the 320–920 nm range. *Physical Chemistry Chemical Physics*, 17(29):19238–19246, 2015.
- [30] Aslihan Babayigit, Anitha Ethirajan, Marc Muller, and Bert Conings. Toxicity of organometal halide perovskite solar cells. *Nature materials*, 15:247–251, 2016.
- [31] Feng Hao, Constantinos C Stoumpos, Duyen Hanh Cao, Robert PH Chang, and Mercuri G Kanatzidis. Lead-free solid-state organic-inorganic halide perovskite solar cells. *Nature Photonics*, 8(6):489–494, 2014.
- [32] Mulmudi Hemant Kumar, Sabba Dharani, Wei Lin Leong, Pablo P Boix, Ravi Ramanujam Prabhakar, Tom Baikie, Chen Shi, Hong Ding, Ramamoorthy Ramesh, Mark Asta, et al. Lead-free halide perovskite solar cells with high photocurrents realized through vacancy modulation. *Advanced Materials*, 26(41):7122–7127, 2014.

- [33] Kenneth P Marshall, Richard I Walton, and Ross A Hatton. Tin perovskite/fullerene planar layer photovoltaics: improving the efficiency and stability of lead-free devices. *Journal of Materials Chemistry A*, 3(21):11631–11640, 2015.
- [34] Takamichi Yokoyama, Duyen H Cao, Constantinos C Stoumpos, Tze-Bin Song, Yoshiharu Sato, Shinji Aramaki, and Mercouri G Kanatzidis. Overcoming short-circuit in lead-free $\text{CH}_3\text{NH}_3\text{SnI}_3$ perovskite solar cells via kinetically controlled gas–solid reaction film fabrication process. *The journal of physical chemistry letters*, 7(5):776–782, 2016.
- [35] Bayrammurad Saparov, Feng Hong, Jon-Paul Sun, Hsin-Sheng Duan, Weiwei Meng, Samuel Cameron, Ian G Hill, Yanfa Yan, and David B Mitzi. Thin-film preparation and characterization of $\text{Cs}_3\text{Sb}_2\text{I}_9$: A lead-free layered perovskite semiconductor. *Chem. Mater*, 27(16):5622–5632, 2015.
- [36] Malin B Johansson, Huimin Zhu, and Erik MJ Johansson. Extended photo-conversion spectrum in low-toxic bismuth halide perovskite solar cells. *The journal of physical chemistry letters*, 7(17):3467–3471, 2016.
- [37] Duyen H Cao, Constantinos C Stoumpos, Takamichi Yokoyama, Jenna L Logsdon, Tze-Bin Song, Omar K Farha, Michael R Wasielewski, Joseph T Hupp, and Mercouri G Kanatzidis. Thin films and solar cells based on semiconducting two-dimensional ruddlesden–popper $(\text{CH}_3(\text{CH}_2)_n\text{NH}_3)_2(\text{CH}_3\text{NH}_3)_{n-1}\text{SnI}_3$ perovskites. 2017.
- [38] Hui-Seon Kim, Ja-Young Seo, and Nam-Gyu Park. Material and device stability in perovskite solar cells. *ChemSusChem*, 2016.
- [39] Tomas Leijtens, Giles E Eperon, Nakita K Noel, Severin N Habisreutinger, Annamaria Petrozza, and Henry J Snaith. Stability of metal halide perovskite solar cells. *Advanced Energy Materials*, 5(20), 2015.
- [40] Ian C Smith, Eric T Hoke, Diego Solis-Ibarra, Michael D McGehee, and Hemamala I Karunadasa. A layered hybrid perovskite solar-cell absorber with enhanced moisture stability. *Angewandte Chemie*, 126(42):11414–11417, 2014.
- [41] Duyen H Cao, Constantinos C Stoumpos, Omar K Farha, Joseph T Hupp, and Mercouri G Kanatzidis. 2d homologous perovskites as light-absorbing materials for solar cell applications. *Journal of the American Chemical Society*, 137(24):7843–7850, 2015.
- [42] Hsinhan Tsai, Wanyi Nie, Jean-Christophe Blancon, Constantinos C Stoumpos, Reza Asadpour, Boris Harutyunyan, Amanda J Neukirch, Rafael Verduzco, Jared J Crochet, Sergei Tretiak, et al. High-efficiency two-dimensional ruddlesden–popper perovskite solar cells. *Nature*, 536(7616):312–316, 2016.

- [43] J George Bednorz and K Alex Müller. Possible hightc superconductivity in the ba- la- cu- o system. *Zeitschrift für Physik B Condensed Matter*, 64(2):189–193, 1986.
- [44] RJ Cava, B Batlogg, RB Van Dover, DW Murphy, S Sunshine, T Siegrist, JP Remeika, EA Rietman, S Zahurak, and GP Espinosa. Bulk superconductivity at 91 k in single-phase oxygen-deficient perovskite ba₂ycu₃o_{9- δ} . *Physical Review Letters*, 58(16):1676, 1987.
- [45] Y Maeno, H Hashimoto, K Yoshida, S Nishizaki, et al. Superconductivity in a layered perovskite without copper. *Nature*, 372(6506):532, 1994.
- [46] T He, Q Huang, AP Ramirez, Y Wang, KA Regan, N Rogado, MA Hayward, MK Haas, JS Slusky, K Inumaru, et al. Superconductivity in the non-oxide perovskite mgcni₃. *arXiv preprint cond-mat/0103296*, 2001.
- [47] KI Kobayashi, T Kimura, H Sawada, K Terakura, and Y Tokura. Room-temperature magnetoresistance in an oxide material with an ordered double-perovskite structure. *Nature*, 395(6703):677, 1998.
- [48] Ronald E Cohen. Origin of ferroelectricity in perovskite oxides. *Nature*, 358(6382):136–138, 1992.
- [49] JB Philipp, D Reisinger, M Schonecke, A Marx, A Erb, L Alff, R Gross, and J Klein. Spin-dependent transport in the double-perovskite sr₂crwo₆. *Applied physics letters*, 79(22):3654–3656, 2001.
- [50] Jingshan Hou, Xin Yin, Yongzheng Fang, Fuqiang Huang, and Weizhong Jiang. Novel red-emitting perovskite-type phosphor cala_{1-x}m_xgm_{o6}: xeu³⁺(m= nb, ta) for white led application. *Optical Materials*, 34(8):1394–1397, 2012.
- [51] Samuel D Stranks and Henry J Snaith. Metal-halide perovskites for photovoltaic and light-emitting devices. *Nature nanotechnology*, 10(5):391–402, 2015.
- [52] Zhi-Kuang Tan, Reza Saberi Moghaddam, May Ling Lai, Pablo Docampo, Ruben Higler, Felix Deschler, Michael Price, Aditya Sadhanala, Luis M Pazos, Dan Credginton, et al. Bright light-emitting diodes based on organometal halide perovskite. *Nature nanotechnology*, 9(9):687–692, 2014.
- [53] Felix Deschler, Michael Price, Sandeep Pathak, Lina E Klintberg, David-Dominik Jarausch, Ruben Higler, Sven Huttner, Tomas Leijtens, Samuel D Stranks, Henry J Snaith, et al. High photoluminescence efficiency and optically pumped lasing in solution-processed mixed halide perovskite semiconductors. *The journal of physical chemistry letters*, 5(8):1421–1426, 2014.

- [54] Sergii Yakunin, Loredana Protesescu, Franziska Krieg, Maryna I Bodnarchuk, Georgian Nedelcu, Markus Humer, Gabriele De Luca, Manfred Fiebig, Wolfgang Heiss, and Maksym V Kovalenko. Low-threshold amplified spontaneous emission and lasing from colloidal nanocrystals of caesium lead halide perovskites. *Nature communications*, 6:8056, 2015.
- [55] Pazhoor Varghese Bijumon, Pezholil Mohanan, and Mailadil Thomas Sebastian. Synthesis, characterization and properties of $\text{Ca}_5\text{A}_2\text{TiO}_{12}$ ($a = nb, ta$) ceramic dielectric materials for applications in microwave telecommunication systems. *Japanese journal of applied physics*, 41(6R):3834, 2002.
- [56] Atsufumi Hirohata, Hiroaki Sukegawa, Hideto Yanagihara, Igor Žutić, Takeshi Seki, Shigemi Mizukami, and Raja Swaminathan. Roadmap for emerging materials for spintronic device applications. *IEEE Transactions on Magnetics*, 51(10):1–11, 2015.
- [57] Patrick Odenthal, William Talmadge, Nathan Gundlach, Ruizhi Wang, Chuang Zhang, Dali Sun, Zhi-Gang Yu, Z Vally Vardeny, and Yan S Li. Spin-polarized exciton quantum beating in hybrid organic-inorganic perovskites. *Nature Physics*, 2017.
- [58] JW Anthony, RA Bideaux, KW Bladh, and MC Nichols. Handbook of mineralogy; mineralogical society of america: Chantilly, va, 2001. *There is no corresponding record for this reference.*
- [59] Bettina V Lotsch. New light on an old story: perovskites go solar. *Angewandte Chemie International Edition*, 53(3):635–637, 2014.
- [60] Teruya Ishihara, Jun Takahashi, and Takenari Goto. Exciton state in two-dimensional perovskite semiconductor $(\text{C}_{10}\text{H}_{21}\text{NH}_3)_2\text{PbI}_4$. *Solid state communications*, 69(9):933–936, 1989.
- [61] X Hong, T Ishihara, and AV Nurmikko. Dielectric confinement effect on excitons in PbI_4 -based layered semiconductors. *Physical Review B*, 45(12):6961, 1992.
- [62] EA Muljarov, SG Tikhodeev, NA Gippius, and Teruya Ishihara. Excitons in self-organized semiconductor/insulator superlattices: PbI_4 -based perovskite compounds. *Physical Review B*, 51(20):14370, 1995.
- [63] Christian Wehrenfennig, Giles E Eperon, Michael B Johnston, Henry J Snaith, and Laura M Herz. High charge carrier mobilities and lifetimes in organolead trihalide perovskites. *Advanced materials*, 26(10):1584–1589, 2014.
- [64] Michael B Johnston and Laura M Herz. Hybrid perovskites for photovoltaics: Charge-carrier recombination, diffusion, and radiative efficiencies. *Accounts of chemical research*, 49(1):146–154, 2015.

- [65] Laura M Herz. Charge-carrier dynamics in organic-inorganic metal halide perovskites. *Annual review of physical chemistry*, 67:65–89, 2016.
- [66] Paul E Shaw, Arvydas Ruseckas, and Ifor DW Samuel. Exciton diffusion measurements in poly (3-hexylthiophene). *Advanced Materials*, 20(18):3516–3520, 2008.
- [67] Zhi Guo, Joseph S Manser, Yan Wan, Prashant V Kamat, and Libai Huang. Spatial and temporal imaging of long-range charge transport in perovskite thin films by ultrafast microscopy. *Nature communications*, 6:7471, 2015.
- [68] A Haugeneder, M Neges, C Kallinger, W Spirkel, U Lemmer, J Feldmann, Ullrich Scherf, E Harth, A Gügel, and Klaus Müllen. Exciton diffusion and dissociation in conjugated polymer/fullerene blends and heterostructures. *Physical Review B*, 59(23):15346, 1999.
- [69] Jessica E Kroeze, Tom J Savenije, Martien JW Vermeulen, and John M Warman. Contactless determination of the photoconductivity action spectrum, exciton diffusion length, and charge separation efficiency in polythiophene-sensitized tio₂ bilayers. *The Journal of Physical Chemistry B*, 107(31):7696–7705, 2003.
- [70] Richard R Lunt, Jay B Benziger, and Stephen R Forrest. Relationship between crystalline order and exciton diffusion length in molecular organic semiconductors. *Advanced Materials*, 22(11):1233–1236, 2010.
- [71] Peter Peumans, Aharon Yakimov, and Stephen R Forrest. Small molecular weight organic thin-film photodetectors and solar cells. *Journal of Applied Physics*, 93(7):3693–3723, 2003.
- [72] David Zhitomirsky, Oleksandr Voznyy, Sjoerd Hoogland, and Edward H Sargent. Measuring charge carrier diffusion in coupled colloidal quantum dot solids. *ACS nano*, 7(6):5282–5290, 2013.
- [73] Dong Shi, Valerio Adinolfi, Riccardo Comin, Mingjian Yuan, Erkki Alarousu, Andrei Buin, Yin Chen, Sjoerd Hoogland, Alexander Rothenberger, Khabiboulakh Katsiev, et al. Low trap-state density and long carrier diffusion in organolead trihalide perovskite single crystals. *Science*, 347(6221):519–522, 2015.
- [74] Rebecca L Milot, Rebecca J Sutton, Giles E Eperon, Amir Abbas Haghighirad, Josue Martinez Hardigree, Laura Miranda, Henry J Snaith, Michael B Johnston, and Laura M Herz. Charge-carrier dynamics in 2d hybrid metal-halide perovskites. *Nano Lett*, 16(11):7001–7007, 2016.
- [75] X Hong, T Ishihara, and AV Nurmikko. Photoconductivity and electroluminescence in lead iodide based natural quantum well structures. *Solid state communications*, 84(6):657–661, 1992.

- [76] Constantinos C Stoumpos, Duyen H Cao, Daniel J Clark, Joshua Young, James M Rondinelli, Joon I Jang, Joseph T Hupp, and Mercouri G Kanatzidis. Ruddlesden–popper hybrid lead iodide perovskite 2d homologous semiconductors. *Chemistry of Materials*, 28(8):2852–2867, 2016.
- [77] James M Ball, Michael M Lee, Andrew Hey, and Henry J Snaith. Energy environ. *Sci*, 6(6):1739, 2013.
- [78] Lioz Etgar, Peng Gao, Zhaosheng Xue, Qin Peng, Aravind Kumar Chandiran, Bin Liu, Md K Nazeeruddin, and Michael Gratzel. Mesoscopic $\text{ch}_3\text{nh}_3\text{pbi}_3/\text{tio}_2$ heterojunction solar cells. *Journal of the American Chemical Society*, 134(42):17396–17399, 2012.
- [79] Jin Hyuck Heo, Sang Hyuk Im, Jun Hong Noh, Tarak N Mandal, Choong-Sun Lim, Jeong Ah Chang, Yong Hui Lee, Hi-jung Kim, Arpita Sarkar, Md K Nazeeruddin, et al. Efficient inorganic-organic hybrid heterojunction solar cells containing perovskite compound and polymeric hole conductors. *Nature photonics*, 7(6):486–491, 2013.
- [80] Jacky Even, Laurent Pedesseau, Jean-Marc Jancu, and Claudine Katan. Importance of spin–orbit coupling in hybrid organic/inorganic perovskites for photovoltaic applications. *The Journal of Physical Chemistry Letters*, 4(17):2999–3005, 2013.
- [81] HA Weakliem and D Redfield. Temperature dependence of the optical properties of silicon. *Journal of Applied Physics*, 50(3):1491–1493, 1979.
- [82] Supriyo Datta and Biswajit Das. Electronic analog of the electro-optic modulator. *Applied Physics Letters*, 56(7):665–667, 1990.
- [83] SA Wolf, DD Awschalom, RA Buhrman, JM Daughton, S Von Molnar, ML Roukes, A Yu Chtchelkanova, and DM Treger. Spintronics: a spin-based electronics vision for the future. *Science*, 294(5546):1488–1495, 2001.
- [84] Igor Žutić, Jaroslav Fabian, and S Das Sarma. Spintronics: Fundamentals and applications. *Reviews of modern physics*, 76(2):323, 2004.
- [85] David D Awschalom and Michael E Flatté. Challenges for semiconductor spintronics. *Nature physics*, 3(3):153, 2007.
- [86] Yuji Nishikawa, Atsushi Tackeuchi, Satoshi Nakamura, Shunichi Muto, and Naoki Yokoyama. All-optical picosecond switching of a quantum well etalon using spin-polarization relaxation. *Applied physics letters*, 66(7):839–841, 1995.
- [87] Jörg Rudolph, Daniel Hägele, HM Gibbs, G Khitrova, and M Oestreich. Laser threshold reduction in a spintronic device. *Applied Physics Letters*, 82(25):4516–4518, 2003.

- [88] Kimberley C Hall and Michael E Flatte. Performance of a spin-based insulated gate field effect transistor. *Applied Physics Letters*, 88(16):162503, 2006.
- [89] JT Hyland, GT Kennedy, A Miller, and Chris C Button. Spin relaxation and all optical polarization switching at 1.52 micrometres in ingaas (p)/ingaasp multiple quantum wells. *Semiconductor science and technology*, 14(3):215, 1999.
- [90] Tadashi Kawazoe, Tomobumi Mishina, and Yasuaki Masumoto. Highly repetitive picosecond polarization switching in type-ii algaas/alas multiple quantum well structures. *Japanese journal of applied physics*, 32(12A):L1756, 1993.
- [91] Atsushi Tackeuchi, Osamu Wada, and Yuji Nishikawa. Electron spin relaxation in ingaas/inp multiple-quantum wells. *Applied Physics Letters*, 70(9):1131–1133, 1997.
- [92] KC Hall, SW Leonard, HM van Driel, AR Kost, E Selvig, and DH Chow. Sub-picosecond spin relaxation in gaassb multiple quantum wells. *Applied Physics Letters*, 75(26):4156–4158, 1999.
- [93] JM Kikkawa and DD Awschalom. Lateral drag of spin coherence in gallium arsenide. *Nature*, 397(6715):139, 1999.
- [94] EI Rashba. Theory of electrical spin injection: Tunnel contacts as a solution of the conductivity mismatch problem. *Physical Review B*, 62(24):R16267, 2000.
- [95] Aubrey T Hanbicki, BT Jonker, G Itskos, G Kioseoglou, and A Petrou. Efficient electrical spin injection from a magnetic metal/tunnel barrier contact into a semiconductor. *Applied Physics Letters*, 80(7):1240–1242, 2002.
- [96] ZG Yu and ME Flatté. Spin diffusion and injection in semiconductor structures: Electric field effects. *Physical Review B*, 66(23):235302, 2002.
- [97] Xiaohua Lou, Christoph Adelman, Scott A Crooker, Eric S Garlid, Jianjie Zhang, SM Reddy, Soren D Flexner, Chris J Palmstrom, and Paul A Crowell. Electrical detection of spin transport in lateral ferromagnet-semiconductor devices. *arXiv preprint cond-mat/0701021*, 2006.
- [98] Hyun Cheol Koo, Jae Hyun Kwon, Jonghwa Eom, Joonyeon Chang, Suk Hee Han, and Mark Johnson. Control of spin precession in a spin-injected field effect transistor. *Science*, 325(5947):1515–1518, 2009.
- [99] Pojen Chuang, Sheng-Chin Ho, LW Smith, F Sfigakis, M Pepper, Chin-Hung Chen, Ju-Chun Fan, JP Griffiths, I Farrer, HE Beere, et al. All-electric all-semiconductor spin field-effect transistors. *Nature nanotechnology*, 10(1):35–39, 2015.
- [100] C Betthausen, Tobias Dollinger, Henri Saarikoski, V Kolkovsky, G Karczewski, T Wojtowicz, Klaus Richter, and Dieter Weiss. Spin-transistor action via tunable landau-zener transitions. *Science*, 337(6092):324–327, 2012.

- [101] YK Kato, RC Myers, AC Gossard, and DD Awschalom. Observation of the spin hall effect in semiconductors. *science*, 306(5703):1910–1913, 2004.
- [102] JWG Van den Berg, S Nadj-Perge, VS Pribiag, SR Plissard, EPAM Bakkers, SM Frolov, and LP Kouwenhoven. Fast spin-orbit qubit in an indium antimonide nanowire. *Physical review letters*, 110(6):066806, 2013.
- [103] T Kimura, Y Otani, T Sato, S Takahashi, and S Maekawa. Room-temperature reversible spin hall effect. *Physical review letters*, 98(15):156601, 2007.
- [104] Ron Jansen. Silicon spintronics. *Nature materials*, 11(5):400, 2012.
- [105] Wei Han, Roland K Kawakami, Martin Gmitra, and Jaroslav Fabian. Graphene spintronics. *Nature nanotechnology*, 9(10):794–807, 2014.
- [106] VV Dobrovitski, GD Fuchs, AL Falk, C Santori, and DD Awschalom. Quantum control over single spins in diamond. *Annu. Rev. Condens. Matter Phys.*, 4(1):23–50, 2013.
- [107] Minsung Kim, Jino Im, Arthur J Freeman, Jisoon Ihm, and Hosub Jin. Switchable $s = 1/2$ and $j = 1/2$ rashba bands in ferroelectric halide perovskites. *Proceedings of the National Academy of Sciences*, 111(19):6900–6904, 2014.
- [108] David Giovanni, Hong Ma, Julianto Chua, Michael Gratzel, Ramamoorthy Ramesh, Subodh Mhaisalkar, Nripan Mathews, and Tze Chien Sum. Highly spin-polarized carrier dynamics and ultralarge photoinduced magnetization in $\text{ch}_3\text{nh}_3\text{pb}_3\text{i}_3$ perovskite thin films. *Nano letters*, 15(3):1553–1558, 2015.
- [109] C Zhang, D Sun, CX Sheng, YX Zhai, K Mielczarek, A Zakhidov, and ZV Vardeny. Magnetic field effects in hybrid perovskite devices. *Nature Physics*, 11(5):427, 2015.
- [110] Daniel Niesner, Max Wilhelm, Ievgen Levchuk, Andres Osvet, Shreetu Shrestha, Mirosław Batentschuk, Christoph Brabec, and Thomas Fauster. Giant rashba splitting in $\text{ch}_3\text{nh}_3\text{pb}_3\text{i}_3$ organic-inorganic perovskite. *Physical review letters*, 117(12):126401, 2016.
- [111] Dali Sun, Chuang Zhang, Marzieh Kavand, Kipp J van Schooten, Hans Malissa, Matthew Groesbeck, Ryan McLaughlin, Christoph Boehme, and Z Vally Vardeny. Spintronics of organometal trihalide perovskites. *arXiv preprint arXiv:1608.00993*, 2016.
- [112] Mikaël Kepenekian, Roberto Robles, Claudine Katan, Daniel Saporì, Laurent Pedesseau, and Jacky Even. Rashba and dresselhaus effects in hybrid organic–inorganic perovskites: From basics to devices. *ACS nano*, 9(12):11557–11567, 2015.

- [113] David Giovanni, Wee Kiang Chong, Herlina Arianita Dewi, Krishnamoorthy Thirumal, Ishita Neogi, Ramamoorthy Ramesh, Subodh Mhaisalkar, Nripan Mathews, and Tze Chien Sum. Tunable room-temperature spin-selective optical stark effect in solution-processed layered halide perovskites. *Science advances*, 2(6):e1600477, 2016.
- [114] Jie Ma and Lin-Wang Wang. Nanoscale charge localization induced by random orientations of organic molecules in hybrid perovskite $\text{CH}_3\text{NH}_3\text{PbI}_3$. *Nano letters*, 15(1):248–253, 2014.
- [115] Samuel A March, Drew B Riley, Charlotte Clegg, Daniel Webber, Xinyu Liu, Margaret Dobrowolska, Jacek K Furdyna, Ian G Hill, and Kimberley C Hall. Four-wave mixing in perovskite photovoltaic materials reveals long dephasing times and weaker many-body interactions than GaAs. *ACS Photonics*, 4(6):1515–1521, 2017.
- [116] Jacky Even, Laurent Pedesseau, M-A Dupertuis, J-M Jancu, and Claudine Katan. Electronic model for self-assembled hybrid organic/perovskite semiconductors: Reverse band edge electronic states ordering and spin-orbit coupling. *Physical Review B*, 86(20):205301, 2012.
- [117] Jagdeep Shah. *Ultrafast spectroscopy of semiconductors and semiconductor nanostructures*, volume 115. Springer Science & Business Media, 2013.
- [118] GL Bir, AG Aronov, and GE Pikus. Spin relaxation of electrons due to scattering by holes. *Zh. Eksp. Teor. Fiz*, 69(4):1382, 1975.
- [119] Y Yafet. g factors and spin-lattice relaxation of conduction electrons. *Solid state physics*, 14:1–98, 1963.
- [120] R J Elliott. Theory of the effect of spin-orbit coupling on magnetic resonance in some semiconductors. *Physical Review*, 96(2):266, 1954.
- [121] J-N Chazalviel. Spin relaxation of conduction electrons in n-type indium antimonide at low temperature. *Physical Review B*, 11(4):1555, 1975.
- [122] GE Pikus and AN Titkov. Spin relaxation under optical orientation in semiconductors. *Optical Orientation*, 8:73–131, 1984.
- [123] MI Dyakonov and VI Perel. Spin relaxation of conduction electrons in noncentrosymmetric semiconductors. *Soviet Physics Solid State, Ussr*, 13(12):3023–3026, 1972.
- [124] H Ohno et al. Semiconductor spintronics and quantum computation. *Semiconductor Spintronics and Quantum computation*, 2002.

- [125] Atsuhiko Miyata, Anatolie Mitioglu, Paulina Plochocka, Oliver Portugall, Jacob Tse-Wei Wang, Samuel D Stranks, Henry J Snaith, and Robin J Nicholas. Direct measurement of the exciton binding energy and effective masses for charge carriers in an organic-inorganic tri-halide perovskite. *arXiv preprint arXiv:1504.07025*, 2015.
- [126] Samuel A March, Charlotte Clegg, Drew B Riley, Daniel Webber, Ian G Hill, and Kimberley C Hall. Simultaneous observation of free and defect-bound excitons in $\text{ch}_3\text{nh}_3\text{pb}_i\text{b}_3$ using four-wave mixing spectroscopy. *Scientific reports*, 6:39139, 2016.
- [127] Fedor T Vasko and Alex V Kuznetsov. *Electronic states and optical transitions in semiconductor heterostructures*. Springer Science & Business Media, 2012.
- [128] T Uenoyama and LJ Sham. Hole relaxation and luminescence polarization in doped and undoped quantum wells. *Physical review letters*, 64(25):3070, 1990.
- [129] P Murzyn, CR Pidgeon, PJ Phillips, JP Wells, NT Gordon, T Ashley, JH Jefferson, TM Burke, J Giess, M Merrick, et al. Electron spin lifetimes in long-wavelength hg 1- x cd x te and insb at elevated temperature. *Physical Review B*, 67(23):235202, 2003.
- [130] Otfried Madelung. *Semiconductorsbasic data*. Springer Science & Business Media, 2012.
- [131] JM Kikkawa and DD Awschalom. Resonant spin amplification in n-type gaas. *Physical Review Letters*, 80(19):4313, 1998.
- [132] Mikael Kepenekian and Jacky Even. Rashba and dresselhaus couplings in halide perovskites: Accomplishments and opportunities for spintronics and spin-orbitronics. *The Journal of Physical Chemistry Letters*, 2017.
- [133] Emmanuel I Rashba. Properties of semiconductors with an extremum loop. i. cyclotron and combinational resonance in a magnetic field perpendicular to the plane of the loop. *Physics of the Solid State*, 2:1109–1122, 1960.
- [134] Yu A Bychkov and EI Rashba. Properties of a 2d electron gas with lifted spectral degeneracy. *JETP lett*, 39(2):78, 1984.
- [135] G. Dresselhaus. Spin-orbit coupling effects in zinc blende structures. *Phys. Rev.*, 100:580–586, Oct 1955.
- [136] Jacky Even, Laurent Pedesseau, Jean-Marc Jancu, and Claudine Katan. Dft and k·p modelling of the phase transitions of lead and tin halide perovskites for photovoltaic cells. *physica status solidi (RRL)-Rapid Research Letters*, 8(1):31–35, 2014.

- [137] Federico Brivio, Keith T Butler, Aron Walsh, and Mark Van Schilfgaarde. Relativistic quasiparticle self-consistent electronic structure of hybrid halide perovskite photovoltaic absorbers. *Physical Review B*, 89(15):155204, 2014.
- [138] Anna Amat, Edoardo Mosconi, Enrico Ronca, Claudio Quarti, Paolo Umari, Md K Nazeeruddin, Michael Gratzel, and Filippo De Angelis. Cation-induced band-gap tuning in organohalide perovskites: interplay of spin-orbit coupling and octahedra tilting. *Nano letters*, 14(6):3608–3616, 2014.
- [139] William Lawrence Bragg. The specular reflection of x-rays. *Nature*, 90(2250):410, 1912.
- [140] Junxue Liu, Jing Leng, Kaifeng Wu, Jun Zhang, and Shengye Jin. Observation of internal photoinduced electron and hole separation in hybrid two-dimensional perovskite films. *J. Am. Chem. Soc.*, 139(4):1432–1435, 2017.
- [141] J Tauc, Radu Grigorovici, and Anina Vancu. Optical properties and electronic structure of amorphous germanium. *physica status solidi (b)*, 15(2):627–637, 1966.
- [142] Jan Tauc. Optical properties and electronic structure of amorphous ge and si. *Materials Research Bulletin*, 3(1):37–46, 1968.
- [143] EA Davis and Nff Mott. Conduction in non-crystalline systems v. conductivity, optical absorption and photoconductivity in amorphous semiconductors. *Philosophical Magazine*, 22(179):0903–0922, 1970.
- [144] Constantinos C Stoumpos, Christos D Malliakas, and Mercuri G Kanatzidis. Semiconducting tin and lead iodide perovskites with organic cations: phase transitions, high mobilities, and near-infrared photoluminescent properties. *Inorganic chemistry*, 52(15):9019–9038, 2013.
- [145] David G Billing and Andreas Lemmerer. Synthesis, characterization and phase transitions in the inorganic-organic layered perovskite-type hybrids [(cnh_{2n+1}nh₃)₂pb₄], n= 4, 5 and 6. *Acta Crystallographica Section B: Structural Science*, 63(5):735–747, 2007.
- [146] Claudio Quarti, Edoardo Mosconi, James M Ball, Valerio D’Innocenzo, Chen Tao, Sandeep Pathak, Henry J Snaith, Annamaria Petrozza, and Filippo De Angelis. Structural and optical properties of methylammonium lead iodide across the tetragonal to cubic phase transition: implications for perovskite solar cells. *Energy & Environmental Science*, 9(1):155–163, 2016.
- [147] Mark T Weller, Oliver J Weber, Paul F Henry, Antonietta M Di Pumpo, and Thomas C Hansen. Complete structure and cation orientation in the perovskite photovoltaic methylammonium lead iodide between 100 and 352 k. *Chemical Communications*, 51(20):4180–4183, 2015.

- [148] DS Bhavsar and KB Saraf. Optical properties of lead iodide between 0.4946 and 6.185 eV. *Journal of Materials Science: Materials in Electronics*, 14(4):195–198, 2003.
- [149] Krzysztof Galkowski, Anatolie Mitioglu, Atsuhiko Miyata, Paulina Plochocka, Oliver Portugall, Giles E Eperon, Jacob Tse-Wei Wang, Thomas Stergiopoulos, Samuel D Stranks, Henry J Snaith, et al. Determination of the exciton binding energy and effective masses for methylammonium and formamidinium lead trihalide perovskite semiconductors. *Energy & Environmental Science*, 9(3):962–970, 2016.
- [150] Valerio D’Innocenzo, Giulia Grancini, Marcelo JP Alcocer, Ajay Ram Srimath Kandada, Samuel D Stranks, Michael M Lee, Guglielmo Lanzani, Henry J Snaith, and Annamaria Petrozza. Excitons versus free charges in organo-lead tri-halide perovskites. *Nature communications*, 5:3586, 2014.
- [151] PCM Christianen, EJA De Bekker, HJA Bluyssen, PR Hageman, and MR Leys. Cooling reduction due to a rapid density decay of hot carriers in GaAs. *Semiconductor Science and Technology*, 9(5S):713, 1994.
- [152] Ryota Terauchi, Yuzo Ohno, Taro Adachi, Arao Sato, Fumihiro Matsukura, Atsushi Tackeuchi, and Hideo Ohno. Carrier mobility dependence of electron spin relaxation in GaAs quantum wells. *Japanese journal of applied physics*, 38(4S):2549, 1999.
- [153] Adam D Wright, Carla Verdi, Rebecca L Milot, Giles E Eperon, Miguel A Pérez-Osorio, Henry J Snaith, Feliciano Giustino, Michael B Johnston, and Laura M Herz. Electron–phonon coupling in hybrid lead halide perovskites. *Nature communications*, 7, 2016.
- [154] Melike Karakus, Søren A Jensen, Francesco D’Angelo, Dmitry Turchinovich, Mischa Bonn, and Enrique Canovas. Phonon–electron scattering limits free charge mobility in methylammonium lead iodide perovskites. *The journal of physical chemistry letters*, 6(24):4991–4996, 2015.
- [155] Ye Yang, David P Ostrowski, Ryan M France, Kai Zhu, Jao Van De Lagemaat, Joseph M Luther, and Matthew C Beard. Observation of a hot-phonon bottleneck in lead-iodide perovskites. *Nature Photonics*, 10(1):53, 2016.
- [156] MA Brand, A Malinowski, OZ Karimov, PA Marsden, RT Harley, AJ Shields, D Sanvitto, DA Ritchie, and MY Simmons. Precession and motional slowing of spin evolution in a high mobility two-dimensional electron gas. *Physical review letters*, 89(23):236601, 2002.
- [157] K. C. Hall, S. W. Leonard, H. M. van Driel, A. R. Kost, E. Selvig, and D. H. Chow. Subpicosecond spin relaxation in GaAs multiple quantum wells. *Applied Physics Letters*, 75(26):4156–4158, 1999.

- [158] K. C. Hall, K. Gündoğdu, E. Altunkaya, W. H. Lau, Michael E. Flatté, Thomas F. Boggess, J. J. Zinck, W. B. Barvosa-Carter, and S. L. Skeith. Spin relaxation in (110) and (001) InAs/GaSb superlattices. *Phys. Rev. B*, 68:115311, Sep 2003.
- [159] K. C. Hall, Wayne H. Lau, K. Gndodu, Michael E. Flatt, and Thomas F. Boggess. Nonmagnetic semiconductor spin transistor. *Applied Physics Letters*, 83(14):2937–2939, 2003.

Appendix Copyright Permissions

Figure 1.1

8/14/2017

RightsLink Printable License

JOHN WILEY AND SONS LICENSE TERMS AND CONDITIONS

Aug 14, 2017

This Agreement between Kimberley C Hall ("You") and John Wiley and Sons ("John Wiley and Sons") consists of your license details and the terms and conditions provided by John Wiley and Sons and Copyright Clearance Center.

License Number	416770000918
License date	Aug 14, 2017
Licensed Content Publisher	John Wiley and Sons
Licensed Content Publication	Angewandte Chemie International Edition
Licensed Content Title	New Light on an Old Story: Perovskites Go Solar
Licensed Content Author	Bettina V. Lotsch
Licensed Content Date	Dec 18, 2013
Licensed Content Pages	3
Type of use	Dissertation/Thesis
Requestor type	University/Academic
Format	Print and electronic
Portion	Figure/table
Number of figures/tables	1
Original Wiley figure/table number(s)	Figure 1
Will you be translating?	No
Title of your thesis / dissertation	PUMP PROBE STUDIES OF SPIN DYNAMICS IN THE 2D PEROVSKITE BUTYLAMMONIUM METHYLAMMONIUM LEAD IODIDE
Expected completion date	Sep 2017
Expected size (number of pages)	100
Requestor Location	Kimberley C Hall 1459, Oxford Street Dalhousie University Halifax, NS B3H4R2 Canada Attn: Kimberley C Hall
Publisher Tax ID	EU826007151

<https://s100.copyright.com/CustomerAdmin/PLF.jsp?ref=1174d084-10b3-4e5b-a1e8-f43379a7288f>

1/6

Figures 1.3

Open access article published under ACS AuthorChoice License.

Letter

Charge-Carrier Dynamics in 2D Hybrid Metal–Halide Perovskites

Rebecca L. Milot[†], Rebecca J. Sutton[†], Giles E. Eperon[†], Amir Abbas Haghighirad[†], Josue Martinez Hardigree[†], Laura Miranda[‡], Henry J. Snaith[†], Michael B. Johnston[†], and Laura M. Herz[†]

[†] Department of Physics, University of Oxford, Clarendon Laboratory, Parks Road, Oxford, OX1 3PU, United Kingdom

[‡] Oxford Photovoltaics Ltd., Unit 6, Begbroke Science Park, Woodstock Road, Oxford, OX5 1PF, United Kingdom

Nano Lett., 2016, 16 (11), pp 7001–7007

DOI: 10.1021/acs.nanolett.6b03114

Publication Date (Web): September 30, 2016

Copyright © 2016 American Chemical Society

*E-mail: laura.herz@physics.ox.ac.uk.

 ACS AuthorChoice - This is an open access article published under a Creative Commons Attribution (CC-BY) License, which permits unrestricted use, distribution and reproduction in any medium, provided the author and source are cited.

Figure 1.4

8/14/2017

RightsLink Printable License

**THE AMERICAN ASSOCIATION FOR THE ADVANCEMENT OF SCIENCE LICENSE
TERMS AND CONDITIONS**

Aug 14, 2017

This Agreement between Kimberley C Hall ("You") and The American Association for the Advancement of Science ("The American Association for the Advancement of Science") consists of your license details and the terms and conditions provided by The American Association for the Advancement of Science and Copyright Clearance Center.

License Number	4167680126867
License date	Aug 14, 2017
Licensed Content Publisher	The American Association for the Advancement of Science
Licensed Content Publication	Science
Licensed Content Title	Efficient Hybrid Solar Cells Based on Meso-Superstructured Organometal Halide Perovskites
Licensed Content Author	Michael M. Lee,Joël Teuscher,Tsutomu Miyasaka,Takurou N. Murakami,Henry J. Snaith
Licensed Content Date	Nov 2, 2012
Licensed Content Volume	338
Licensed Content Issue	6107
Volume number	338
Issue number	6107
Type of Use	Thesis / Dissertation
Requestor type	Scientist/individual at a research institution
Format	Print and electronic
Portion	Figure
Number of figures/tables	1
Order reference number	
Title of your thesis / dissertation	PUMP PROBE STUDIES OF SPIN DYNAMICS IN THE 2D PEROVSKITE BUTYLAMMONIUM METHYLAMMONIUM LEAD IODIDE
Expected completion date	Sep 2017
Estimated size(pages)	100
Requestor Location	Kimberley C Hall 1459, Oxford Street Dalhousie University Halifax, NS B3H4R2

<https://s100.copyright.com/CustomAdmin/PLF.jsp?ref=966c72ed-a052-4583-9c41-116da23b0ad6>

1/7

Figures 1.5 and 3.3

Open access article published under ACS AuthorChoice License.

Article**Ruddlesden–Popper Hybrid Lead Iodide Perovskite 2D Homologous Semiconductors**

Constantinos C. Stoumpos^{†¶}, Duyen H. Cao^{†¶}, Daniel J. Clark[‡], Joshua Young^{§⊥}, James M. Rondinelli[⊥], Joon I. Jang[‡], Joseph T. Hupp[†], and Mercouri G. Kanatzidis[†]

[†] Department of Chemistry, Northwestern University, 2145 Sheridan Road, Evanston, Illinois 60208, United States

[‡] Department of Physics, Applied Physics and Astronomy, Binghamton University, P.O. Box 6000, Binghamton, New York 13902, United States

[§] Department of Materials Science and Engineering, Drexel University, 3141 Chestnut Street, Philadelphia, Pennsylvania 19102, United States

[⊥] Department of Materials Science and Engineering, Northwestern University, 2220 Campus Drive, Evanston, Illinois 60208, United States

Chem. Mater., 2016, 28 (8), pp 2852–2867

DOI: 10.1021/acs.chemmater.6b00847

Publication Date (Web): April 15, 2016

Copyright © 2016 American Chemical Society

*E-mail: m-kanatzidis@northwestern.edu.

 ACS AuthorChoice - This is an open access article published under an ACS AuthorChoice License, which permits copying and redistribution of the article or any adaptations for non-commercial purposes.

Figure 2.2

8/14/2017

RightsLink Printable License

**AMERICAN PHYSICAL SOCIETY LICENSE
TERMS AND CONDITIONS**

Aug 14, 2017

This Agreement between Kimberley C Hall ("You") and American Physical Society ("American Physical Society") consists of your license details and the terms and conditions provided by American Physical Society and Copyright Clearance Center.

License Number	4167690898160
License date	Aug 14, 2017
Licensed Content Publisher	American Physical Society
Licensed Content Publication	Physical Review B
Licensed Content Title	Electronic model for self-assembled hybrid organic/perovskite semiconductors: Reverse band edge electronic states ordering and spin-orbit coupling
Licensed Content Author	J. Even et al.
Licensed Content Date	Nov 5, 2012
Licensed Content Volume	86
Type of Use	Thesis/Dissertation
Requestor type	Student
Format	Print, Electronic
Portion	chart/graph/table/figure
Number of charts/graphs/tables/figures	1
Portion description	Figure 3
Rights for	Main product
Duration of use	Life of Current Edition
Creation of copies for the disabled	no
With minor editing privileges	no
For distribution to	Worldwide
In the following language(s)	Original language of publication
With incidental promotional use	no
The lifetime unit quantity of new product	0 to 499

<https://s100.copyright.com/CustomerAdmin/PLF.jsp?ref=0e4404f1-b98a-4920-895a-d7220aad7f17>

1/3

Figure 2.3

8/14/2017

RightsLink Printable License

**NATURE PUBLISHING GROUP LICENSE
TERMS AND CONDITIONS**

Aug 14, 2017

This Agreement between Kimberley C Hall ("You") and Nature Publishing Group ("Nature Publishing Group") consists of your license details and the terms and conditions provided by Nature Publishing Group and Copyright Clearance Center.

License Number	4167681169017
License date	Aug 14, 2017
Licensed Content Publisher	Nature Publishing Group
Licensed Content Publication	Nature Physics
Licensed Content Title	Spin-polarized exciton quantum beating in hybrid organic-inorganic perovskites
Licensed Content Author	Patrick Odenthal, William Talmadge, Nathan Gundlach, Ruizhi Wang, Chuang Zhang, Dali Sun
Licensed Content Date	May 29, 2017
Type of Use	reuse in a dissertation / thesis
Requestor type	academic/educational
Format	print and electronic
Portion	figures/tables/illustrations
Number of figures/tables/illustrations	1
High-res required	no
Figures	Figure 1
Author of this NPG article	no
Your reference number	
Title of your thesis / dissertation	PUMP PROBE STUDIES OF SPIN DYNAMICS IN THE 2D PEROVSKITE BUTYLAMMONIUM METHYLAMMONIUM LEAD IODIDE
Expected completion date	Sep 2017
Estimated size (number of pages)	100
Requestor Location	Kimberley C Hall 1459, Oxford Street Dalhousie University Halifax, NS B3H4R2

Figure 2.4

8/14/2017 Rightslink® by Copyright Clearance Center









Title: Rashba and Dresselhaus Effects in Hybrid Organic-Inorganic Perovskites: From Basics to Devices

Author: Mikaël Kepenekian, Roberto Robles, Claudine Katan, et al

Publication: ACS Nano

Publisher: American Chemical Society

Date: Dec 1, 2015

Logged in as: Seth Todd 

Copyright © 2015, American Chemical Society

PERMISSION/LICENSE IS GRANTED FOR YOUR ORDER AT NO CHARGE

This type of permission/license, instead of the standard Terms & Conditions, is sent to you because no fee is being charged for your order. Please note the following:

- Permission is granted for your request in both print and electronic formats, and translations.
- If figures and/or tables were requested, they may be adapted or used in part.
- Please print this page for your records and send a copy of it to your publisher/graduate school.
- Appropriate credit for the requested material should be given as follows: "Reprinted (adapted) with permission from (COMPLETE REFERENCE CITATION). Copyright (YEAR) American Chemical Society." Insert appropriate information in place of the capitalized words.
- One-time permission is granted only for the use specified in your request. No additional uses are granted (such as derivative works or other editions). For any other uses, please submit a new request.

If credit is given to another source for the material you requested, permission must be obtained from that source.

[BACK](#)

[CLOSE WINDOW](#)

Copyright © 2017 [Copyright Clearance Center, Inc.](#) All Rights Reserved. [Privacy statement.](#) [Terms and Conditions.](#) Comments? We would like to hear from you. E-mail us at customer@copyright.com

Figure 3.4

8/14/2017 Rightslink® by Copyright Clearance Center









Title: 2D Homologous Perovskites as Light-Absorbing Materials for Solar Cell Applications

Author: Duyen H. Cao, Constantinos C. Stoumpos, Omar K. Farha, et al

Publication: Journal of the American Chemical Society

Publisher: American Chemical Society

Date: Jun 1, 2015

Logged in as: Seth Todd



Copyright © 2015, American Chemical Society

PERMISSION/LICENSE IS GRANTED FOR YOUR ORDER AT NO CHARGE

This type of permission/license, instead of the standard Terms & Conditions, is sent to you because no fee is being charged for your order. Please note the following:

- Permission is granted for your request in both print and electronic formats, and translations.
- If figures and/or tables were requested, they may be adapted or used in part.
- Please print this page for your records and send a copy of it to your publisher/graduate school.
- Appropriate credit for the requested material should be given as follows: "Reprinted (adapted) with permission from (COMPLETE REFERENCE CITATION). Copyright (YEAR) American Chemical Society." Insert appropriate information in place of the capitalized words.
- One-time permission is granted only for the use specified in your request. No additional uses are granted (such as derivative works or other editions). For any other uses, please submit a new request.

If credit is given to another source for the material you requested, permission must be obtained from that source.

[BACK](#)

[CLOSE WINDOW](#)

Copyright © 2017 [Copyright Clearance Center, Inc.](#) All Rights Reserved. [Privacy statement.](#) [Terms and Conditions.](#)
 Comments? We would like to hear from you. E-mail us at customer@copyright.com